Revista Brasileira de Ciências Mecânicas

Journal of the Brazilian Society of Mechanical Sciences

3

PUBLICAÇÃO DA ABCM - ASSOCIAÇÃO BRASILEIRA DE CIÊNCIAS MECÂNICAS

VOL. XVII - Nº 3 - 1995 ISSN 0100-7386

REVISTA BRASILEIRA DE CIÊNCIAS MECÂNICAS

JOURNAL OF THE BRAZILIAN SOCIETY OF MECHANICAL SCIENCES

REVISTA BRASILEIRA DE CIÊNCIAS MECÂNICAS
JOURNAL OF THE BRAZILIAN SOCIETY OF MECHANICAL SCIENCES
Vol. 1, Nº 1 (1979) -
Rio de Janeiro: Associação Brasileira de Ciências Mecânicas
Trimestral
Inclui referências bibliográficas.
1. Mecânica
ISSN-0100-7386

A REVISTA BRASILEIRA DE CIÊNCIAS MECÂNICAS publica trabalhos que cobrem os vários aspectos da ciência e da tecnologia em Engenharia Mecânica, incluindo interfaces com as Engenharias Civil, Elétrica, Química, Naval, Nuclear, Aeroespacial, Alimentos, Agrícola, Petróleo, Materiais, etc., bem como aplicações da Física e da Matemática à Mecânica.

Publicação da /Published by
ASSOCIAÇÃO BRASILEIRA DE CIÊNCIAS MECÂNICAS
THE BRAZILIAN SOCIETY OF MECHANICAL SCIENCES

Secretária da ABCM: Ana Lucia Frões de Souza
Av. Rio Branco, 124 - 18º andar - Tel./Fax (021) 222-7128
20040-001 - Rio de Janeiro RJ - Brasil

Presidente: **Arthur Palmeira Ripper**
Vice-Presidente: **Sidney Stuckenbruk**
Secret. Geral: **Agamenon R. E. Oliveira**
Secretário: **Carlos Alberto de Almeida**
Diretora de Patrimônio: **Aura Conci**

REVISTA FINANCIADA COM RECURSOS DO

Programa de Apoio a Publicações Científicas

MCT CNPq FINEP

FAPESP - Fundação de Amparo a Pesquisa do Estado de São Paulo

RBCM - J. of the Braz. Soc. Mechanical Sciences
Vol. XVII - nº3 - 1995 - pp. 252-268

ISSN 0100-7386
Printed in Brazil

Initial Values Searching Method For Solving Non-Similar Boundary Layer Problems by the Local Non-Similarity Model

José Viriato Coelho Vargas
Departamento de Engenharia Mecânica
IME - Instituto Militar de Engenharia
22290-270 - Rio de Janeiro, RJ - Brasil

Francisco Eduardo Mourão Saboya
Departamento de Engenharia Mecânica
UFF - Universidade Federal Fluminense
Niterói, RJ - Brasil

Marcus V. A. Bianchi
Heat Transfer Laboratory
School of Mechanical Engineering
Purdue University
West Lafayette, IN 47907-1288 - USA

Abstract

The present work introduces a method for searching initial values, to solve non-similar Boundary Layer problems through the local non-similarity model. In order to provide a view to illustrate the method, the problem of mixed convection on a wedge and the surface mass transfer problem of uniform injection (blowing) in a flat plate under forced convection are solved herein. The results for the latter and for the special case when the wedge becomes a vertical plate are compared with prior information from the published literature and novel results are presented for the 90° and 180° wedge, where the problem is non-similar and $U = Ax^m$. It is also shown the method provides results of high accuracy, for the whole range of variation of the non-similarity parameter, and with only one transformation of variables, based on scale analysis for forced convection, both to uniform surface temperature and to uniform heat flux.

Keywords: Boundary Layer Problem, Local Non-Similarity, Initial Value Search, Mixed Convection on a Wedge, Uniform Injection

Introduction

Some boundary layer problems are similar, i.e., they can be treated as one or a set of ordinary differential equations, but many of them are not, they are the so called non-similar problems. They are modeled by a system of parabolic equations that need to be solved by a different approach. Among the available methods for the solution of these problems, the local non-similarity method introduced by Sparrow et al. (1970) has some important features that should be considered, depending on the objectives of the researcher. The solutions are found locally, i.e., independently of information from other streamwise positions. The problem reduces locally to a set of ordinary differential equations, so the approach becomes simple and direct, both in concept and in application and demands low computational time if compared to other methods, still preserving the accuracy of the results.

A survey on the local non-similarity method was presented by Chen (1988), bringing together the solutions of several non-similar boundary layer problems, with the transformed conservation equations either in the integral or differential form. The study reports the difficulty for convergence for high values of the non-similarity parameter, and also requiring excessive computational time due to the unknown initial values. To deal with this problem, it is suggested to use short increments of the non-similarity parameter, from the starting condition when the parameter is zero and the problem becomes similar with easy convergence, proceeding from this point step by step until the solution at the desired value of the non-similarity parameter is achieved. Indeed, this technique leads to the solution, on the other hand it eliminates one of the most attractive features of the local non-similarity model, which is the possibility of obtaining local and autonomous solutions, besides the extra computational time required.

In the present paper, a method to provide automatically the proper initial values for achieving convergence of the local non-similarity model at any streamwise position is introduced andillustrated.

Manuscript received: March 1995. Technical Editor: Carlos Alberto Carrasco Altemani

The method turns possible to preserve the most attractive aspects of the local non-similarity method, i.e., local solutions independently of other streamwise informations and low computational time.

Several authors have dealt with the problem of mixed convection on a vertical wall (Chen, 1988; Cebeci and Bradshaw, 1988) and with the problem of mixed convection on inclined surfaces (Mucoglu and Chen, 1979; Wickern, 1991) considering U = constant in all geometries. This paper presents results to be compared with previous information for the vertical wall and novel results for the 90° and 180° wedge angles, in the sense that the free stream velocity is considered $U = Ax^m$, according to the potential flow theory. This assumption implies that the pressure gradient in the momentum equation is not zero. No pressure gradients were considered in a previous problem (Mucoglu and Chen, 1979). In two recent studies (Wickern, 1991), in contrast to Prandtl's classical boundary layer theory, the pressure in the boundary layer was no longer determined by the pressure outside, but still with the assumption of U = constant. As a result of these remarks, non-similar wedge flow solutions under mixed convection with $U = Ax^m$ have not been given yet, except for the specific case of a vertical wall (m = 0).

The application of the IVSM is illustrated by the solution of the problem of mixed convection on a wedge, performing an analysis to study the effects of the buoyancy force on the heat transfer and friction characteristics of laminar forced convection flow which is either maintained at uniform temperature or subjected to uniform heat flux. In these problems, the IVSM allowed the solution to be obtained in the entire range of variation of the non-similarity parameter (0-100) with only one set of transformed equations based on scale analysis for forced convection. It has been reported in previous works, that either with the local non-similarity method (Chen, 1988) or with a finite-differences scheme (Cebeci and Bradshaw, 1988), the non-similar problem of mixed convection on a vertical wall with that set of transformed equations is increasingly difficult to converge as the non-similarity parameter increases. With the local non-similarity method, results were presented only up to $\xi = 10$ (Chen, 1988) and with finite-differences, when ξ is large, a new set of transformed equations obtained from similarity variables based on scale analysis for purely natural convection was used (Cebeci and Bradshaw, 1988). Also, solutions were presented, with a Keller's box scheme (Wickern, 1991) and with the local non-similarity method and finite-differences (Mucoglu and Chen, 1979), for several inclined plates, considering U = constant which is different from the cases treated in this paper, but again not for high values of the non-similarity parameter, therefore neither covering the entire range purely forced - mixed - free convection nor the more general case when $U = Ax^m$.

The solution of the surface mass transfer problem of uniform injection (blowing) in a flat plate under forced convection is also obtained. The results are compared with available published information.

Description

Since the method of local non-similarity is applied to the problems, the partial differential parabolic equations that model the non-similar boundary layer transform into a set of ordinary differential equations to be solved at any specific streamwise location (Chen, 1988). Some of the initial values required to carry on the solution are known, and the problem is completed with freestream conditions, therefore it is a boundary value problem.

Although results will be given only for m = 0, 1/3, 1/2 and 1, the model is valid for any wedge angle, except for the horizontal plate.

For solving the set of ordinary differential equations the Runge-Kutta method of 4^{th} order is applied, estimating the unknown initial values to start the calculations with the IVSM herein presented, associating the Newton shooting method to correct the estimated initial values (Kincaid and Cheney, 1991). The convergence is reached when the edge conditions are verified and also their first derivatives, since an asymptotic solution is required at this point, as described by Nachtsheim and Swigert (1965). Nevertheless, the Newton method requires the estimated vector of unknown initial conditions to be close enough to the actual vector, otherwise the integration diverges before reaching the edge of the boundary layer. As a result of this, the challenge is the estimate of initial values at any streamwise position, except for a low value of the non-similarity parameter, to guarantee that problem does not happen.

The initial values searching method consists in the estimate of a n-dimensional region instead of a n-dimensional vector of unknown initial conditions, where n is the number of unknown initialvalues,

thereafter by a searching approach the proper n-dimensional vector that leads to convergence is found. In the presentation that follows, the succeeding sections of the paper deal with the solution of non-similar boundary layers as a result of the mixed convection on a wedge, with uniform temperature and uniform heat flux and the problem of surface mass transfer. The first section, that contains the exposition of the method is more detailed than the subsequent sections.

Mixed Convection on a Wedge

A schematic presentation of the problem can be seen in Fig. 1. The three configurations are ways of achieving a potential profile for the freestream velocity, as reported by the potential flow theory, $U = Ax^m$, A is a constant.

The streamwise coordinate is represented by x and the transverse coordinate is y.

Nomenclature

C_{fx} = local friction factor, Eq. (31)

f = non-dimensional streamfunction related to the velocities of the problem

F_i = range of variation of dimension i, i = 1,...,4

g = derivative of f in respect to the non-similarity variable, $\frac{\partial f}{\partial \xi}$

g_x = magnitude of the gravity force component in the x direction

Gr_x = local Grashof number as a function of temperature, $\frac{g_x \beta \left(T_w - T_\infty\right) x^3}{\nu^2}$

Gr^*_x = local Grashof number as a function of the heat flux, $\frac{g_x \beta q_w x^4}{k\nu^2}$

IVSM= initial values searching method

k = thermal conductivity of the fluid

K = maximum numeric real value arbitrated as the bound for $s_i(\eta)$ according to the computer used in the calculations

m = parameter related to the wedge angle, $\frac{\beta_1}{2\pi - \beta_1}$

M = number of divisions of F2

n = parameter related to the surface temperature profile

N = number of divisions of F1

NF = number of functions calculated each step in the Runge-Kutta scheme

Nu_x = local Nusselt number, Eq. (30)

Pr = Prandtl number, $\frac{\nu}{\alpha}$

q_w = heat flux through the surface

$\vec{r}$ = actual vector of initial values

Re_x = local Reynolds number, $\frac{Ux}{\nu}$

$s_i(\eta)$= functions calculated each step in the Runge-Kutta scheme

T = temperature inside the boundary layer

Tx = surface temperature

T_∞ = temperature outside the boundary layer

u = velocity in the x direction, $\frac{\partial \Upsilon}{\partial y}$

U = velocity outside the boundary layer

UHF = uniform heat flux case

UWT= uniform wall temperature case

v = velocity in the y direction, $-\frac{\partial \Upsilon}{\partial x}$

v_w = velocity of injection

x = direction paralell to the surface

y = direction orthogonal to the surface

$\vec{Z}o$ = estimated vector of initial values

$\vec{Z}o_{ij}$ = region of estimated initial values to be searched

α = thermal diffusivity

β = volumetric coefficient of thermal expansion

β_1 = wedge angle

Υ = non-dimensional function related to the temperature for the UHF case

Γ = derivative of Υ in respect to the non-similarity variable, $\frac{\partial \Upsilon}{\partial x}$

$\Delta\xi$ = ξ increment

$\Delta\eta$ = η increment

ΔZ_1 = increment in dimension 1

ΔZ_2 = increment in dimension 2

ε = tolerance for convergence

ζ = surface mass transfer non-similarity variable

η = pseudo-similarity variable

η_∞ = value atributed to the similar variable at the edge of the boundary layer

θ = non-dimensional temperature, $\frac{T - T\infty}{Tw - T\infty}$

ν = kinematic viscosity

ξ = UWT non-similarity variable

ρ = density

τ_w = shear stress at the surface

Υ = stream function

ϕ = derivative of θ in respect to the non-similarity variable, $\frac{\partial \theta}{\partial \xi}$

X = UHF non-similarity variable

( )' = derivatives with respect to η

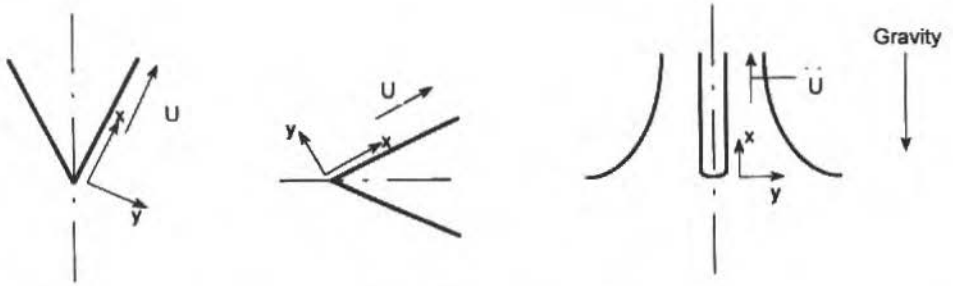

Fig. 1 Physical model and problem coordinates

Under the assumptions of laminar, constant-property, mixed convection flow, negligible viscous dissipation and Boussinesq approximation, the governing equations for the problem are:

$$\frac{\partial u}{\partial x} + \frac{\partial v}{\partial y} = 0 \tag{1}$$

$$u\frac{\partial u}{\partial x} + v\frac{\partial u}{\partial y} = U\frac{dU}{dx} \pm g_x\beta\,(T - T\infty) + \nu\frac{\partial^2 u}{\partial y^2} \tag{2}$$

$$u\frac{\partial T}{\partial x} + v\frac{\partial T}{\partial y} = \alpha\frac{\partial^2 T}{\partial y^2} \tag{3}$$

with two different sets of boundary conditions, one for the uniform wall temperature problem and the other for the uniform heat flux problem, as follows:

- uniform wall temperature

$$y = 0 : u = v = 0, T = T_w \; ; \; y \to \infty : u \to U, T \to T\infty \tag{4}$$

- uniform heat flux

$$y = 0 : u = v = 0, q_w = -k\left.\frac{\partial T}{\partial y}\right|_{y=0} \; ; \; y \to \infty : u \to U, T \to T\infty \tag{5}$$

The ± sign in Eq. (2) refers to the aiding flow (+) or to the opposing flow (-) representing the two possible situations in mixed convection. For the gravity orientation of Fig. 1, a positive component of the buoyancy force in the direction of the freestream velocity means an aiding flow, and when negative, an apposing flow.

Uniform wall temperature

In the model, the surface temperature is restricted to the form:

$$T_w - T_\infty = Bx^n \quad , \; B \to \text{constant} \tag{6}$$

So, when n = 0 the case of uniform surface temperature is represented.

A transformation of the problem from the (x, y) coordinate system to the (ξ, η) system is performed choosing η and ξ as (Schlichting, 1979; Sparrow et al., 1959; Sparrow and Yu, 1971; Bejan, 1984; Burmeister, 1983):

$$\eta = y\sqrt{\frac{U}{vx}} \; ; \xi = \frac{|Gr_x|}{Re_x^2} \tag{7}$$

The non-dimensional stream function is:

$$f(\xi, \eta) = \frac{\Upsilon(x, y)}{\sqrt{vxU}} \tag{8}$$

The resulting transformed governing equations are:

$$f''' + \frac{1+m}{2} ff'' + m \pm \xi\theta - m(f')^2 = \xi(1 + n - 2m)(f'g' - gf'') \tag{9}$$

$$\frac{\theta''}{Pr} + \frac{1+m}{2} f\theta' - nf'\theta = \xi(1 + n - 2m)(\phi f' - g\theta') \tag{10}$$

where $g = \partial f/\partial\xi$ and $\phi = \partial\theta/\partial\xi$, and with the following transformed boundary conditions:

$$\begin{aligned} &\eta = 0 \; : \; f' = 0 \; ; \; 0 = 1 \; ; \; (1+m) f + 2\xi g (1 + n - 2m) = 0 \\ &\eta \to \infty \; : \; f' \to 1 \; ; \; \theta \to 0 \end{aligned} \tag{11}$$

For the sake of conciseness the description of the initial values searching method is at first applied to the local similarity method (Sparrow et al., 1970), thereafter, as an extension, to the local non-similarity method.

The local similarity method assumes g and ϕ are small enough so that they may be neglected, hence Eqs. (9) to (11) become:

$$f''' + \frac{1+m}{2} ff'' + m \pm \xi\theta - m(f')^2 = 0 \tag{12}$$

$$\frac{\theta''}{Pr} + \frac{1+m}{2} f\theta' - nf'\theta = 0 \tag{13}$$

with the following boundary conditions:

$$\begin{aligned} &\eta = 0 \; : \; f' = 0 \; ; \; 0 = 1 \; ; \; 0 = 1 \\ &\eta \to \infty \; : \; f' = 1 \; ; \; 0 \to 0 \end{aligned} \tag{14}$$

The parameter ξ is regarded as a constant at any streamwise location, therefore the set of equations is treated as ordinary differential equations at each location.

With the increase of the value of ξ, the results become more uncertain, as reported by the literature (Sparrow et al., 1970; Chen, 1988; Sparrow and Yu, 1971), because of the assumptions that led to Eqs. (12) to (14) of the local similarity method.

The conditions for f" and θ' at $\eta = 0$ are not known, thus it is necessary to provide a good estimate to start the calculations aiming to achieve convergence. In other words, somehow a certain estimated vector has to be close enough to the actual vector of initial conditions.

Consider the following estimated vector of unknown initial conditions:

$$\vec{Z}_0 = (Z_{01}, Z_{02}) \tag{15}$$

Let the actual vector of initial conditions be:

$$\vec{r} = (r_1, r_2) \tag{16}$$

So, the vector $\vec{Z}_0$ should be in a region close enough to $\vec{r}$, in order to obtain convergence to the solution. Normally, depending on the equation that region is not wide. To deal with this difficulty, the IVSM estimates a discrete 2-dimensional region instead of a 2-dimensional vector $\vec{Z}_0$, as follows:

$$\vec{Z}_{0ij} = (Z_{0i1}, Z_{0j2}), \quad \begin{matrix} i = 1, \ldots, N \\ j = 1, \ldots, M \end{matrix} \tag{17}$$

where N and M are the number of divisions of the chosen range of variation of dimensions 1 and 2, respectively.

Equation (17) defines M x N vectors to be tested as possible initial values for the solution of Eqs. (12) to (14). Starting with $\vec{Z}_{011}$, each vector is tested until a proper vector is found to obtain convergence. Note that not all vectors need to be tested, therefore the search finishes when the proper vector is found.

Call F_1 and F_2, the arbitrary ranges of variation for dimension 1 and for dimension 2, respectively. The increments to changes the value of $\vec{Z}_{0ij}$ are:

$$\Delta Z_1 = \frac{F_1}{N} \; ; \; \Delta Z_2 = \frac{F_2}{M} \tag{18}$$

As a result of that, a new value of $\vec{Z}_{0ij}$ to be tested comes from:

$$\vec{Z}_{0(i+1)(j+1)} = (Z_{0i1} + \Delta Z_1, Z_{0j2} + \Delta Z_2) \tag{19}$$

For each $\vec{Z}_{0ij}$ it is verified whether the integration diverges or not. If so, a new value of $\vec{Z}_{0ij}$ is tested, until a proper one leading to a solution is found. At this point the search stops, even if the entire region has not been tested yet.

The test mentioned in last paragraph consists in verifying if the functions calculated during the integration of the equations remain bound along the whole domain. In other words:

$$|s_i(\eta)| < K, \quad i = 1, \ldots, NF \tag{20}$$

where $s_i(\eta)$ are the functions and NF is the number of functions that are calculated in each step of the Runge-Kutta scheme, and K is an arbitrarily big number chosen according to the computer being used in the calculations.

For each value of ξ, Eqs. (12) to (14) provide the local similarity solution, therefore the corresponding initial values $f''_{SL}(\xi, 0)$ and $\theta'_{SL}(\xi, 0)$ are now available, where the index SL refers to the local similarity solution.

Applying the local non-similarity method to the problem, Eqs. (9) to (11) are differentiated in respect to ξ, neglecting the terms containing the second derivatives with respect to ξ, eventually obtaining:

$$g'' + \frac{1+m}{2} f g'' - (1+n) f' g' + \left(\frac{3}{2} + n - \frac{3}{2} m\right) f' g \pm \xi \phi \pm \theta = \xi (1 + n - 2m)(g' g' - g g'') \tag{21}$$

$$\frac{1}{Pr}\phi'' + \frac{1+m}{2} f\phi' + (2m - 2n - 1) f'\phi + \left(\frac{3}{2} + n - \frac{3}{2}m\right) g\theta' - ng'\theta = \tag{22}$$

$$\xi (1 + n - 2m) (g'\phi - g\phi')$$

The boundary conditions become:

$$\eta = 0 : f = 0 \; ; g = 0 \; ; f' = 0 \; ; g' = 0 \; ; \theta = 1 \; ; \phi = 0 \tag{23}$$
$$\eta \to \infty : f' \to 1 \; ; g' \to 0 \; ; \theta \to 0 \; ; \phi \to 0$$

For each desired value of ξ, the set of ordinary differential equations (9), (10), (21) to (23) has to be solved. Since only one differentiation was performed and some selected terms neglected this is the so called second order non-similarity method. Although the approach for the IVSM is applied to these equations, it could be easily extended to higher order systems.

The set of equations requires the estimation of four unknown initial values, to wit:

$$f''(\xi, 0), \theta'(\xi, 0), g''(\xi, 0) \text{ and } \phi'(\xi, 0)$$

This time, a 4-dimension region has to be defined such that for a specified value of ξ the IVSM searches four ranges of variation, one for each dimension.

The ranges of variation for to $f''(\xi, 0)$ and $\theta'(\xi, 0)$ be searched are defined based on the values obtained in the local similarity solution, as follows:

$$\{F_1 \in \mathbb{R} | f''_{low}(\xi, 0) < f''_{SL}(\xi, 0) < f''_{high}(\xi, 0)\} \tag{24}$$

$$\{F_2 \in \mathbb{R} | \theta'_{low}(\xi, 0) < \theta'_{SL}(\xi, 0) < \theta'_{high}(\xi, 0)\} \tag{25}$$

where F_1 is the range for $f''(\xi, 0)$ and F_2 is the range for $\theta'(\xi, 0)$.

The center points come from the local similarity solution and since the local nonsimilarity solution is expected to be close enough, it is noted that the low and high values can be chosen close to the local similarity solution, say 10% for low values of ξ up to 30% for high values of ξ, for example. These values establish an upper and a lower limit for the interval. Anyway, if necessary, according to each problem, this interval can be increased or reduced as desired.

It is also desirable to have a proper estimate for the other two unknown initial values $g''(\xi, 0)$ and $\phi'(\xi, 0)$.

Therefore, from a first order backward differences approximation, in $\eta = 0$:

$$g''_{ini}(\xi, 0) = \frac{f''_{SL}(\xi, 0) - f''_{SL}(\xi - \Delta\xi, 0)}{\Delta\xi} \tag{26}$$

$$\phi'_{ini}(\xi, 0) = \frac{\theta'_{SL}(\xi, 0) - \theta'_{SL}(\xi - \Delta\xi, 0)}{\Delta\xi} \tag{27}$$

the values of $f''_{SL}(\xi - \Delta\xi, 0)$ and $\theta'_{SL}(\xi - \Delta\xi, 0)$ also come from the local similarity solution, which is easily convergent. The two other regions can now be chosen based on the central points defined by Eqs. (26) and (27), as follows:

$$\{F_3 \in \mathbb{R} | g''_{low}(\xi, 0) < g''_{ini}(\xi, 0) < g''_{high}(\xi, 0)\} \tag{28}$$

$$\{F_4 \in \mathbb{R} | \phi'_{low}(\xi, 0) < \phi'_{ini}(\xi, 0) < \phi'_{high}(\xi, 0)\} \tag{29}$$

It is important to note the low and high values can also be chosen close to the center values, because it is expected the central values are sufficiently close to the local similarity solution.

The local Nusselt number Nu_x and the local friction factor C_{fx} are defined by:

$$Nu_x = \frac{qw}{T_w - T_\infty} \cdot \frac{x}{k} = -\theta'(\xi, 0) Re_x^{1/2} \tag{30}$$

$$Cf_x = \frac{Tw}{(\rho U^2/2)} = 2f''(\xi, 0) Re_x^{-1/2} \tag{31}$$

Uniform heat flux

In this case the boundary conditions for the problem are represented by equations (5). This time, another transformation from the (x, y) system to the (χ, η) system is necessary.

Let η be defined as in Eq. (7) and:

$$\chi = \frac{|Gr_x^*|}{Re_x^{5/2}} \tag{32}$$

$$f(\chi, \eta) = \frac{\Upsilon(x, y)}{\sqrt{\nu x U}} \tag{33}$$

$$\Upsilon = \frac{(T - T\infty) Re_x^{1/2}}{q_w x/k}, \tag{34}$$

The resulting transformed equations are:

$$f''' + \frac{1+m}{2} ff'' + m \pm \chi\gamma - mf'^2 = \chi\left(\frac{3}{2} - \frac{5}{2}m\right)(f'g' - gf'') \tag{35}$$

$$\frac{1}{Pr}\gamma'' - \frac{1-m}{2} f'\gamma + \frac{m+1}{2} f\gamma' = \left(\frac{3}{2} - \frac{5}{2}m\right)\chi(f'\Gamma - g\gamma') \tag{36}$$

The subsidiary equations for the local nonsimilarity model of second order are:

$$g''' + \frac{1+m}{2} fg'' - \frac{1+m}{2} f''g \pm \chi\Gamma \pm \gamma - 2mf'g' = \chi\left(\frac{3}{2} - \frac{5}{2}m\right)(g'g' - gg'') \tag{37}$$

$$\frac{1}{Pr}\Gamma'' + \frac{1+m}{2} f\Gamma' + (2 - 2m) g\gamma' + (3m - 2) f'\Gamma - \frac{1-m}{2} g'\gamma = \chi\left(\frac{3}{2} - \frac{5}{2}m\right)(g'\Gamma - g\Gamma') \tag{38}$$

The boundary conditions become:

$$\eta = 0:\ g' = 0;\ f' = 0;\ g = 0;\ f = 0;\ \Gamma' = 0;\ \gamma' = -1$$
$$\eta \to \infty : g' \to 0;\ f' \to 1;\ \Gamma' \to 0;\ \gamma' \to 0 \tag{39}$$

The local Nusselt number Nu_x and the local friction factor C_{fx} are given by:

$$Nu_x Re_x^{-1/2} = \frac{1}{\gamma(\chi, 0)} \tag{40}$$

$$C_{fx} Re_x^{1/2} = 2f''(\chi, 0) \tag{41}$$

The IVSM is applied to this case exactly the same way as it was in the uniform wall temperature case, since the Boundary Value Problem has four unknown initial values.

Surface Mass Transfer

The objective of this sections is to analyze a flat plate aligned parallel to a uniform freestream flow. As it is well known, the case of uniform surface mass transfer is a non-similar problem.

With the conservation equations for constant property, forced convection boundary layer flow over a flat plate, the transformed equations for the application of the local non-similarity model are (Sparrow and Yu, 1971):

$$f''' + ff'' = \zeta(f'g' - f''g) \tag{42}$$

$$g''' + fg'' - f'g' + 2f''g = 0 \tag{43}$$

$$\frac{1}{Pr}\theta'' + f\theta' - 2nf'\theta = \zeta(f'\phi - \theta' g) \tag{44}$$

$$\frac{1}{Pr}\phi'' + f\phi' - (1 + 2n) f'\phi + 2g\theta' - 2ng'\theta = 0 \tag{45}$$

with the boundary conditions:

$$\eta = 0:\ f = -\frac{1}{2}\zeta;\ \theta = 1;\ g = -\frac{1}{2};\ f' = 0;\ \phi = 0;\ g' = 0$$
$$\eta \to \infty : f' \to 1;\ \theta \to 0;\ g' \to 0;\ \phi \to 0 \tag{46}$$

and with the modified variables:

$$\eta = y\sqrt{\frac{U}{2\nu x}};\ \zeta = \frac{v_w}{U}\sqrt{\frac{2Ux}{\nu}} \tag{47}$$

$$f(\zeta,\eta) = \frac{\Upsilon}{\sqrt{2\nu x U}} \tag{48}$$

The local Nusselt number is given by:

$$Nu_x Re_x^{-1/2} = \frac{-\theta'(\zeta,0)}{\sqrt{2}} \tag{49}$$

The IVSM is applied to this model in conjunction with the local non-similarity method the same way as the other models presented earlier for a boundary values problem with four unknown initial values.

Results and Discussion

In this section, numerical computations were carried out for a fluid having a Prandtl number 0.7. The method of local non-similarity of second level was applied in all cases, such that four guesses were required for each test of the IVSM, therefore a 4-dimension region had to be estimated for each case solved, in the application of the IVSM. A sparse discretization was required for each guess range. At most ten divisions were used in a range, within ±30 % the center guess, which comes from the local similarity solution, if necessary. Therefore, at most 10^4 vectors $\hat{Z}_0$ had to be tested in the most unfavorable situation. Also, if convergence happens to be difficult, the history of this sparse run will lead to a better region closer to a proper $\hat{Z}_0$, then a new sparse run in this closer region will certainly lead to convergence. These tests are not computationally expensive because in the case when the estimated vector is not appropriate for convergence, Eq. (20) is not satisfied in the very beginning of the Runge-Kutta integration, and the IVSM automatically tests a new vector and so on, until the appropriate vector that leads to convergence is found. As pointed out in section 3, the entire region does not need to be tested. Once the appropriate vector is found the computations stop. Additionally, most cases did not require the estimate from the local similarity solution, since the user is able to figure from the physical understanding of the problem, a rough estimate for the guesses to start with. Of course, this is possible only because the IVSM uses an estimated region of possible guesses, not only one single vector. Anyway, after $\xi = 10$, in order to achieve convergence to a solution, the use of the IVSM was mandatory, in all cases studied in this paper. Results were obtained for the problem of mixed convection on a wedge, either with uniform surface temperature or with uniform heat flux, and for the problem of surface mass transfer on a flat plate.

To illustrate the validity of the results that have been obtained, the solutions for the similar wedge ($m = 0.5; n = 0$), for the vertical plate ($m = 0; n = 0$), both under mixed convection were compared to the results of Sparrow et al. (1959) and Chen (1988), respectively, in the case of uniform temperature, as particular solutions of the model developed in this paper. Also, in the case of uniform heat flux, the solutions for the vertical plate ($m = 0$) were compared to previous results (Mucoglu and Chen, 1979), as a particular case of the model presented here. In the surface mass transfer problem, the results were compared to the results of Sparrow and Yu (1971).

The integration step was determined by trial and error, reducing its size until coincidental solutions are found obeying a convergence criterion, consisting on the verification of the integrated functions along the domain, the boundary conditions and their derivatives directly on the edge of the boundary layer, according to a tolerance $\varepsilon = 10^{-6}$. The value of this tolerance should be relaxed depending on the degree of non-similarity of the problem to be analyzed. Some authors have reported the need to relax this tolerance when using the local non-similarity model of third order, to achieve convergence (Chen, 1988).

During the computations it is also necessary to adjust the value of η_∞, which was done here by trial and error (Chen, 1988), until asymptotic values are found on the edge of the boundary layer. With the IVSM, the values of the transformed functions and their derivatives could be verified directly on the edge of the boundary layer, guaranteeing an asymptotic solution with no need to use an error least square technique as described by Nachtsheim and Swigert (1965). All results reported in this paper

were obtained with $\eta_\infty = 10, \Delta\eta = 0.02$ and according to a tolerance $\varepsilon = 10^{-6}$, so that the same results were obtained with finer meshes and larger η_∞ domains.

Figure 2 shows the local Nusselt numbers and Fig. 3 shows the local friction factor as functions of ξ for the UWT case for several values of m (aiding flow) and in the small graphs, the local Nusselt numbers and the local friction factor as functions of ξ for the UWT case for several values of m (opposing flow), until the occurrence of a separation. Analyzing the results, it is seen that the local friction factor is more sensitive to changes in the buoyancy parameter than the local Nusselt number. As m increases, the effect of the buoyancy force decreases, since g_X is maximum when m = 0. The asymptotes of forced convection ($\xi = 0$) are given by:

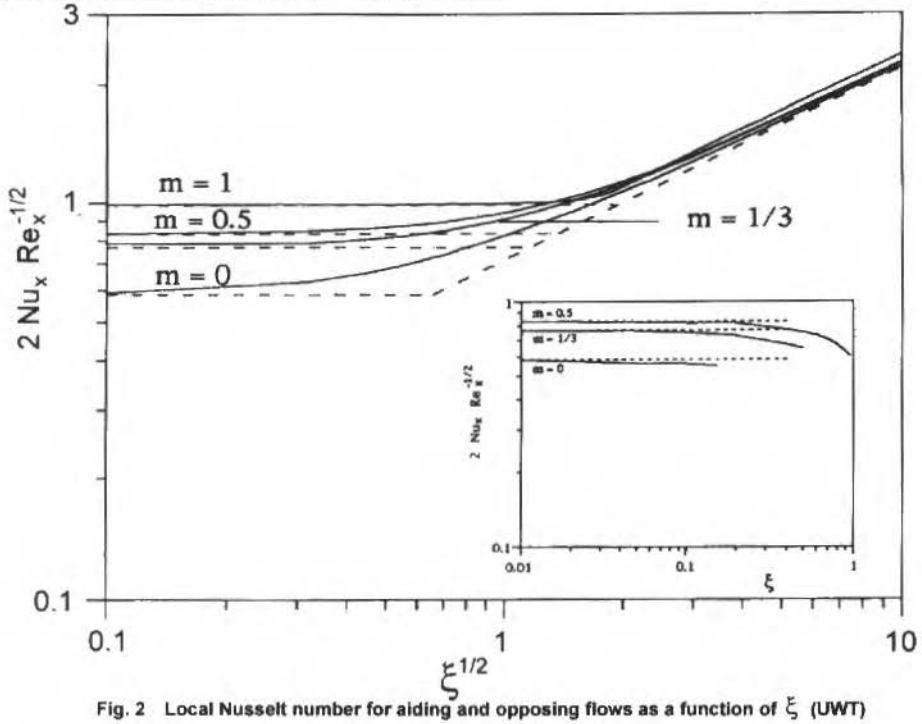

Fig. 2 Local Nusselt number for aiding and opposing flows as a function of ξ (UWT)

- m = 0 (vertical plate)

$$2C_{fx}Re_x^{1/2} = 1.32823;\ 2Nu_xRe_x^{-1/2} = 0.58536 \tag{50}$$

- $m = \frac{1}{3}$ (90° wedge)

$$2C_{fx}Re_x^{1/2} = 3.02967;\ 2Nu_xRe_x^{-1/2} = 0.76830 \tag{51}$$

- m = 0.5 (similar problem - 120° wedge)

$$2C_{fx}Re_x^{1/2} = 3.59887;\ 2Nu_xRe_x^{-1/2} = 0.83246 \tag{52}$$

- m = 1 (180° - frontal flow against a side wall - Fig. 1)

$$2C_{fx}Re_x^{1/2} = 4.93035;\ 2Nu_xRe_x^{-1/2} = 0.9919 \tag{53}$$

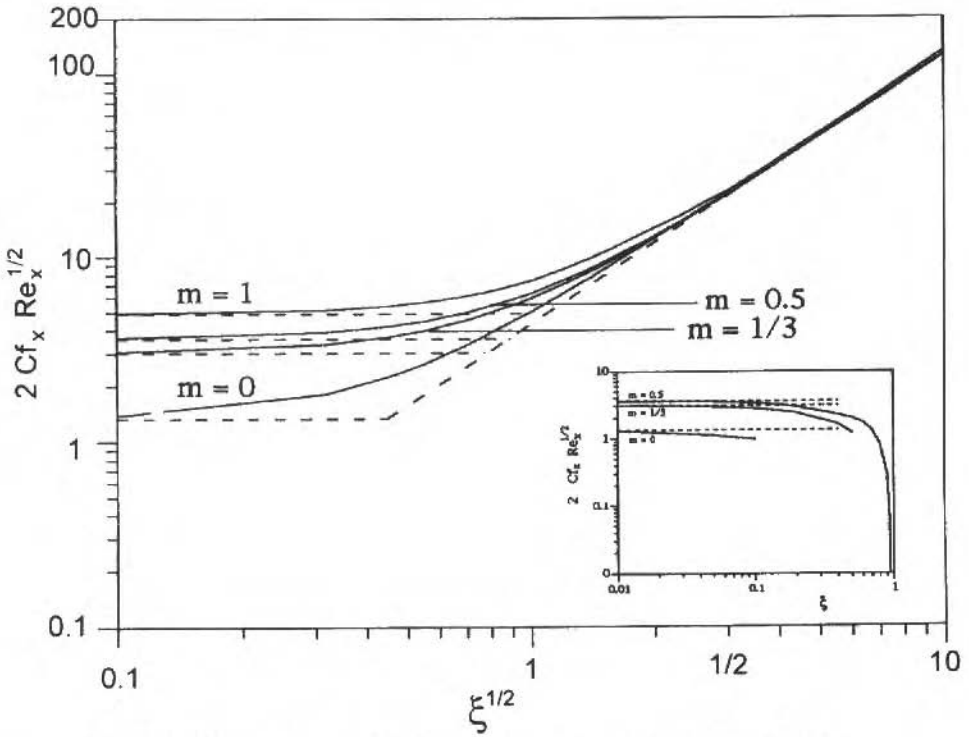

Fig. 3 Local friction factor for aiding and opposing flows as a function of ξ (UWT)

For high values of ξ the natural convection is predominant. For a fluid having a Prandtl number 0.7, the asymptotes are given by (Sparrow et al., 1959):

$$2C_{fx}Re_x^{1/2} = 3.84\left(\frac{Gr_x}{Re_x^2}\right)^{3/4} \; ; \; 2Nu_xRe_x^{-1/2} = 0.7065\left(\frac{Gr_x}{Re_x^2}\right)^{1/4} \tag{54}$$

Figures 4-5 show respectively some typical velocity and temperature profiles for several values of m and ξ for aiding flows. It is seen from these distributions that the velocity overshoot for some situations is very large. The largest one was found to be connected with a higher non-similarity parameter and m = 0.

The previous analysis allows the determination of a mixed convection regime defined with a 5% criterion where the local friction factor and the local Nusselt number deviate from either the pure forced or the pure free convection values, both for aiding and opposing flows, as seen in Table 1.

In the situation of opposing flow, the free convection generates a movement of particles against the potential flow, and a separation will occur when the generated flow is strong enough to overcome the potential flow. This is mathematically seen when the local friction factor achieves the values zero. As it is well known, the governing equations are not valid near a point of separation, therefore results are more difficult to obtain as the local friction factor approaches zero.

Figures 6-7 show the local Nusselt number and the local friction factor, respectively, as functions of the non-similarity parameter χ for the UHF case for m = 0 (vertical plate) and m = 1/3 (90° wedge), for aiding flow.

Table 1 Convection Criteria (UWT)

$2Nu_x Re_x^{-1/2}$	Aiding Flow		
	Ranges of Variation		
Value of m	Non-similarity Parameter $\rightarrow \xi = \lvert Gr_x \rvert / Re_x^2$		
	Forced Convection	Mixed Convection	Free Convection
0	0 - 0.056	0.056 - 6.230	6.230 - ∞
1/3	0 - 0.211	0.211 - 14.623	14.623 - ∞
0.5	0 - 0.326	0.326 - 17.439	17.439 - ∞

$2Cf_x Re_x^{1/2}$	Aiding Flow		
	Ranges of Variation		
Value of m	Non-similarity Parameter $\rightarrow \xi = \lvert Gr_x \rvert / Re_x^2$		
	Forced Convection	Mixed Convection	Free Convection
0	0 - 0.012	0.012 - 30.000	30.000 - ∞
1/3	0 - 0.036	0.036 - 15.705	15.705 - ∞
0.5	0 - 0.051	0.051 - 15.610	15.610 - ∞

$2Nu_x Re_x^{1/2}$	Opposing Flow	
	Ranges of Variation	
Value of m	Non-similarity Parameter $\rightarrow \xi = \lvert Gr_x \rvert / Re_x^2$	
	Forced Convection	Mixed Convection From
0	0 - 0.149	0.149
1/3	0 - 0.183	0.183
0.5	0 - 0.254	0.254

$2Cf_x Re_x^{1/2}$	Opposing Flow	
	Ranges of Variation	
Value of m	Non-similarity Parameter $\rightarrow \xi = \lvert Gr_x \rvert / Re_x^2$	
	Forced Convection	Mixed Convection From
0	0 - 0.015	0.015
1/3	0 - 0.046	0.046
0.5	0 - 0.060	0.060

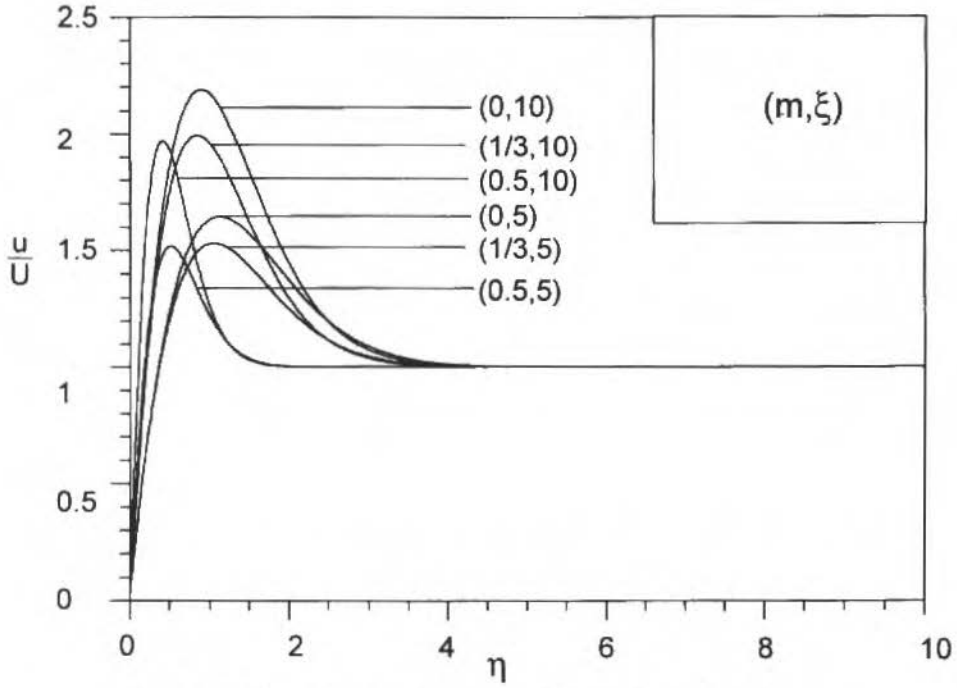

Fig. 4 Velocity profiles for several wedge angles and values of ξ (UWT)

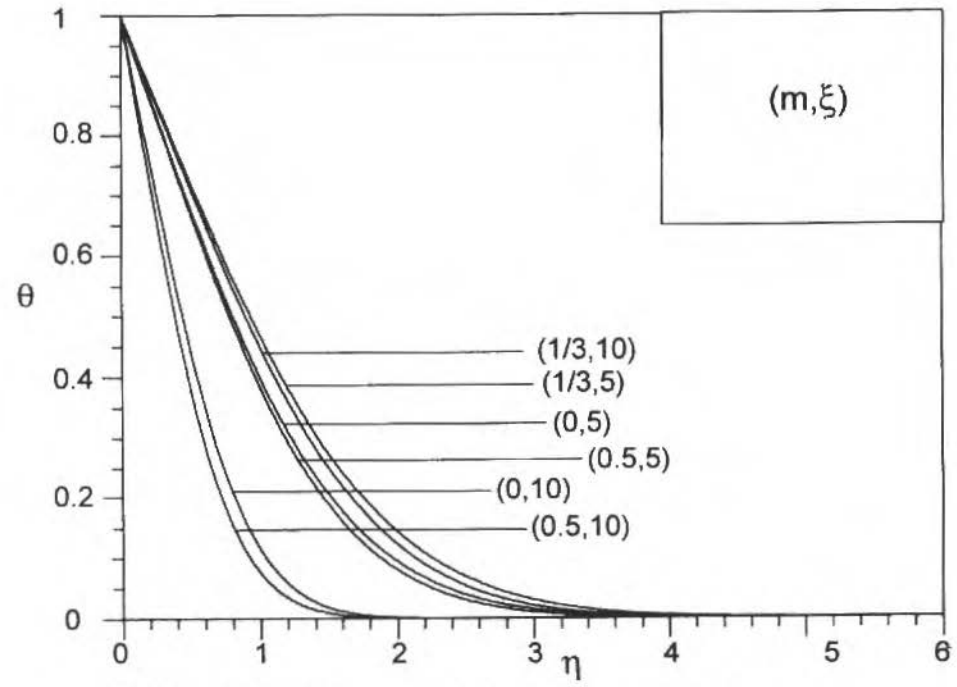

Fig. 5 Temperature profiles for several wedge angles and values of ξ (UWT)

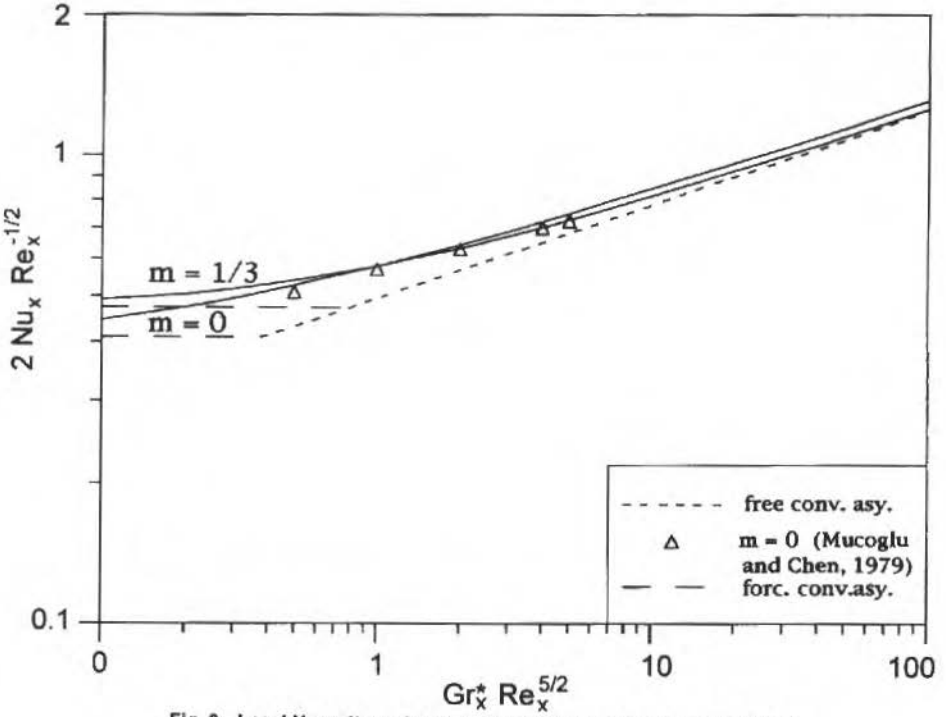

Fig. 6 Local Nusselt number for aiding flow as a function of χ (VHF)

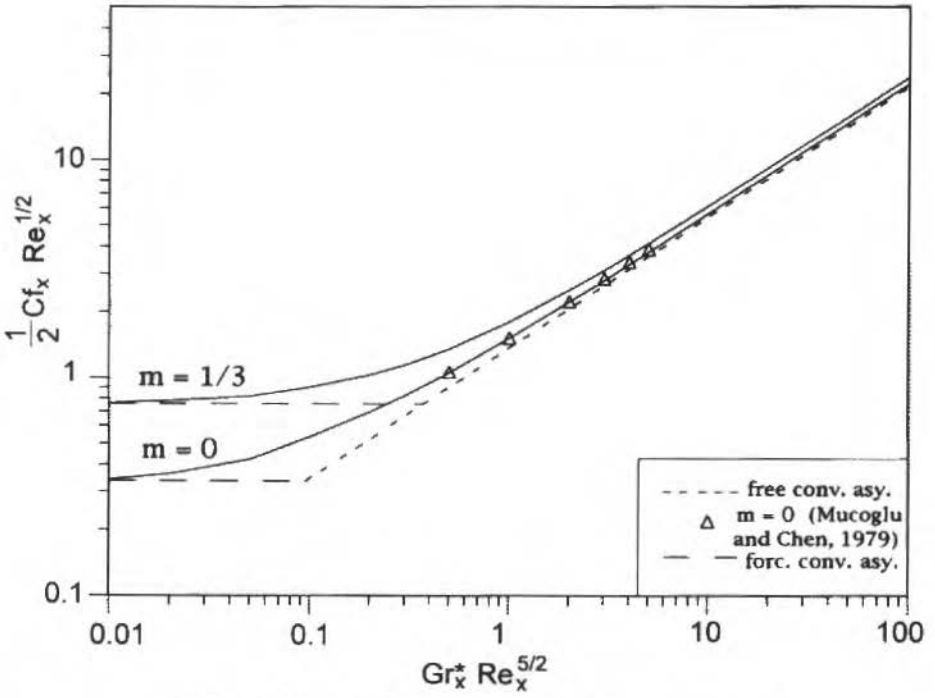

Fig. 7 Local friction factor for aiding flow as a function of χ (UHF)

The asymptotes of forced convection ($\chi = 0$) are given by:

- m = 0 (vertical plate)

$$2C_{fx}Re_x^{1/2} = 0.336;\ 2Nu_xRe_x^{-1/2} = 0.40884 \tag{55}$$

- $m = \frac{1}{3}$ (90° wedge)

$$2C_{fx}Re_x^{1/2} = 0.75744;\ 2Nu_xRe_x^{-1/2} = 0.47495 \tag{56}$$

For a fluid having a Prandtl number 0.7, the asymptotes for high values of χ are given from the solution of the similar problem of natural convection on a vertical wall (Bejan, 1984):

$$\frac{1}{2}C_{fx}Re_x^{1/2} = 1.421\left(\frac{Gr_x^*}{Re_x^{5/2}}\right)^{3/5};\ Nu_xRe_x^{-1/2} = 0.4873\left(\frac{Gr_x^*}{Re_x^{5/2}}\right)^{1/5} \tag{57}$$

In the analysis, the non-similarity parameter χ was varied from 0 to 100. The mixed convection regime for the UHF case is completely identified once solutions were obtained in the entire range purely forced - mixed - free convection, and for brevity, a table similar to Table 1 was not constructed for this case.

Again, it is seen the local friction factor is more sensitive to changes in the buoyancy parameter than is the local Nusselt number and also, as m increases the effect of the variation of χ decreases.

Figure 8 shows the local Nusselt numbers for the problem of surface mass transfer, covering the range of $\frac{v_w}{U}\sqrt{\frac{Ux}{\nu}} = \frac{\zeta}{\sqrt{2}}$ from 0 to 0.5.

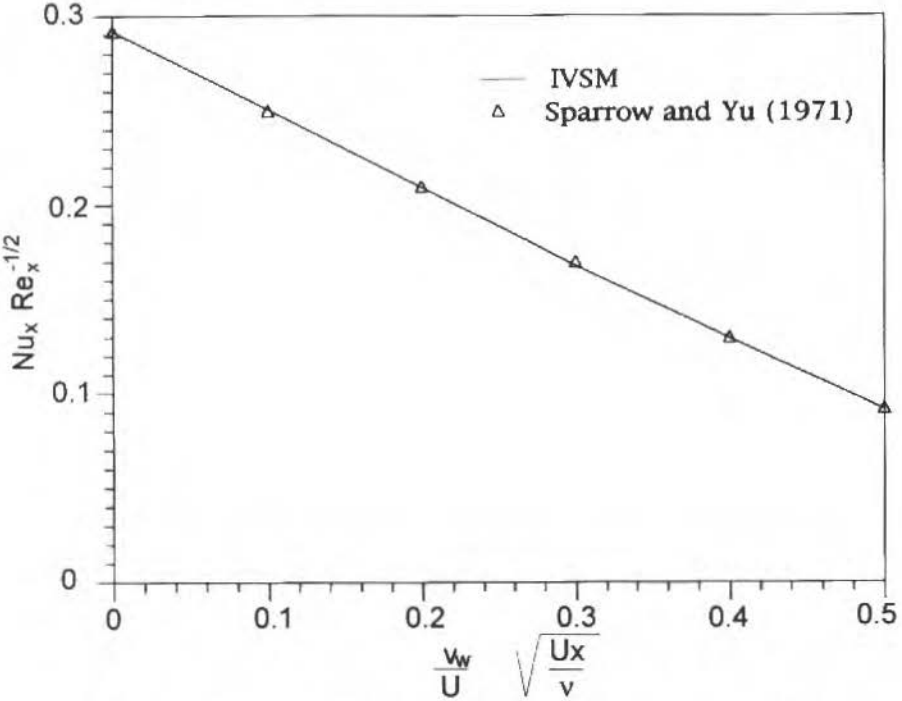

Fig. 8 Local Nusselt number as a function of $\zeta/\sqrt{2}$ (surface mass transfer)

As an illustration of the application of the IVSM, in the surface mass transfer problem it is seen that for an initial estimate for $f''(\zeta, 0) = 0.14$ the integration by the Runge-Kutta scheme diverges, even reducing the integration step, and for $f''(\zeta, 0) = 0.15$, it converges to a solution. The IVSM detects automatically the proper value to start the integration and achieve convergence. This observation was made using the correct values of $\theta'(\zeta, 0)$, $g''(\zeta, 0)$ and $\phi'(\zeta, 0)$, with $\Delta\eta = 0.03$, $\varepsilon = 10^{-6}$, $\zeta = \left(\frac{\sqrt{2}}{2}\frac{v_w}{U}\sqrt{\frac{Ux}{\nu}}\right) = 0.5$ and $Pr = 0.7$.

It is convenient to emphasize that a numerical scheme with step size control (Kincaid and Cheney, 1991) to integrate the transformed equations would certainly bring advantages to the application of the IVSM, but it would not be so successful if applied alone with the local non-similarity model, as it was shown in last paragraph.

Concluding Remarks

In this paper a method was presented to be applied in conjunction with the local non-similarity method to solve non-similar boundary layer problems. Several problems were solved and novel results presented for the problem of mixed convection on a wedge with $U = Ax^m$ for $m = 1/3$ and $m = 1$ covering the entire range of purely forced - mixed - free convection. The key conclusions of this study are:

a) The novel results in entire range purely forced-mixed-free convection allow the identification of a mixed convection regime in all cases studied, both for the local friction factor and the local Nusselt number;

b) The IVSM is a powerful tool to solve non-similar boundary layer problems, detecting the appropriate estimate for the set of unknown initial values guarantees the convergence to a solution in the entire range of the phenomenon, which was not done in previous studies (Chen, 1988; Mucoglu and Chen, 1979; Wickern, 1991), and

c)With the method of finite-differences (Cebeci and Bradshaw, 1988), two sets of transformed equations had to be used to obtain the solution for the vertical wall problem. On the other hand, the IVSM solved the same problem with only one set of equations, in a simpler and more efficient way, in the sense that less computational time is required by the local nonsimilarity method than the finite-differences scheme. Note that the finite-differences method requires a fine mesh both in the ξ and η directions, while the local non-similarity method requires a fine mesh only in the η direction.

References

Bejan, A., 1984, Convection Heat Transfer, 1st Edn, Chap. 2, Wiley, New York.

Burmeister, L. C., 1983, Convective Heat Transfer, lst Edn, p. 299, Wiley, New York.

Cebeci, T., and Bradshaw, P., 1988, Physical and Computational Aspects of Convective Heat Transfer, lst End, Chap. 9, Springer-Verlag, New York, Inc.

Chen, T. S., 1988, "Parabolic systems: local non-similarity method". In Handbook of Numerical Heat Transfer (Edited by W. J. Minkowycz, E. M Sparrow, G. E Schneider and R. H. Pletcher), Chap. 5, Wiley, New York.

Kincaid, D., and Cheney, W., 1991, Numerical Analysis, 1st Edn, Chap. 8, Wadsworth, Belmont, CA.

Mucoglu, A., and Chen. T. S.,1979, "Mixed Convection on Inclined Surfaces", ASME Journal of Heat Transfer, Vol. 101, pp. 422-426.

Nachtsheim, P. R., and Swigert, P.,1965, "Satisfaction of Asymptotic Boundary Conditions in Numerical Solution of Systems of Nonlinear Equations of Boundary Layer Type", NASA TN D-3004, Lewis Research Center.

Schlichting, H., 1979, Boundary Layer Theory, 7th Edn, Chap. 8, McGraw-Hill, New York.

Sparrow, E. M., Eichhorn, R., and Gregg, J. L. 1959, "Combined Forced and Free Convection in a Boundary Layer Flow", The Physics of Fluids, Vol. 3, pp. 319-328.

Sparrow, E. M., Quack, H., and Boerner, C. J.,1970, "Local Nonsimilarity Boundary Layer Solutions", AIAA Journal, Vol. 8, pp. 1936-1942.

Sparrow, E. M., and Yu, H.S., 1971, "Local Nonsimilariry Thermal Boundary Layer Solutions", ASME Journal of Heat Transfer, Vol. 93, pp. 328-334.

Wickern, G., 1991, "Mixed Convection from an Arbitrarily Inclined Semi-infinite Flat Plate- I. The Influence of Inclination Angle", International Journal of Heat and Mass Transfer, Vol. 34, pp. 1935-1945.

Wickern, G., 1991, "Mixed Convection from an Arbitrarily Inclined Semi-infinite Flat Plate-II. The Influence of the Prandtl Number", International Journal of Heat and Mass Transfer, Vol. 34, pp. 1947-1957.

RBCM - J. of the Braz. Soc. Mechanical Sciences
Vol. XVII - nº3 - 1995 - pp. 269-277

ISSN 0100-7386
Printed in Brazil

Strain Rate Effects on the Fracture Toughness Mechanisms of an Epoxy Resin and its Alumina Powder Composite

José Roberto Moraes d' Almeida
Materials Science and Metallurgy Department
Pontifícia Universidade Católica do Rio de Janeiro
Rua Marquês de São Vicente, 225 - Gávea
22453-900 - Rio de Janeiro - RJ - Brasil.

Sérgio Neves Monteiro
Science and Technology Center
Universidade Estadual do Norte Fluminense
Av. Alberto Lamego, 2000 - Horto
28015-620 - Campos - RJ - Brasil

Abstract

The micromechanisms of fracture of an alumina powder epoxy matrix composite was identified and compared with the fracture mechanisms of the neat epoxy matrix. The effect of strain rate upon the fracture behavior of the composite and that of the neat epoxy matrix was evaluated. A strong increase in the neat resin fracture toughness at high strain rates was associated with crack tip blunting.
Keywords: Composite, Crack Blunting, Strain Rate Effect.

Introduction

In the last 30 years thermoset polymers are being increasingly used as adhesives and also as matrix in composite materials (Chawla, 1987). Nevertheless, they are brittle materials and have very low critical values both for the stree intensity factor, K_{Ic}, and for the strain energy release rate, G_{Ic}. For epoxy resins these values range typically from 0.6 to 0.8 $MPa.m^{1/2}$ and from 0.1 to 0.2 KJm^{-2} for K_{Ic} and G_{Ic}, respectively (Bandyopadhyay, 1990). The fracture toughness can be increased by incorporating, to the polymer, different types of fillers, like fibers, elastomers, rigid particles (Low and May, 1988; Bandyopadhyay, Pearce and Mestan, 1985; Kinloch, Maxwell and Young, 1985) and even thermoplastic polymers (Bucknall and Gilbert, 1989). The actual acting toughness mechanisms are a function of the difference between the resin matrix and filler properties and/or the filler aspect ratio. The three main possible toughness mechanisms are due to: i) crack anchoring or deflection at the filler-matrix interface (Low and May, 1988; Lange and Radford, 1971), ii) crack bridging by fibers or stretched elastometric particles (Bandyopadhyay, Pearce and Mestan, 1985) or iii) localized crack tip plastic deformation (Kinloch, Maxwell and Young, 1985). The toughness of the composities is also a function of external variables, such as the imposed stress field or strain rate. Furthermore the incorporation of rigid particles brings to the polymer a frequently desirable increase in stiffness.

In this work the micromechanisms of fracture of an alumina particle reinforced epoxy matrix composite are studied as a function of the applied strain rate and compared with the unfilled epoxy matrix fracture mechanisms.

Experimental Procedures and Materials

The epoxy system studied is based on a difunctional liquid epoxy resin, diglycidyl ether of bisphenol A (DGEBA), crosslinked with an aliphatic amine, triethylenetetramine (TETA). Predried and sieved alumina particles (99.9% alumina) with mean diameter of 0.26 μ m were used as fillers. The proper quantities of resin and hardener were thoroughly mixed in an open container for at least 10 minutes. The alumina particles were, then, slowly added and the slurry formed wasagain mixed for more 5 to 10 minutes. The mixture was poured into bar shaped open silicone molds. The cure of the composite was achieved at room temperature and the resin/hardener/filler ratio used was 100/13/30, on a weight basis.

Manuscript received: June 1995. Technical Editor: Agenor de Toledo Fleury

The density of the composite was measured following the ASTM Standard D-792. The volume fractions of the filler, V_f, and voids, V_v, were obtained from the micromechanics equations (Schoutens, 1984)

$$V_f = \frac{1}{\rho_f - \rho_m}\left[\rho_c - \rho_m (1 - V_v)\right] \quad (1)$$

$$V_V = 1 - \rho_c\left(\frac{M_f}{\rho_f} + \frac{M_m}{\rho_m}\right) \quad (2)$$

where ρ is the density, M the mass fraction and the sub-indexes f, m, c and v stand for filler, matrix, composite and void, respectively. Tabulated values for the density of the resin and of the alumina particles were used in the calculations, namely (Shackelford, 1985): $\rho_m = 1160$ kg/m^3 and $\rho_f = 3970$ Kg/m^3.

Composite and neat resin specimens were tested in three-point bending (TPB) at slow, $v = 1.7 \times 10^{-5}$ m/s, and impact, $v = 3.46$ m/s, speeds. The imposed strain rates were 5×10^{-4} s^{-1} and 150 s^{-1}, respectively. The geometry and the average dimensions of the specimens used are shown in Fig. 1. Three to five specimens were tested for the experimental conditions. The single edge notched (SEN) specimens had the notch tip sharpened by sliding a razor blade across it, as recommended by the European Task Group on Facture (Williams and Cawood, 1990). The usual 0.13 mm notch tip radius was used for the Charpy test. This is a blunt notch and the values of energy measured with the Charpy specimens had an additional energy component for the initiation of the crack (Williams, 1980; Williams and Hodgkinson, 1981). Therefore, the fracture energy values derived from both tests are not directly comparable. Nevertheless, they will serve as a qualitative parameter for comparison of the fracture mechanisms of the neat resin and its alumina composite.

For the TPB slow test the total energy consumed at failure was calculated by integrating the area under the stress-strain curve. For the impact test condition the absorbed energy was directly read from the testing machine dial. The values thus obtained were corrected to windage and friction in the pendulum bearings the procedure established by the ASTM Standard D-256.

The topography of the fracture surfaces were analyzed by scanning electron microscopy (SEM) at 15-20 kV with secondary electrons imaging. The fractured specimens were gold sputtered before the SEM analysis in order to avoid charging.

Experimental Results

The composite density measured was $\rho_c = 1380$ kg/m3 and the filler and void volume fractions, calculated from Eqs. (1) and (2) respectively, were $V_f = 8\%$ and $V_V \approx 0\%$. This low void volume fraction is in good agreement with the microstructure observed by reflected light optical microscopy (Costa and d' Almeida, 1993). The energy values obtained from the impact and TPB slow tests are listed in Table 1, along with the derived values of the fracture toughness parameter (see the discussion below).

Nomenclature

a = crack length
c = specific heat
k = thermal conductivity
k_1 = contact stiffness
k_2 = specimen stiffness
m = mass
t = time
u_1 = energy lost by the striker
u_2 = energy gained by the specimen
v = velocity
B = thickness
x = crack length/specimen width ratio
G = strain energy release rate
K = stress intensity factor
L = test span
M = mass fraction
U = total energy at fracture
U_0 = kinetic energy term
V = volume fraction
W = width
ϕ = calibration factor
α = contact stiffness/specimen stiffness ratio
ρ = density
ω = natural frequency
ΔT = temperature change

sub-indexes

c = composite
f = filler
m = matrix
v = void
Ic = critical value for mode I fracture toughness

Table 1 Absorbed Energy at Fracture (U, 10^{-2}J) and Derived Values for the Strain Energy Release Rate (G, kJ/m^2)

	Matrix		Composite	
	U	G	U	G
TPB	0.41	0.08	0.54	0.12
Impact	27.0	1.46	13.0	0.10

Analysis and Discussion

Under the high strain rate imposed at the impact tests, the fracture toughness can be determined from the following equation (Williams and Hodgkinson, 1981; Low and May, 1989)

$$U = GBW\phi + U_0 \tag{3}$$

U is the global energy consumed at the impact test, i.e., the value measured at the test machine dial, and U_0 is a term related with the kinetic energy, namely:

$$U_0 = \frac{1}{2}\pi m v^2 \tag{4}$$

where m is the mass of the specimen and v the test velocity. In Eq. (3), B and W are, respectively, the thickness and the width of the specimen, cf. Fig. 1, and ϕ is a calibration factor.For small cracks it is given by (Birch and Williams, 1978)

$$\phi = \frac{1}{2}x + \frac{1}{18\pi}\cdot\frac{L}{W}\cdot\frac{1}{x} \tag{5}$$

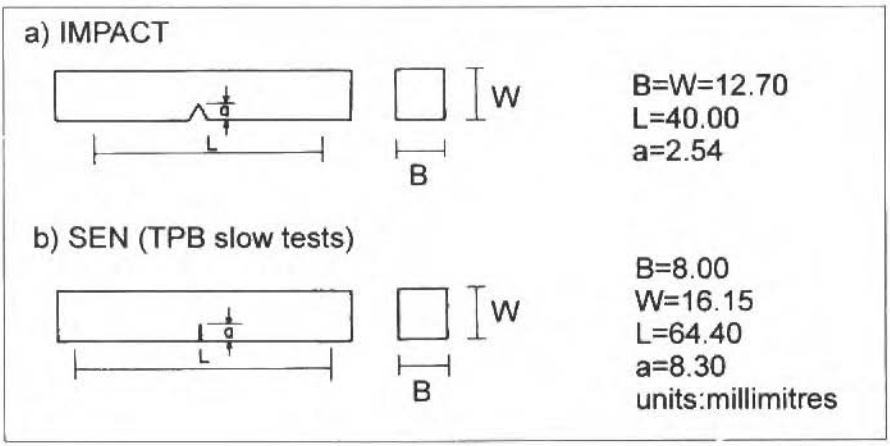

Fig. 1 Geometry and dimensions, in millimeters, of the test specimens

where L is the test span and x is the ratio between crack length, a, and specimen width, namely: x = a/W.

The values of G calculated from Equs. (3) to (5) are shown in Table 1. For the slow TPB tests, U_0 is small and can be disregarded. As it is shown in Table 1, under the test conditions used at this work, a strong change for the G value was derived for the resin matrix. The results obtained show that the neat resin fracture behavior is strongly affected by the strain rate of the tests. On the other hand, the values derived for the composite are almost constant and independente on the strain rate of the tests.

As said before, the values of G derived from SEN and impact specimens are not straightforward comparable because the impact speciments had a blunt notch. Nevertheless, it can be seen from Table 1 that it occurs a strong increase in the energy absorbing capacity of the neat resin in relationship to the also blunt notched composite specimens. The high energy value quoted for the neat resin could be due to the dynamic character of the test (Williams, 1987; Williams and Adams, 1987). As showed by Williams and Adams (1987) an apparent increase in toughness is obtained for short loading times, as in an impact test. Under dynamic conditions both the force and the energy measured are dependent on the contact stiffness, k_1, between the striker and the specimen. The energy lost by the striker, u_1, and that gained by the specimen, u_2, had the following relationships (Williams and Adams, 1987):

$$u_1 = \left(\frac{\alpha+1}{\alpha}\right)u_2 + \frac{\alpha}{2}\frac{(2\alpha+1)}{(\alpha+1)^2}mv^2 \pm \sqrt{2/\alpha+1}\sqrt{u_2}\sqrt{mv^2}, \quad (6)$$

for $\sin \omega t = \pm 1$ and $\cos \omega t = 0$;

$$u_1 = \left(\frac{\alpha+1}{\alpha}\right)u_2 + \frac{2\alpha^2}{(\alpha+1)^2}mv^2, \quad (7)$$

for $\sin \omega t = 0$ and $\cos \omega t = +1$; and

$$u_1 = \left(\frac{\alpha+1}{\alpha}\right)u_2, \quad (8)$$

for $\sin \omega t = 0$ and $\cos \omega t = -1$

where α is the ratio between the contact stiffness and the specimen stiffness, k_2, i.e., $\alpha = k_1/k_2$. In Eqs. (6) to (8), ω is the natural frequency of the test system and t is the time. The boundary conditions arise from considering that the interaction between the specimen and the striker is governed by a mass-spring model (Williams, 1987).

Equation (6) is plotted as u_1/mv^2 vs u_2/mv^2 in Fig. 2. It must be highlighted that the other equations, say Eqs. (7) and (8), gave results with the same trend as the one obtained by using Eq. (6). For the sake of clarity only the trend obtained by Eq. (6) is showed in Fig. 2. It can be seen that for $\alpha > 10$ the energy lost by the striker is approximately equal to the energy gained by the specimen, $u_1 \approx u_2$. This result means that the value of energy measured reflects a real material behavior for α values greater than 10. For polymers, in general, α can be taken as close to 10 (Williams and Adams, 1987). Therefore, the calculated increase of the G parameter reflects a strong difference in the polymer behavior under impact conditions.

The analysis of the composite fracture surface reveals that crack pinning by the alumina particles, Fig. 3a and b, is the main toughness mechanism acting at the composities at both test conditions. As shown in Fig.3, characteristic tails are developed at the alumina particles lying at the fracture surface. The position of the tails left behind the particles, shows that a good interfacial adhesion was developed between the particles and the matrix (Kinloch, Maxwell and Young, 1985). At Fig.3 it is also shown that, in fact, the alumina particles formed clusters that are uniformly distributed throughout the matrix and that have a mean size of about 45 μm. Figure 3b depicts with greater magnification the process of crack pinning. It can be seen that the crack path is locally perturbed by the clusters, which act as pin points for the crack until enough energy is stored to break the crack away.

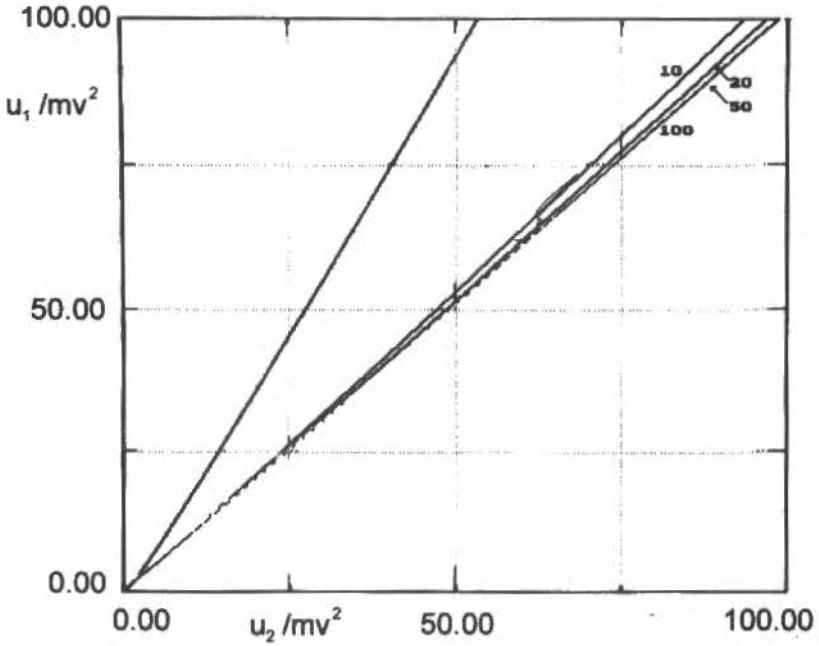

Fig. 2 The variation of the energy lost by the striker, u_1, against the energy gained by the specimen, u_2, as a function of α. The curves for α = 50 and α = 100 are not distinguishable at the graphic scale used

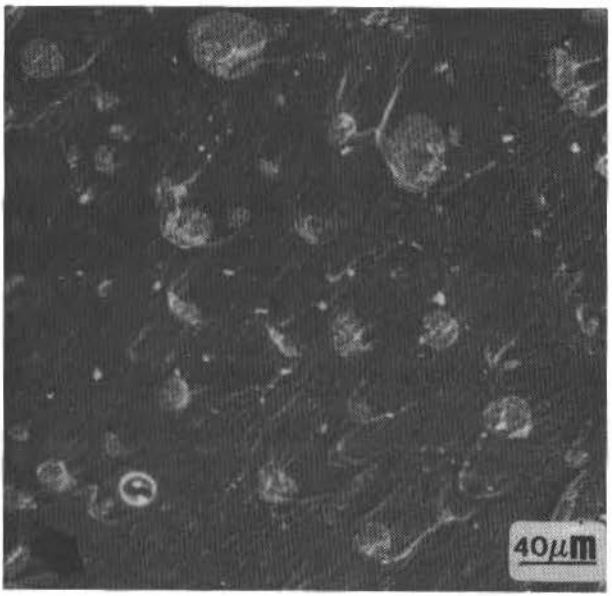

Fig. 3a Crack pinning by the agglomerates of alumina particles. The arrows show the direction of fracture propagation. Impact tested specimen. 100x

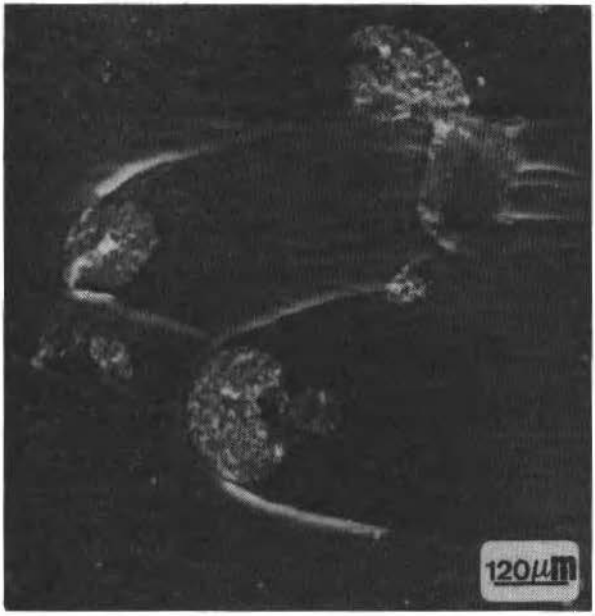

Fig. 3b Crack pinning by the agglomerates of alumina particles. The arrows show the direction of fracture propagation. Impact tested specimen. 300x

For the neat resin a strong change at the fracture surface morphology was observed depending on the strain rate of the test. The neat resin fracture associated with the slow speed test is almost entirely featureless, as shown in Fig.4a. The crack propagation occurs mainly on a single plane without large occurrence of crack branching. Therefore, a small amount of energy is consumed during crack propagation. On the other hand, many tear marks are observed at the neat resin fracture surface developed under the impact test condition, Fig.4b and 4c. This morphology is characteristic of localized plastic deformation (Low and May, 1989) and its presence shows that crack tip blunting is taking place.

Blunting of the crack tip of polymers has been associated with an adiabatic heating process developed at the crack tip under impact conditions (Weichert and Schonert, 1974; Williams and Hodgkinson, 1981; Clutton and Williams, 1981). The temperature rise due to the adiabatic heating is given by the equation (Williams and Hodgkinson, 1981):

$$\Delta T = \frac{G}{(\pi \rho c k t)^{1/2}} \qquad (9)$$

where c is the epecific heat, k the thermal conductivity and t the loading time.

For the neat epoxy resin the temperature change, ΔT, was calculated to vary between 42 and 66 °C. These values were obtained using c = 0.40 cal/g. °C (Dean, 1973), k = 0.20 W/m.K (Low and May, 1989) and t varying between 0.4 and 1 milliseconds. The Δ T values are high enough to bring the crack tip temperature close to the glass transition temperature, of obout 100 °C (Low and may, 1989), for the epoxy resin. This should induce localized crack tip plastic deformation and agrees with the topographic marks shown in Fig.4b.

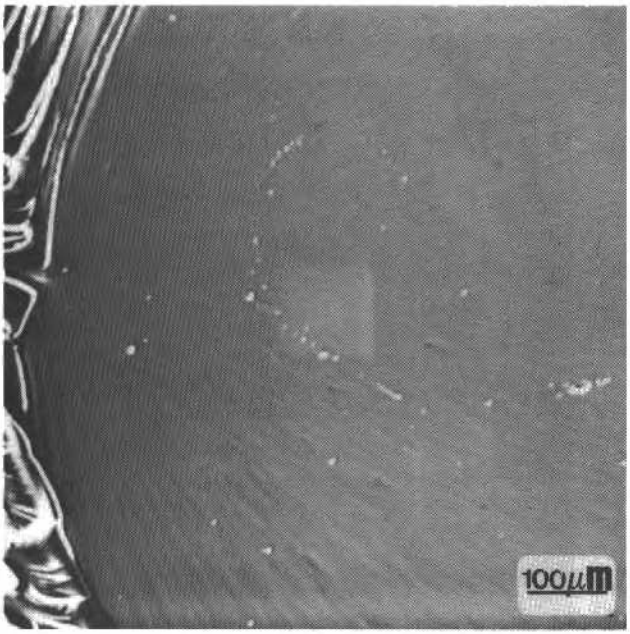

Fig. 4a Neat resin fracture surfaces. a) Featureless fracture topography developed at high strain rate tests conducted under low strain rate, $5x10^{-4}$ s^{-1}.

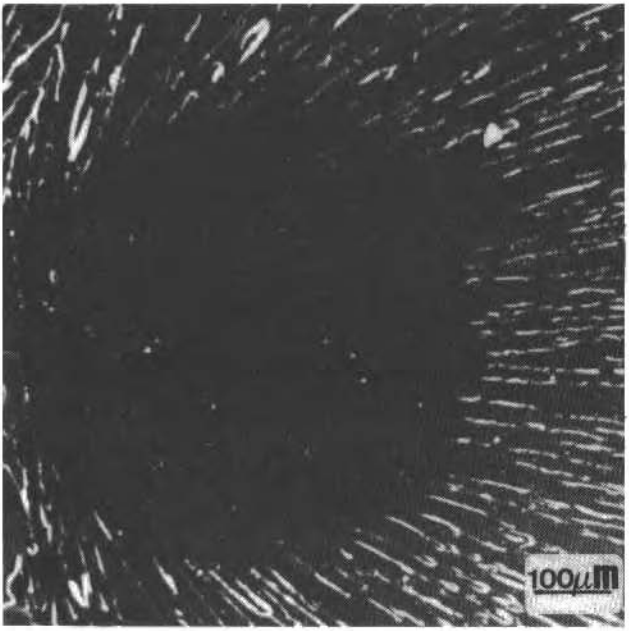

Fig. 4b Neat resin fracture surfaces. Tear marks developed at high strain rate tests, 150 s^{-1}

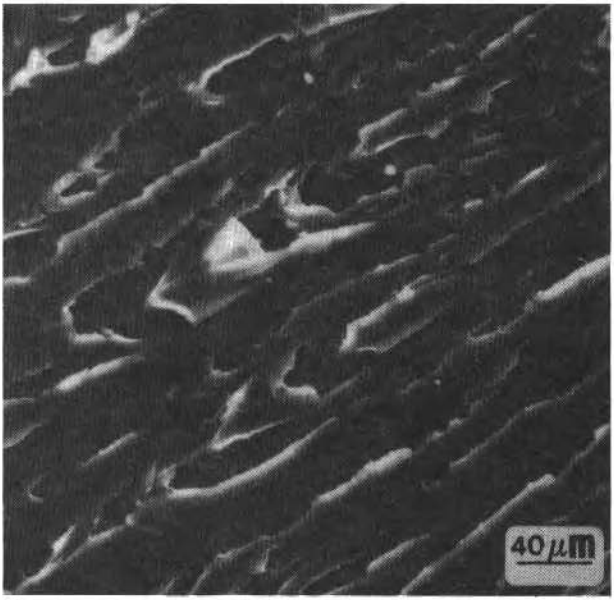

Fig. 4c Tear marks developed at high strain rate tests, 150 s^{-1}

In order to calculate the temperature change for the composite, both the specific heat and the thermal conductivity of the composite were evaluated by using rule of mixture equations (Chawla, 1987). The calculated values were k = 0.251 W/m.K and c = 0.38 cal/g. °C. These values were obtained using for the alumina powder the following parameters: k = 30 W/m.K (Shackelford, 1985) and c = 0,198 cal/g. °C (Dean, 1973).

The change in temperature for the composite was calculated to be less than 4 °C. With this very low temperature rise, the temperature excursion at the crack tip of the composite is not able to induce any thermal blunting. Therefore, the fracture resistance ability of the alumina particle composite is restrict to crack pinning. From the experimental results obtained, cf. Table 1, it can be inferred that the energy absorbing capacity of this mechanism was not affected by the externally imposed strain rate.

Conclusions

- Both at high and low strain rates, crack pinning was identified as the fracture toughness mechanism for the alumina particle epoxy matrix composite studied at this work.
- The neat resin matrix fracture behavior is strongly dependent upon the applied strain rate.
- At impact test conditions the neat resin shows a strong increase in fracture toughness. This behavior is related to the development of an adiabatic heating process that causes crack tip blunting.

Acknowledgments

The authours acknowledge the financial support from the Brazilian Minister od Science and Technology (MCT) and The State Foundation for the Development of the North Region of the State of Rio de Janeiro (FENORTE).

References

Bandyopadhyay, S., 1990, "Review of the Microscopic and Macroscopic Aspects od Fracture of Unmodified and Modified Epoxy Resins", Materials Science and Engineering, Vol.A125, pp. 157-184.

Bandyopadhyay, S., Pearce, P.J., and Mestan, S.A., 1985, "Crack-Tip Micromechanics and Fracture Properties of Rubber Toughned Epoxy Resins", Proceedings of the 6th Churchill College Conference on Deformation, Yield and Fracture of Polymers, paper 18, Cambridge, England.

Birch, M.W., and Williams, J.G., 1978, "The Effect of Rate on the Impact of Polymers", International Journal of Fracture, Vol.14, pp.69-84.

Bucknall, C.B., and Gilbert, A.H., 1989, "Toughening Tetrafunctional Epoxy Resins Using Polyetherimide", Polymer, Vol.30, pp.213-217.

Chawla, K.K., 1987, "Composite Materials: Science and Engineering", Springer-Verlag, New York.

Clutton, E.O., and Williams, J.G., 1981, "On the Thermal Blunting of Crack Tips in Polymers", Journal of Materials Science, Vol.16, pp.2583-2589.

Costa, F.H.M.M., and d' Almeida, J.R.M., 1993, "Uniaxial Compression Mechanical Behavior of an Alumina-Epoxy Composite", Journal of the Brazilian Society of Mechanical Sciences, Vol.15, pp.199-207.

Dean, J.A., 1973, Lange's Handbook of Chemistry, 11 th edition, McGraw Hill Book Company, New York.

Kinloch, A.J., Maxwell, D.L., and Young, R.J., 1985,. "The fracture of Hybrid-Particulate Composites", Journal of Materials Science, Vol.20, pp.4169-4184.

Lange, F.F., and Radford, K.C., 1971, "Fracture Energy of an Epoxy Composite System", Journal of Materials Science, Vol.6, pp. 1197-1203.

Low, I.M., and Mai, Y.W., 1988, "Micromechanisms of Crack Extension in Unmodified and Modified Epoxy Resins", Composites Science and Technology, Vol.33, pp.191-212.

Low, I.M., and Mai, Y.W.,1989, "Rate and Temperature Effects on Crack Blunting Mechanisms in Pure and Modified Epoxies", Journal of Materials Science, Vol.24, pp.1634-1644.

Schoutens, J.E., 1984, "Simple and Precise Measurements of Fibre Volume and Void Fractions in Metal Matrix Composite Materials", Journal of Materials Science, Vol.19, pp.957-964.

Shackelford, J.F., 1985, Introduction to Materials Science for Enginners, MacMillan Publishing Company, New York.

Weichert, R., and Schonert, K., 1974, "On the Temperature Rise at the Tip of a Fast Running Crack", Journal of The Mechanics and Physics of Solids, Vol.22, pp. 127-133.

Williams, J.G., 1980, "Modelling Crack Tip Failure Mechanisms in Polymers", Metal Science, Vol.14, pp.344-350.

Williams, J.G., 1987, "The Analysis of the Dynamic Fracture Using Lumped Mass-Spring Models", International Journal of Fracture, Vol.33, pp.47-59.

Williams, J.G. and Adams, G.C., 1987, "The Analysis of instrumented Impact Tests Using a Mass-Spring Model", International Journal of Fracture, Vol.33, pp.209-222.

Williams, J.G., and Cawood, M.J., 1990, "European Group on Fracture: K_c and G_c Methods for Polymers", Polymer Testing, Vol.9, pp.15-26.

Williams, J.G., and Hodgkinson, J.M., 1981, "Crack Blunting Mechanisms in Impact Tests on Polymers", Proceedings of the Royal Society of London, Vol.A375, pp.231-248.

RBCM - J. of the Braz. Soc. Mechanical Sciences
Vol. XVII - nº3 - 1995 - pp. 278-291

ISSN 0100-7386
Printed in Brazil

Achieving Ultra-Precision by Mechatronics: Active Air Journal Bearing

Oswaldo Horikawa
Department of Mechanical Engineering
Escola Politécnica of São Paulo University
Av. Prof. Mello Moraes, 2231, Cidade Universitária
05508-900 São Paulo, SP Brasil

Kaiji Sato
Akira Shimokohbe
Precision and Intelligence Laboratory
Tokyo Institute of Technology
4259, Nagatsuda, Midori-ku, Yokohama 227, Japan

Abstract

Aiming bearings of: ultra-precision, infinite stiffness, high vibration damping capability and new functions (axis positioning and dynamic stiffness control), the authors present in this paper an "active air journal bearing" AAJB, a novel type of bearing, capable of precisely controlling the radial position of its axis. The AAJB that is the result of the application of concepts of the mechatronics, utilizes non-contact sensors to detect the radial position of the axis, non-contact actuators (movable air pads driven by piezo-electric actuators) to support and drive the axis, and a controller to regulate the whole system. In the paper, the basic configuration of the AAJB as well as its dynamic model and the controller design is shown. The stiffness and the positioning characteristics of the AAJB are examined and a method of compensating motion errors caused by profile error of the axis and bearing parts is presented. By experiments, it is shown that the AAJB has: an almost infinite static stiffness and an increased damping capability, a band-width of more than 1 KHz and an absolute rotary motion accuracy of better than 21 nm with the axis rotating at 750 rpm.
Keywords: Air Bearing, Mechatronics, Active Air Journal Bearing.

Introduction

Air bearings are machine elements widely used in the field of precision engineering, such as, the fabrication of ICs, data storage media, high precision machine tools and measuring machines. This is due to the advantage of air bearings such as high accuracy and extremely low friction. However, they show problems like: (1) vibration due to the low stiffness and the lack of damping capability as well as (2) motion inaccuracies due to profile error of the axis and bearing parts. The conventional approach to solve these problems was based on the development of new methodologies to design and manufacture bearings and their components. On the other hand, there is the "mechatronic" approach, i. e., the use of electronic and electro-mechanical techniches to solve mechanical problems. In recent years, the feasibility of solutions obtained from mechatronics point of view is increasing, since the cost of electronic components, actuators, sensors as well as micro-processors is decreasing while their quality is increasing. Thus the authors adopted the approach of mechatronics to obtain air bearings of better characteristics and proposed the "active air bearing" AAB (Aoyama, Watanabe and Shimokohbe, 1987). In the AAB, a non-contact actuator supports and drives an axis, a non-contact sensor detects the axis position and a controller regulates the whole system. The non-contact actuator is a combination of a conventional passive air bearing mechanism (PAB, an air pad plus a pressurized air film) and a piezoelectric actuator (PEA). Such an AAB is capable of executing a precise and quick positioning of the axis, making the improvement of the bearing stiffness, damping capability and motion accuracy possible. The effectiveness of the AAB was demonstrated in past work, in which AABs were utilized to compensate for linear motion errors of an air slide table (Aoyama, Yamaguti, Osada and Shimokohbe, 1989). This paper presents a bearing which by using four AABs, 7nged around a rotating axis, can control axis motion in two radial directions. This bearing, called "active air journal bearing" AAJB (Horikawa and Shimakohbe, 1990) is the first step in the development of a rotary bearing featuring ultra-precision, infinite static stiffness, high vibration damping capability and new functions such as axis positioning and dynamic stiffness control, i. e. a function to increase or decrease the bearing stiffness at an arbitrary frequency (Horikawa, Yasuhara, Osada and Shimokohbe, 1991).

Manuscript received: July 1994. Technical Editor: Agenor de Toledo Fleury

Principle

Configuration of the AAJB

Figure 1 shows the mechanical configuration of the AAJB. The axis (diameter 100 mm, height 84 mm) is supported without mechanical contact by four air pads (air film thickness 20 μm, supply pressure 0.4 MPa). These air pads are connected to the body through springs (elastic hinges) and they can move in the x or y direction.

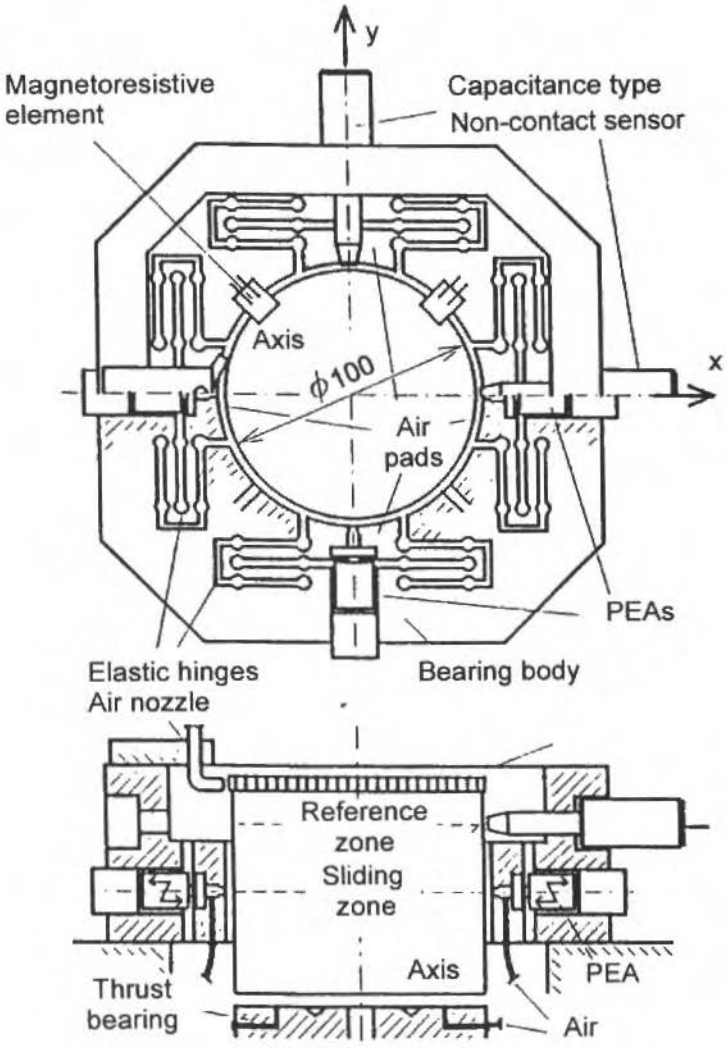

Fig. 1 Mechanical configuration of the AAJB

A PEA is inserted between the body and each air pad. Each PEA and air mechanism, i. e., noncontact actuator, drives the axis in the x or y direction through the pressurized air film. The radial position of the axis is measured by capacitance micrometers installed in both directions and their output are sent to controllers.

The axis is rotated at a constant speed by a turbine (diameter 100 mm), installed in the top face of the axis, and two air nozzles. Each time the axis completes a revolution, two non-contact magnetoresistive elements generate 400 pulses. Using these pulses, the angle of rotation of the axis is measured.

Motions of the axis in one direction is assumed to be independent of that in the other direction, since only relatively small displacements are to be considered. Therefore, motions in the x and y directions are controlled independently.

The AAJB model

A simplified axis dynamic model in the x direction is shown in Fig. 2, where M is the axis mass, K the stiffness of the air film, C the damping coefficient of the air film, d_x the disturbance force, x the displacement of the axis, x_r the reference signal, u_x the displacement of the PEA, k_s the sensor gain, k_s' the coefficient to convert the displacement x_r into voltage ($k_s = k_s'$). The model in the y direction is the same, because of the symmetry of the AAJB mechanism. A corresponding block diagram is shown in Fig. 3. The transfer function between the input voltage to the PEA driver and the axis displacement is decomposed into $G_1(s)$ and $G_2(s)$; $G_2(s)$ denotes the transfer function from the force d_x to the axis position x and $G_1(s)$, the remainder (Horikawa and Shimokohbe, 1990).

$$G_1(s) = \frac{k_p}{(1+Ts)} \frac{\omega_n^2}{s^2 + 2\zeta\omega_n s + \omega_n^2} (2Cs + 2K) \tag{1}$$

$$G_2(s) = \frac{1}{Ms^2 + 2Cs + 2K} \tag{2}$$

The controller is composed of the 2DOF (two degrees of freedom) controller, a band-pass filter ($F_B(s)$) and a repetitive controller. The 2DOF controller is composed of controller $F_1(s)$ of PID type (Eq. (1)) and $F_2(s)$ of PDD^2 type (Eq. (2) (Aoyama et al., 1989).

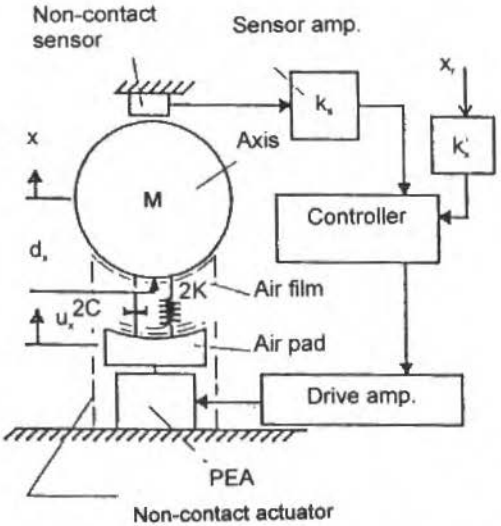

Fig. 2 Dynamic model of the AAJB (x direction)

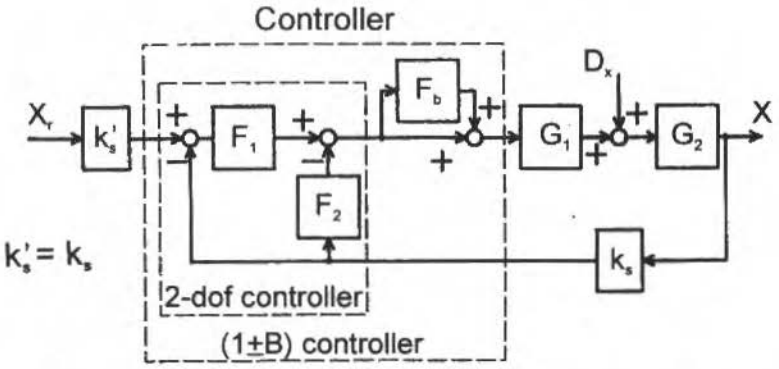

Fig. 3 Block diagram of the AAJB with the 2DOF and the (1 + b) controller

$$F_1(s) = \beta_1 + \frac{\gamma}{s} + \frac{\alpha_1 s}{(1 + T_\alpha s)} \tag{3}$$

$$F_2(s) = \beta_2 + \frac{\alpha_2 s}{(1 + T_\alpha s)} + \frac{\xi s^2}{(1 + T_\xi s)} \tag{4}$$

Where T_α and T_X, are time constants necessary to realize differentiators D and D^2. Considering the 2DOF controller, the compliance characteristics (characteristics from the disturbance force to the axis position, inverse of stiffness) and the reference characteristics (characteristics from the reference input to the axis position) of the AAJB are as follows

$$\frac{X(s)}{D_x(s)} = \frac{G_2(s)}{1 + k_s G(s) F(s)} \tag{5}$$

$$\frac{X(s)}{X_r(s)} = \frac{k_s' G(s) F_1(s)}{1 + k_s G(s) F(s)} \tag{6}$$

where $F(s) = F_1(s) + F_2(s)$ and $G(s) = G_1(s)\, G_2(s)$. These characteristics are designed as follows:

(i) F(s) is determined so as to decrease the gain of the compliance characteristics as much as possible unless the system becomes unstable;

(ii) Keeping F(s) at the above determined value, $F_1(s)$ and $F_2(s)$ are chosen so as to optimize the reference characteristics.

Thus each characteristics can be designed almost independently of the other. This is the reason for the name 2DOF controller.

$F_b(s)$ is a band-pass-filter (BPF) used to execute the dynamic stiffness control (Horikawa et al., 1991), i. e., a function to increase or decrease the bearing at an arbitrary frequency. By increasing the stiffness at the rotation frequency of the axis, it is possible to reduce vibrations caused by cyclic disturbance forces such as cutting forces or by an unbalance of the axis. Contrarily, by decreasing the stiffness at the rotation frequency, it is possible to rotate the axis around its center of inertia, reducing

vibrations caused by an unbalance of the axis. In both cases, this function improves the capability of the AAJB to reduce vibrations, namely to improve the axis rotation accuracy. The controller with $F_b(s)$ is called a (1 + B) controller.

The BPF has the following characteristics:

$$F_b(s) = k_b \frac{\frac{2\pi f_c}{Q} s}{S^2 + \frac{2\pi f_c}{Q} s + (2\pi f_c)^2} \tag{7}$$

Where f_c is the peak response frequency, k_b is the gain and Q a constant that determines the shape of the peak of the response curve of the filter. Considering the BPF, Eqs. (5) and (6) are modified as follows:

$$\frac{X(s)}{D_x(s)} = \frac{G_2(s)}{1 + k_s G(s) F(s) (1 + F_b(s))} \tag{8}$$

$$\frac{X(s)}{X_r(s)} = \frac{k'_s G(s) F_1(s) (1 + F_b(s))}{1 + k_s G(s) F(s) (1 + F_b(s))} \tag{9}$$

If $k_b > 0$, in the BPF (Eq. (7)), the denominator of Eq. (8) increases near f_c so that the compliance decreases, i. e., the bearing stiffness increase at this frequency. The opposite situation occurs and the stiffness decrease, when the filter output is inverted and $-1 < k_b < 1$. In both cases, at a sufficiently low or high frequency in comparison with f_c the magnitude of $F_b(s)$ approaches zero, assuring that the effect of the dynamic stiffness control appears only at frequencies near f_c. At other frequencies, the performance is the same as that obtained only by the 2DOF controller.

When the value of F(s) is large enough to satisfy the following condition, but not so large to make the system unstable, Eq. (9) reduces to Eq. (11).

$$\left| k_s G(s) F(s) (1 + F_b(s)) \right| >> 1 \tag{10}$$

Then, the effect of the dynamic control does not appear in the reference characteristics.

$$\frac{X(s)}{X_r(s)} \cong \frac{k'_s G(s) F_1(s) (1 + F_b(s))}{k_s G(s) F(s) (1 + F_b(s))} = \frac{F_1(s)}{F(s)} \tag{11}$$

The repetitive controller (Horikawa and Shimokohbe, 1990) is another that is added to the AAJB system in order to reduce rotation errors that have repeatability by means of a repetitive control strategy (Hara, Omata and Nakano, 1985). This controller is used together with the 2DOF controller as Fig. 4 shows, where, k_r is the gain of the repetitive control, i, the number of revolutions the axis has completed after repetitive control is activated and L_r, the period of the axis rotation. The repetitive controller executes the following algorithm:

(1) Samples the error $E_{r,i}$;

(2) Calculates the compensation signal:

$C_{r,i} = C_{r,i-1} + E_{r,i-1}/k_r$;

(3) Inputs $C_{r,i}$ to the 2DOF controller so as to cancel the rotation error.

Considering the repetitive controller, Eqs. (5) and (6) become as follows.

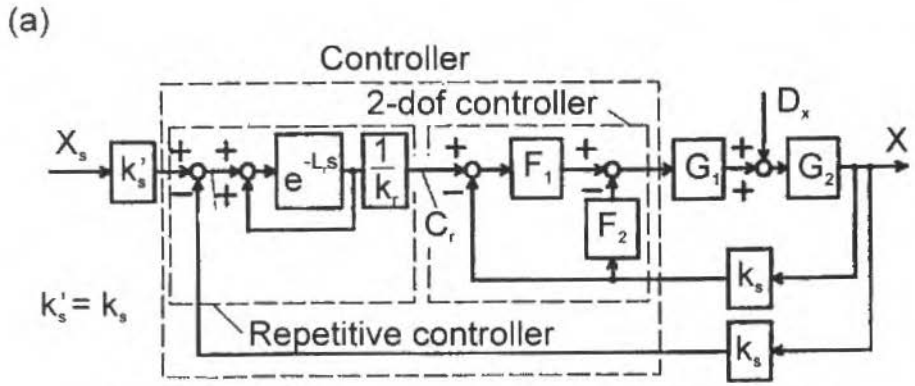

Fig. 4 Block diagram of the AAJB with the 2DOF and the repetitive controllers.

$$\frac{X(s)}{D_x(s)} = \frac{G_2(s)}{1 + k_{(s)} G(s) [F_1(s) (1 + F_r(s)) + F_2(s)]} \tag{8}$$

$$\frac{X(s)}{X_r(s)} = F_r(s) \frac{k_s' G s) F_1(s)}{1 + k_s G(s) [F_1(s) (1 + F_r(s)) + F_2(s)]} \tag{9}$$

where $F_r(s) = \dfrac{e^{-L_r s}}{k_r\left(1 - e^{-L_r s}\right)}$

At frequencies $\omega = 2\pi k/L_r$ (k=0, 1, 2, ...)the term $e^{-L_r s}$ approaches unity and the compliance characteristics approximates zero and the reference characteristics, unity.

Control of absolute rotary motion accuracy

In order to achieve a high absolute motion accuracy, profile error of two parts of the axis (Fig. 1) is considered in the AAJB: profile error of the axis sliding zone, i. e., the axis part (including the air pads) where the pressurized air film is produced, and the profile error of the axis reference zone, i. e., the axis zone where the sensors measure the axis position (or motion).

When the axis is rotating, the profile error of the axis sliding zone gives rise to changes in the film thickness and consequently in the radial force that acts on the axis. Therefore motion errors caused by the profile error of the axis sliding zone can be reduced by the 2DOF and repetitive controllers.

However the profile error of the reference zone is added to the sensor feedback signal and, for this reason, it is necessary to measure and compensate for this error. So, in the AAJB, the profile error of the axis reference zone is first measured and then the measured error sent to the 2DOF controller, as is reference signal (x_r), eventually using also a repetitive controller when the axis is rotated at a relatively high speed. This compensation will be referred to below as roundness compensation.

Table 1 System Parameters

M (kg)	K (Nm^{-1})	ζ	k_n ($\mu m V^{-1}$)	C ($N\,s\,m^{-1}$)	ω_n ($rad\,s^{-1}$)	k_s ($V\mu m^{-1}$)	T (s)
5.05	7.54×10^6	0.77	0.93	1.22×10^3	7.04×10^3	2	3.8×10^{-4}

System dynamics and design

After measuring parameters of the transfer functions $G_1(s)$ and $G_2(s)$ (Horikawa et al., 1990) (Table 1) and making $k_s = 2\ V\mu m^{-1}$, parameters of the 2DOF controller were designed simulating characteristics of the AAJB according to Eqs. (5) and (6). The designed controller (Table 2) gave an improved compliance characteristics and a reference characteristics with a band-width of approximately 1KHz (Horikawa et al., 1990).

Experimental Results

Figure 5 shows the experimental AAJB (the air turbine, the air nozzles and magnetoresistive elements have yet to be installed). Initially, experiments were done without the axis rotation.

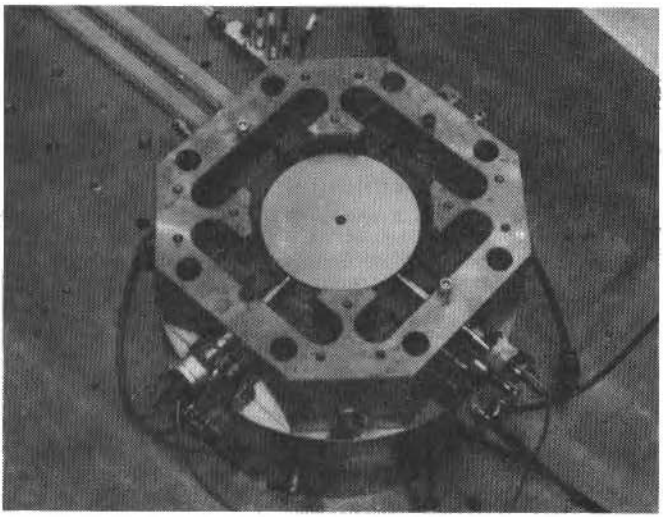

Fig. 5 Prototype of the AAJB

Table 2 Controller Parameters

	$\beta_1 = 0.47$		$\alpha_1 = 5.10\times10^4$
P:	$\beta_2 = 1.12$	D:	$\alpha_2 = 2.72\times10^4$
	$\beta = 1.59$		$\alpha = 7.83\times10^4$
I:	$\gamma = 5.30\times10^3$	D^2:	$\xi = 1.00\times10^8$
$T_\alpha =$	7.00×10^{-3}s	$T_\xi =$	7.00×10^{-3}s

Compliance characteristics

Figure 6 shows outputs of the x and y sensors with no intentional disturbance forces. Figure 6(a) is the case of the uncontrolled bearing (PAB). Here the axis vibrates continuously with amplitudes of about 60 mm mainly because of the air flow from the air supply ports. In the AAJB with the 2DOF controller, amplitudes were decreased to less than 15 nm (Fig. 6(b)). Since the air flow in the PAB and in the AAJB were the same, the reduction means improvement in the bearing stiffness and damping capability.

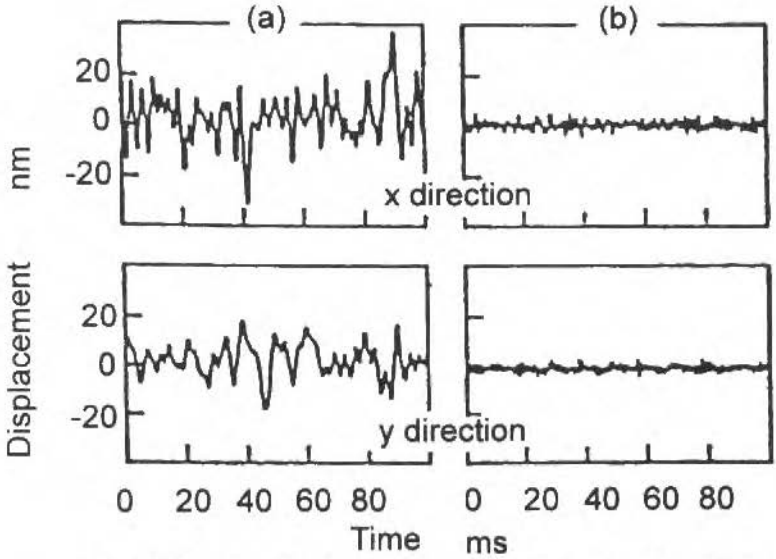

Fig. 6 Vibrations of the axis (0 rpm): (a) PAB (b) AAJB with 2DOF controller

Figure 7 shows experimental compliance characteristics in the x direction. Compared to the case of the PAB (curve(1)) an overall reduction in the compliance, i. e., increasing in the stiffness is obtained in the AAJB (curve (2)). Curve (3) is the case of the AAJB with the (I + B) controller executing the dynamic stiffness control at 275 Hz and increasing the bearing at the frequency, 50 times in comparison with the case of the PAB.

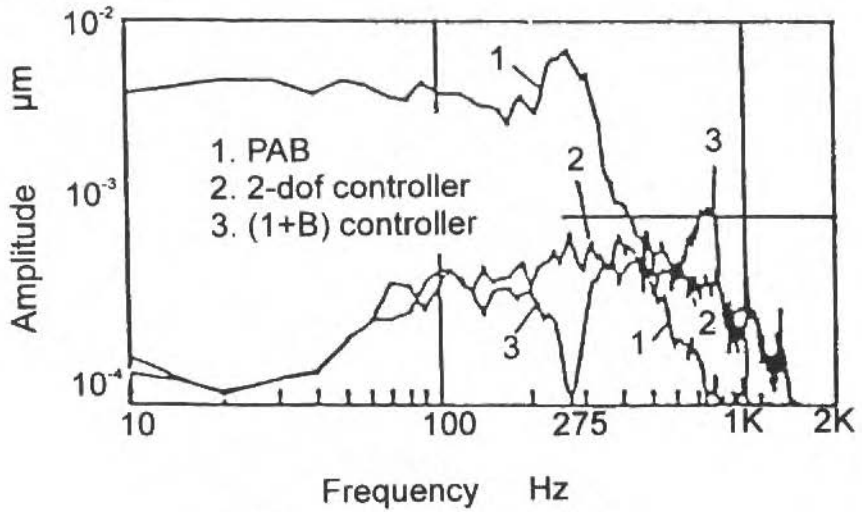

Fig. 7 Compliance characteristics (x direction)

Figure 8 shows responses to a 43 N static force applied diagonally to the axis. While in the PAB (Fig. 8 (a)), the force caused an axis displacement of more than 2μm in the x and y directions, in the AAJB (Fig. 8 (b)) the axis kept a same steady state position even with the force applied, demonstrating the infinite static stiffness of the AAJB.

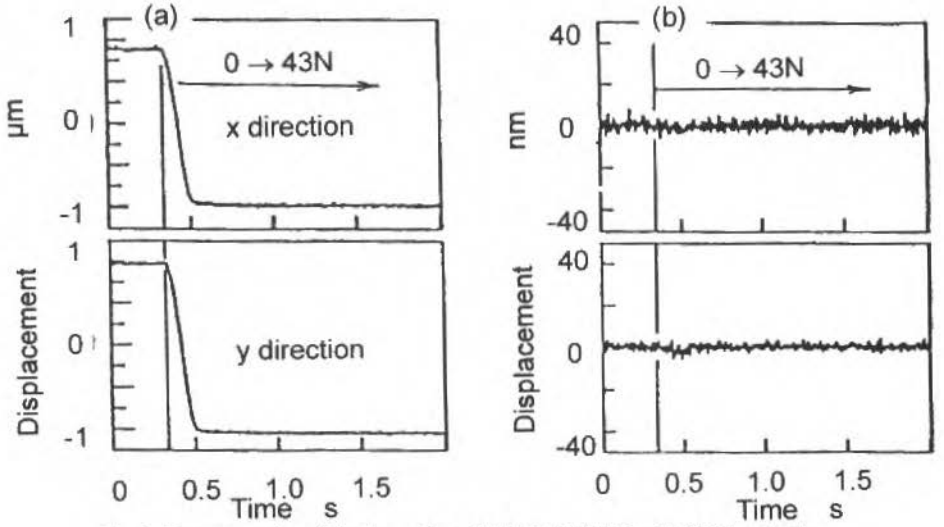

Fig. 8 Responses to a disturbance force (a) PAB; (b) AAJB with 2DOF controller

Reference characteristics

Figure 9 shows experimental (solid lines) and calculated (dashed lines) responses of the AAJB to 0.1μm step inputs. Experimental responses agreed well with calculated ones and showed that the AAJB is capable of positioning the axis precisely and quickly giving a response which corresponds to a band-width of 1 KHz. Figures 10 and 11 are positioning executed in the AAJB and show respectively a positioning resolution of less than 10 nm and capability of positioning its axis along at least 8μm in both directions.

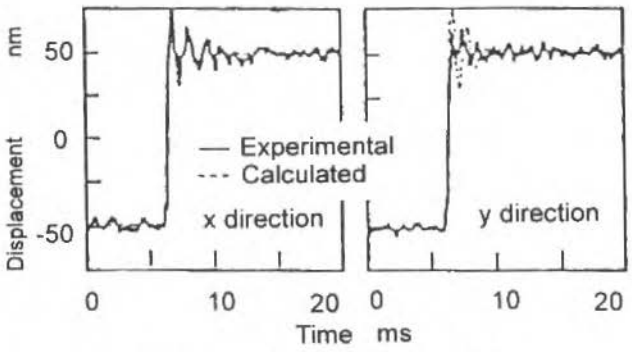

Fig. 9 Responses to 0.1μm step input

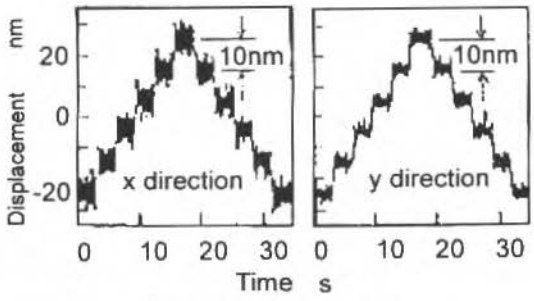

Fig. 10 10 nm positionings

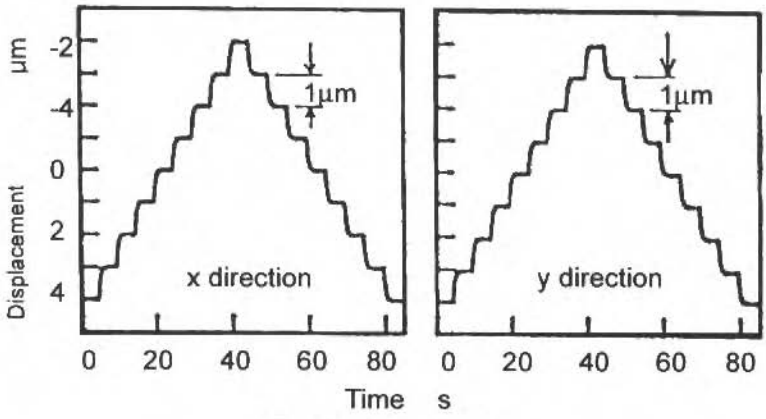

Fig. 11 1μm positionings

AAJB performance with the axis rotating

In the next experiments, the axis was rotated at a constant speed of 1000 rpm by the air turbine installed in the axis. The AAJB was controlled using the axis as the motion reference.

Figure 12 shows rotary motion errors of the axis. In the PAB (Fig. 12 (a)), errors were of approximately 0.3μm . In the AAJB with the 2DOF controller (Fig. 12 (b)), these errors were reduced to approximately 0.1μm in both directions, vibrations remaining with repeatability. However, such vibrations were reduced to less than 25 nm by the repetitive controller (Fig. 12 (c)). Figure 13 shows motion errors of the axis with a 12g unbalance mass, fixed on the upper surface of the axis at 21 mm from the center. The unbalance mass caused cyclic vibrations of more than 3μm in both directions in the PAB (Fig. 13 (a)). However, the vibrations were reduced to less than 0.1μm by the 2DOF controller (Fig. 13 (b)) and to less than 25 nm, by the repetitive controller (Fig. 13 (c)).

Figure 14 shows 0.1μm positionings of the axis rotating at 1000 rpm in the AAJB with the 2DOF and repetitive controllers. Quick and precise positionings were achieved and no interference between the axis motion in either direction was observed.

Control of absolute rotary motion accuracy

In the above experiments it was assumed that sensor signals express the rotary motion accuracy. However the axis reference zone has profile error and it had to be measured and compensated to obtain a high absolute rotary motion accuracy. The profile error of the axis was measured by the "improved reversal method" (Shimokohbe, Horikawa and Sata, 1991) (IRM), proposed by the authors. Using an auxiliary reference (a cylindrical master), set on the object to be measured, by the IRM it is possible to precisely measure the profile error of the object and the absolute rotary motion error of the rotary mechanism, without the necessity of reversing the object to the measured.

Some experiments were done with the axis rotating at a relatively low speed of 75 rpm. Figure 15 shows absolute rotary motion errors of the axis in the x direction. Since similar results were obtained in the y direction, only results of the x direction will be shown. In the case of the PAB (Fig. 15 (a)), absolute rotary motion errors of 0.99μm were observed. These errors were reduced to 0.32μm by the 2DOF controller (Fig. 15 (b)). The result shown in Fig. 15 (b) is superposed to the profile error of the axis in Fig. 16. Since the control keeps constant the gap between the sensor and the axis surface, the rotary motion error has the inverted shape of the profile error. Figure 17 shows the rotary motion error after the roundness compensation. An absolute rotary accuracy of the better than 18 nm was achieved.

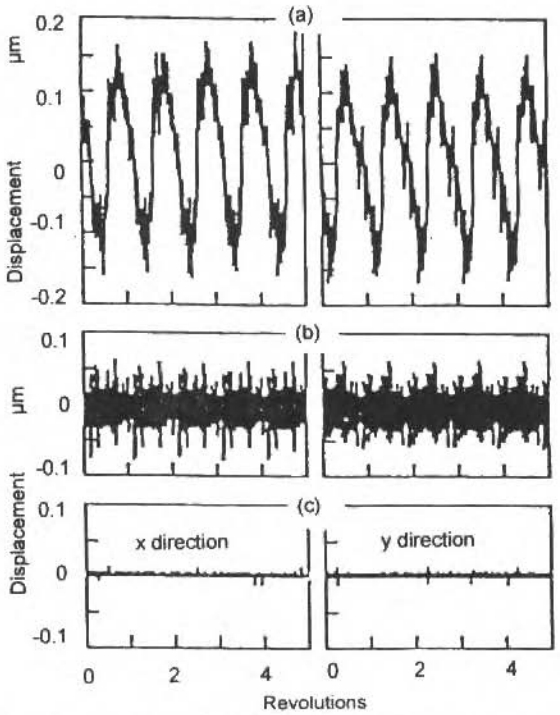

Fig. 12 Rotary motion errors (1000 rpm): (a) PAB; (b) AAJB with 2DOF controller; (c) AAJB with 2DOF and repetitive controllers

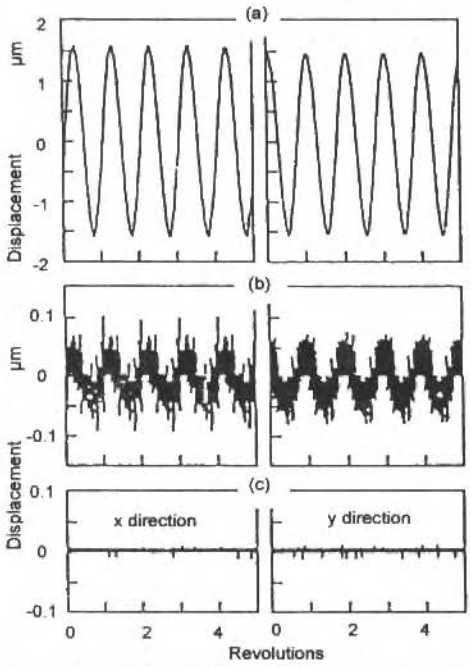

Fig. 13 Rotary motion errors (12g unbalance, 1000 rpm): (a) PAB; (b) AAJB with 2DOF controller; (c) AAJB with 2DOF and repetitive controllers.

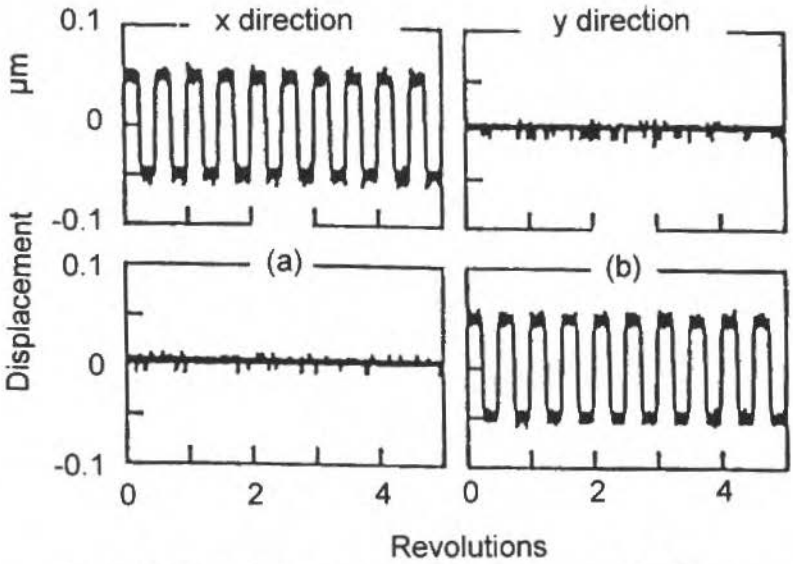

Fig. 14 Positionings of the rotating axis (1000 rpm): (a) x_r input; (b) y_r input

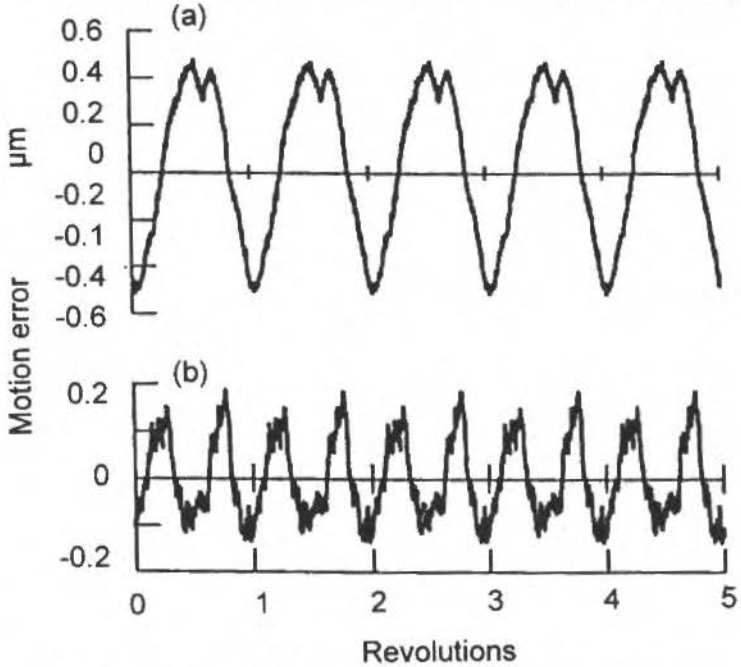

Fig. 15 Absolute rotary motion errors: (a) PAB; (b) AAJB with 2DOF controller.

Experiments were also done with the axis rotating at a relatively high speed of 750 rpm. In this case, absolute rotary motion errors of the PAB axis (Fig. 18 (a)) were of more than 1 μm . In the AAJB, since the roundness compensation was not executed, errors were reduced to 0.33 μm by the 2DOF controller (Fig. 18 (b)) and to 0.32 μm by the repetitive controller (Fig. 18 (c)), remaining errors being caused by profile errors being caused by profile error of the axis.

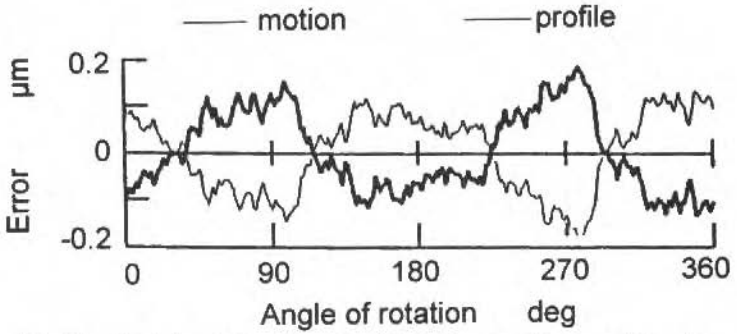

Fig. 16 Absolute rotary motion errors (75 rpm) and profile error of the axis

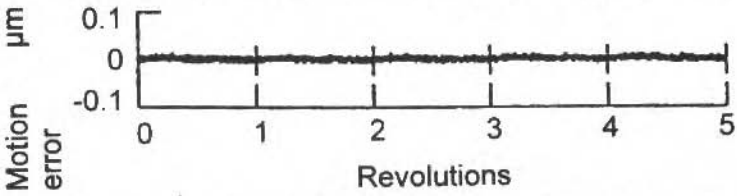

Fig. 17 Absolute rotary motion error of the AAJB with 2DOF controller and roundness compensation (75 rpm)

Figure 19 shows absolute rotary motion errors after the roundness compensation. When only 2DOF controller was used (Fig. 19 (a)), a satisfactory motion accuracy was not achieved and vibrations of 0.14 μm amplitude remained. However, vibrations were reduced and an absolute rotary motion accuracy of less than 21 nm was obtained by also using the repetitive controller (Fig. 19 (b)).

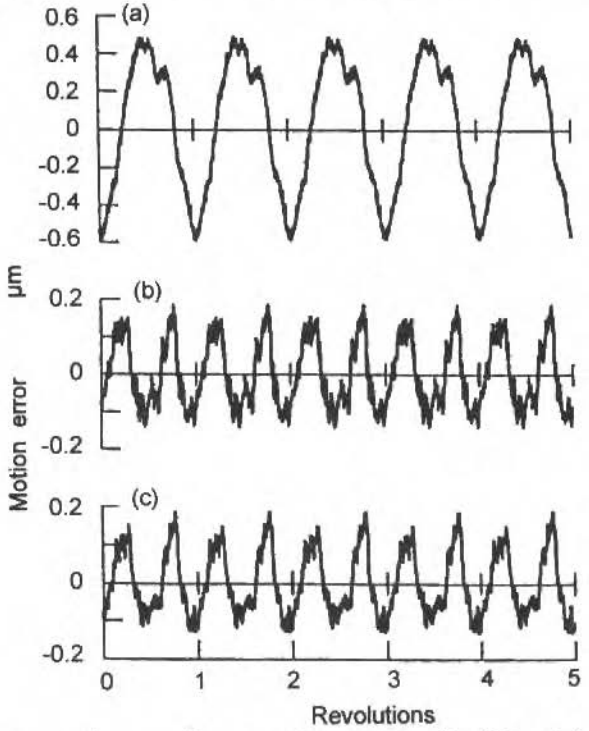

Fig. 18 Absolute rotary motion error without roundness compensation (750 rpm): (a) PAB; (b) AAJB with 2DOF controller; (c) AAJB with 2DOF and repetitive controllers

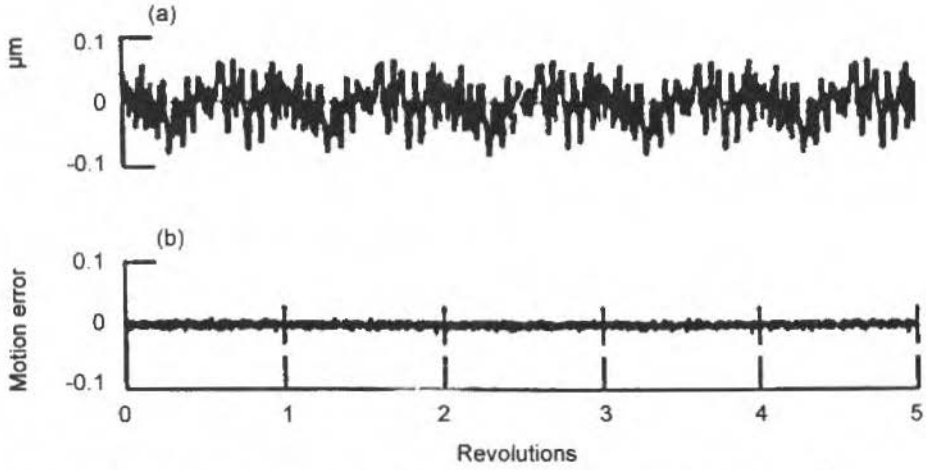

Fig. 19 Absolute rotary motion error with roundness compensation (750 rpm): (a) AAJB with 2DOF controller; (b) AAJB with 2DOF and repetitive controllers.

Conclusions

This paper presented the principle of the "active air journal bearing", AAJB, and by experiments executed in a prototype of the AAJB, it was firstly shown that, when the axis is not rotating the AAJB achieves an almost infinite static stiffness, an increased damping capability and a positioning characteristics with a band-width of 1 kHz. Then, with the axis rotating at 1000 rpm it was shown that the AAJB has the capability of achieving a rotary motion accuracy of 25 nm, positioning its axis quickly and precisely. Finally, by measuring and compensating the profile error of the axis, an absolute rotary motion accuracy of less than 21 nm was achieved with the axis rotating at 750 rpm. The next step of the research is to develop "an active air rotary bearing", AARB, which by using AABs, is capable of controlling five degrees of freedom of a rotating axis, not including the axis rotation. A prototype of the AARB was already constructed and it will be reported in further works.

References

Aoyama, H., Watanabe, I., and Shimokohbe, A., 1987, "Control Mechanism for a High Precision Straight Motion System" IFTOMNProc. 7 th World Congr, Sevilla, Vol. 3 p. 1477

Aoyama, H., Yamaguti, J., Osada, H., and Shimokohbe, A., 1989, "An Ultra Precision Straight Motion Mechanism" Proc. Int. Conf. on Advanced Mechatronics, Tokyo, p. 553

Hara, S., Omata, T., and Nakano, M., 1985, "Synthesis of Repetitive Control System and its Application", Proc. 24th Conf. on Decision and, Control p. 1387

Horikawa, O., and Shimokohbe, A., 1990, "An Active Air Bearing Control of Radial Axis Motion and Stiffness" JSME Int. J., Ser. III, Vol. 33, 55

Horikawa, O., Yasuhara, K., Osada, H., and Shimokohbe, A., 1991, "Dynamic Stiffness Control of Active Air Bearing" Int. J. JSPE, Vol. 25, 45

Shimokohbe, A., Horikawa, O., and Sato, K., 1991, "An Active Air Journal Bearing with Ultraprecision, Infinite Static Stiffness, High Damping Capability and New Functions" Ann. CIRP, Vol. 40, 563

RBCM - J. of the Braz. Soc. Mechanical Sciences
Vol. XVII - nº3 - 1995 - pp. 292-303

ISSN 0100-7386
Printed in Brazil

Previsão das Taxas de Propagação de Trincas de Fadiga Partindo dos Conceitos de Coffin-Manson

Fatigue Crack Growth Rate Prediction Departing from Coffin-Manson Concepts

Jaime Tupiassú Pinho de Castro
Depto. Engenharia Mecânica
Pontifícia Universidade Católica do Rio de Janeiro
R. Marquês de S. Vicente, 225
22453-900 - Rio de Janeiro - R.J. - Brasil

Paulo Pedro Kenedi
StrainLab Análise de Tensões Ltda.
R. Jardim Botânico 700/519
22461-000 - Rio de Janeiro - R.J. - Brasil

Abstract

The Conffin-Manson and the Paris methods, which are normally used in a supplementary but impervious way in the dimensioning against the crack initiation and propagation phases of the fatigue process, are correlated through a series of simple and didactic appealing models. All the proposed models use the classical engineering routines based on cyclic mechanical properties and on the Miner's linear damage accumulation rule. The simpler one uses a singular plastic strain field to estimate the crack growth propagation rate, whereas the more complex recognize the finite dimension of the fatigue crack tip radius, and use various strain concentration rules to quantify the maximum strain amplitude. The models are easy to apply and to phenomenologically justify, and they present a very encouraging correlation with experimental results reported in the literature.
Keywords: Fatigue, Crack Growth Rate, Low-Cicle Fatigue

Resumo

Modelos analíticos de forte apelo didático são desenvolvidos para correlacionar as metodologias de projeto à fadiga de Conffin-Manson e de Paris, normalmente consideradas como incompátiveis. Os modelos são de fácil aplicação e justificativa fenomenológica, e apresentam correlação muito promissora com resultados experimentais relatados na literatura.
Palavras-chave: Fadiga, Taxa de Propagação de Trincas, Fadiga Oligocíclica

Introdução

Neste trabalho desenvolve-se diversos modelos analíticos para correlacionar as duas metodologias modernamente usadas no projeto mecânico à fadiga: o método εN ou de Coffin-Manson (que considera as deformações elastoplásticas e o amolecimento ou o endurecimento cíclico atuantes na raiz de um entalhe, mas não reconhece a presença das trincas de fadiga), e o da/dN ou de Paris (baseado na Mecânica da Fratura e que quantifica a propagação das trincas, mas não pode prever sua iniciação). O objetivo primário do desenvolvimento dos diversos modelos é manter um forte apelo didático e uma clara justificativa fenomenológica, para que a correlação entre as duas metodologias seja facilmente reproduzível e generalizável.

Estes dois métodos de projeto à fadiga têm sido tradicionalmente usados ou de forma alternativa ("projeto à vida segura" ou "projeto tolerante às falhas"), ou quando muito de forma suplementar mas estanque (o εN para prever iniciação e o da/dN para quantificar a propagação das trincas), como se suas filosofias fossem totalmente incompatíveis (ver, por exemplo: Rice, 1988, Suresh, 1991 ou Dowling, 1993).

Os modelos aqui propostos têm por finalidade eliminar esta dicotomia da maneira mais simples e didática possível, usando as propriedades mecânicas cíclicas, a curva de Coffin-Manson o campo das deformações elastopláticas à frente da trinca (descrito pela singularidade de HRR, Hutchinson 1979,

Manuscript received: January 1995. Technical Editor: Agenor de Toledo Fleury

Latzko et al., 1984), as regras de concentração de deformações (Neuber e Linear) e a regra linear de acúmulo de dano para estimar a taxa de propagação das trincas de fadiga, da/dN.

Todos os modelos seguem o procedimento tradicional do projeto mecânico à fadiga: quantificam a deformação atuante num dado elemento de volume e o dano por ela causado, a cada ciclo do carregamento, até acumular o dano crítico que rompe o elemento.

Modelos de Propagação de Trincas

O primeiro modelo empírico mecanicamente bem sucedido para descrever a taxa de propagação de trincas de fadiga foi proposto por Paris et al. no começo da década de 60. Paris mostrou que a taxa da/dN é primeiramente correlacionada com a faixa de variação do fator de intensidade de tensões ΔK:

$$\frac{da}{dN} = A\Delta K^m \qquad \text{(Paris) (1)}$$

onde A e m são constantes dependentes do material, obtidas experimentalmente.

Apesar de muito usada na prática, a regra de Paris só descreve a fase intermediária da curva da/dN vs. ΔK, não considerando nem a existência de um limiar de propagação ΔK_{th} nem a instabilidade das trincas, que ocorre quando o maior valor do fator de intensidade de tensões K_{max} atinge a tenacidade à fratura do material K_c.

Por causa disto, muitas outras regras empíricas foram propostas para se descrever melhor toda a forma sigmoidal da curva da/dN vs. ΔK, bem como os efeitos de algumas variáveis secundárias como a carga média (geralmente quantificada por $R = K_{min}/K_{max}$), e a carga de abertura da trinca K_{op}. Dentre estas regras, provavelmente as mais comuns são:

$$\frac{da}{dN} = A\Delta K^m K_{max}^p \qquad \text{(Walker) (2)}$$

$$\frac{da}{dN} = A\Delta K^m (K_{max} - \Delta K_{th})^p \qquad \text{(Hall) (3)}$$

$$\frac{da}{dN} = \frac{A\Delta K^m}{(1-R)K_c - \Delta K} \qquad \text{(Forman) (4)}$$

$$\frac{da}{dN} = \frac{A\Delta K^m \sqrt{\Delta K - \Delta K_{th}}}{(1-R)K_c - \Delta K} \qquad \text{(Forman modificado) (5)}$$

$$\frac{da}{dN} = A\left[\frac{\Delta K - \Delta K_{th}}{K_c - K_{max}}\right]^m \qquad \text{(Priddle) (6)}$$

$$\frac{da}{dN} = A(\Delta K - K_{op})^m \qquad \text{(Elber) (7)}$$

Todas estas regras requerem a determinação de constante como A e m, que devem ser obtidas experimentalmente em testes de propagação de trincas de fadiga. Há muitas outras regras empíricas similares, cada uma justificada por um determinado conjunto de dados experimentais (para listas mais extensas ver, por exemplo, Hoeppner e Krupp, 1974, Chand e Garg, 1985 ou Schwalbe 1974). Entretanto, nenhuma é fundamentalmente diferente da regra original de Paris. A escolha dentre as diversas regras depende do conjunto particular de dados experimentais que se queira ajustar, sendo que muitas vezes várias delas podem ser usadas de forma igualmente satisfatória, como pode ser visto nos diversos trabalhos das STP 687 (1979) e 748 (1981), que usam o mesmo banco de dados experimentais.

Prever ou estimar a taxa de propagação de trincas de fadiga na ausência de resultados experimentais específicos (isto é, usando apenas as propriedades medidas em outros testes como o de tração, por exemplo), é um problema que tem despertado muito interesse na literatura. Inúmeras regras "preditivas" foram propostas, partindo geralmente ou da abertura da ponta da trinca CTOD, ou da energia dissipada por trabalho plástico, ou então do plano acumulado pelas solicitações cíclicas.

Os modelos preditivos do tipo CTOD assumem que a trinca de fadiga cresce em cada ciclo de quantidade proporcional ao estiramento de sua ponta, quantificado pela sua abertura calculada pelos conceitos básicos da Mecânica da Fratura Linear Elástica, ou seja: $da/dN \sim CTOD \sim K^2/ES_Y$ onde E é o módulo de Young e S_Y a resistência ao escoamento. Os modelos de Pelloux e de Ladner estão entre os pioneiros e podem ser citados como representativos (γ é o coeficiente de Poisson):

$$\frac{da}{dN} = \frac{\Delta K^2}{8\pi E S_Y} \qquad \text{(Pelloux) (8)}$$

$$\frac{da}{dN} = \frac{\Delta K^2 (1-\gamma^2)}{2ES_Y} \qquad \text{(Ladner) (9)}$$

Os modelos do tipo de energia dissipada por trabalho plástico assumem que a totalidade do dano causado pelos carregamentos cíclicos ocorra muito próximo da ponta da trinca, na região de comprimento ZP chamada "zona de processamento", que é a mais solicitada pelas deformações plásticas cíclicas. Assumindo que as amplitudes de tensão, $\sigma_a = \Delta\sigma/2$, e de deformação plástica $\varepsilon_{pa} = \Delta\varepsilon_p/2$, se relacionem por:

$$\sigma_a = K'(\varepsilon_{pa})^{n'} \qquad (10)$$

onde K' é o módulo de plasticidade (ou coeficiente de encruamento) cíclico e n'o expoente de encruamento cíclico, a densidade de energia dissipada por trabalho plástico por ciclo de carregamento, ΔW_p, é dada por:

$$\Delta W_p = \frac{\Delta\sigma\Delta\varepsilon_p}{1+n'} \qquad (11)$$

Separando a equação de Coffin-Manson nas suas partes elástica e plástica, temos:

$$\Delta\sigma = 2\sigma_f'(2N)^b \qquad (12)$$

$$\Delta\varepsilon_p = 2\varepsilon_f'(2N)^c \qquad (13)$$

onde σ_f' e ε_f' são os coeficientes e b e c os expoentes de resistência e de dutilidade à fadiga, e N o número de ciclos aplicado à peça. Usando as expressões desenvolvidas por Kujawasky (1987) para relacionar $\Delta\sigma$ e $\Delta\varepsilon_p$ com o tamanho da zona de processamento ZP, pode-se mostrar que, (Kenedi 1991):

$$\frac{da}{dN} = \left[\frac{(1-2\nu)^2}{2^{b+c+2}(1+n')E\pi\sigma_f'\varepsilon_f' ZP^{b+c+1}}\right]^{\frac{-1}{b+c}} \Delta K^{\frac{-2}{b+c}} \qquad (14)$$

Modelos desse tipo apresentam boa correlação com os resultados experimentais(ver Kujawski e Ellyin, 1987 e 1989 e Glinka, 1985), entretanto precisam de testes de propagação de trincas para ajustar o tamanho da ZP, o que certamente é um contra-senso.

Modelos tipo acúmulo de dano foram desenvolvidos por Majumdar e Morrow (1967) e por Schwalbe (1977). As equações a que eles chegaram são, respectivamente:

$$\frac{da}{dN} = \frac{-2(b+c)}{b+c+1}\left(\frac{S'_Y}{4(1+n')\sigma'_f\varepsilon'_f}\right)^{\frac{-1}{b+c}} \times \left[1-(4(1+n')\varepsilon_Y)^{\frac{-(b+c+1)}{b+c}}\right]\frac{\varepsilon'_Y\Delta K^2}{\pi S'^2_Y} \qquad \text{(Morrow) (15)}$$

$$\frac{da}{dN} = \frac{(1-2\nu)^2}{4\pi(1+n')S'_Y}\left(\frac{2S'_Y}{E\varepsilon'_f}\right)^{(1+n')}\left[(\Delta K-\Delta K_{th})^2\left(\frac{K_c}{K_c-K_{max}}\right)\right] \qquad \text{(Schwalbe) (16)}$$

onde S'_Y e ε'_Y são a resistência ao e a deformação de escoamento cíclicas.

Modelo Básico de Acúmulo de Dano

O fundamento da modelagem aqui proposta é simples e direto: assume-se que as trincas de fadiga se propagam pela quebra seqüencial de pequenos elementos de volume de largura da, um a cada ciclo N, como mostrado na Fig. 1 (Kenedi e Castro, 1992). Cada um destes elementos é tratado como se fosse um corpo de prova (CP) do tipo ε N, submetido a deformações cíclicas crescentes à medida que a ponta da trinca dele se aproxima, como esquematizado na Fig. 2. Cada CP rompe quando a trinca o atinge, e neste caso pode-se afirmar que ele rompeu porque acumulou o dano crítico que poderia tolerar.

Para quantificar-se o dano acumulado em cada CP, assume-se que: (i) são relevantes apenas as deformações plásticas (cíclicas) atuantes dentro da zona plastificada reversa cujo comprimento é R_{YR}; (ii) como o carregamento é mantido constante, a trinca de fadiga avança por incrementos iguais em cada ciclo (o que é bem razoável, devido à pequena dimensão física de R_{YR}), e (iii) o material seja elasto-plástico, contínuo, isotrópico e homogêneo. Portanto:

$$x_i = R_{YR} - n_i\frac{da}{dN} \qquad (17)$$

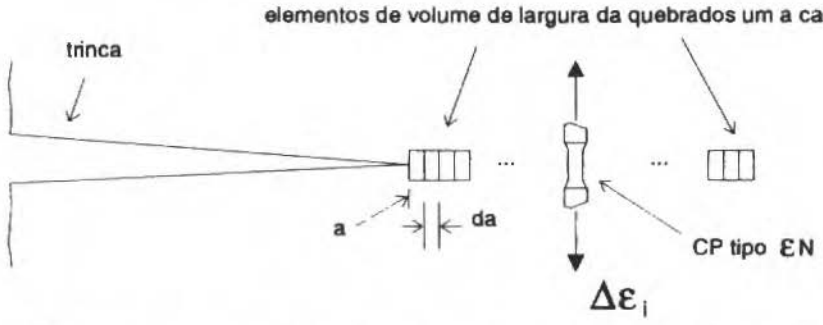

Fig. 1 Crescimento da trinca causada pela quebra seqüencial de Corpos de Prova tipo εN

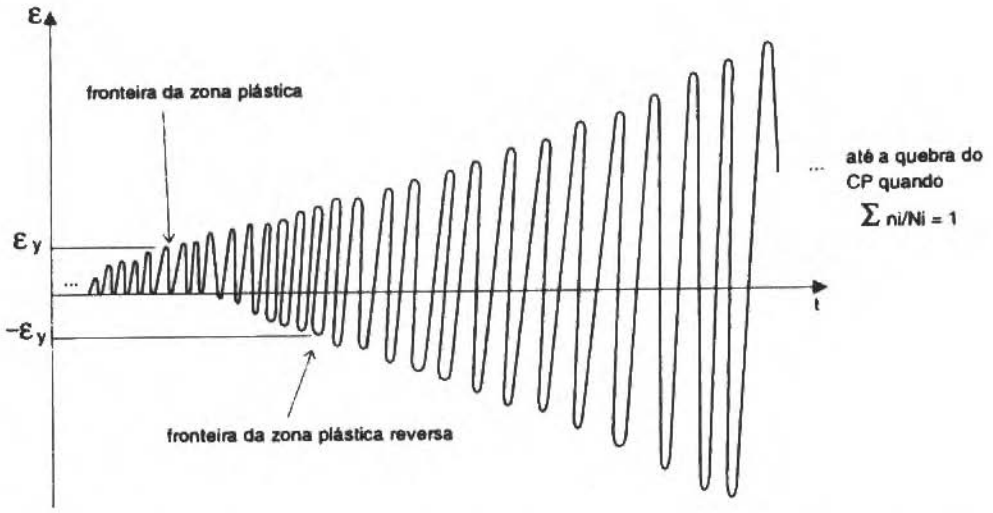

Fig. 2 História esquemática das deformações atuantes em cada um dos CPs

onde n_i é o número de ciclos necessários para que a ponta da trinca percorra a distância x_i,Fig. 3. Usando a modificação proposta por Schawalbe (1977) no campo de deformações de HRR, para se quantificar a amplitude das deformações cíclicas $\Delta\varepsilon_{pi}/2$ atuantes num dado CP distando x_i da ponta da trinca, obtém-se:

$$\frac{\Delta\varepsilon_{pi}}{2} = \frac{S'_Y}{E}\left(\frac{R_{YR}}{x_i}\right)^{\frac{1}{1+n'}} = \frac{S'_Y}{E}\left[\frac{(1-2\nu)^2\Delta K^2}{4\pi(1+n')S_Y^2}\cdot\frac{1}{x_i}\right]^{\frac{1}{1+n'}} \qquad (18)$$

De regra de Coffin-Manson pode-se obter o número de ciclos que o CP duraria caso fosse submetido apenas a esta amplitude de deformações:

$$N_i = \frac{1}{2}\left(\frac{\Delta\varepsilon_{pi}}{2\varepsilon'_f}\right) = \frac{1}{2}\left[\frac{S'_Y}{E\varepsilon'_f}\left(\frac{R_{YR}}{R_{YR}-n_i\frac{da}{dN}}\right)^{\frac{1}{1+n'}}\right]^{\frac{1}{c}} \qquad (19)$$

Mas, como a amplitude das deformações atuantes no CP cresce à medida que a ponta da trinca dele se aproxima a cada ciclo, é preciso usar uma regra de acúmulo de dano para quantificar o efeito dos carregamentos variáveis. Escolhendo (por simplicidade) a regra linear de Palmgren-Miner para quantificar o dano acumulado, pode-se obter implicitamente a expressão básica desta modelagem para prever a taxa de propagação das trincas de fadiga a partir dos conceitos do método εN (note-se que $\Delta\varepsilon_{pi}$ só atua durante um ciclo):

$$\sum\frac{n_i}{N_i} = \sum_{i=1}^{i_f} 2\left[\frac{S'_Y}{E\varepsilon'_f}\left(\frac{R_{YR}}{R_{YR}-n_i\frac{da}{dN}}\right)^{\frac{1}{1+n'}}\right]^{-\frac{1}{c}} = 1 \qquad (20)$$

onde i_f= int(R_{YR}/da/dN) será numericamente igual ao número de ciclos necessários para romper cada elemento de volume.

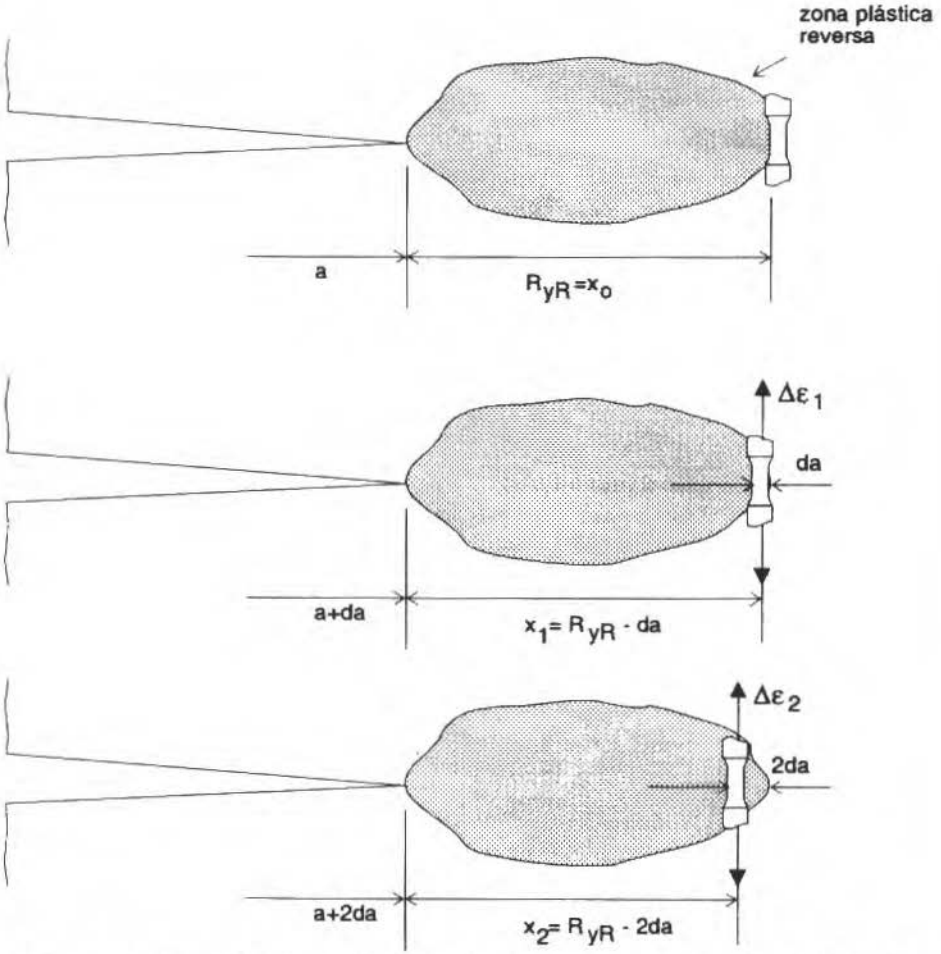

Fig. 3 Esquema do avanço da trinca e das solicitações em cada CP, à medida que a ponta da trinca dele se aproxima

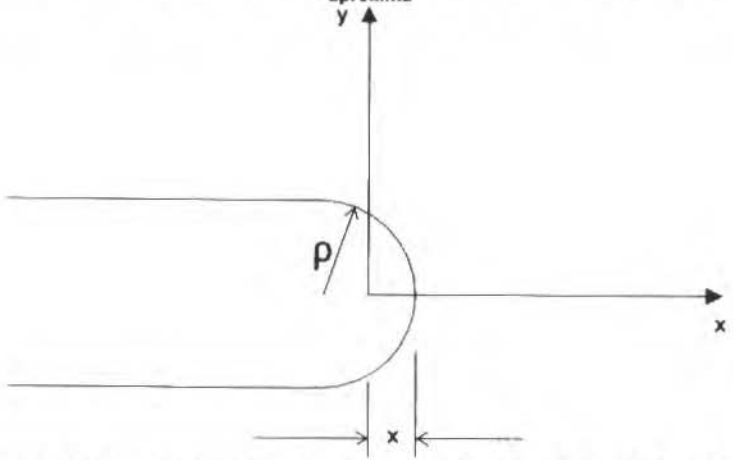

Fig. 4 Translado da origem do eixo de coordenadas da ponta para uma distância x dentro da trinca. Para Creager x = ρ /2

Retirando-se o último ciclo do somatório, para evitar a singularidade das deformações na ponta da trinca, e explicitando-se ΔK, obtém-se uma fórmula (conceitualmente) simples para estimar as taxas de fadiga a partir das propriedades cíclicas do material:

$$\frac{da}{dN} = \left(\frac{2^{-c}S'_Y}{\varepsilon'_f E}\right)^{1+n'} \frac{(1-2\nu)^2}{4\pi(1+n')S_Y^{-2}} \left[\sum_{i=1}^{i_f-1}\left(\frac{1}{i}\right)^{\frac{-1}{c(1+n')}}\right]^{-c(1+n')} \Delta K^2 \qquad (21)$$

Deve-se enfatizar que esta equação reproduz a regra de Paris baseada apenas nas hipóteses tradicionais do dimensionamento mecânico à fadiga pelo método ε N. Logo, ela correlaciona de forma clara e inequívoca estes dois métodos modernos de projeto que têm sido tratados de forma estanque. Entretanto, (21), prevê que da/dN seja função de ΔK^2 para todos os materiais, já que o tamanho da zona plástica reversa R_{YR} é uma função quadrática de ΔK. Esta previsão não é confirmada na prática, logo é necessário melhorar o Modelo Básico expresso em (21).

Aperfeiçoamento no Modelo Básico

Primeiramente deve-se notar que a escolha arbitrária da fronteira elastoplástica reversa para iniciar o acúmulo de dano não altera o valor do expoente de ΔK, só influindo na constante A da regra de Paris. Isto porque as deformações cíclicas à frente da ponta da trinca permanecem descritas por (18), enquanto que o ponto de início da contagem de dano só influi em i_f, o limite superior do somatório de Miner.

A segunda limitação do Modelo Básico é não reconhecer que trincas reais têm pontas com raio ρ e não zero. Como não se conhece solução exata para descrever trincas reais, para modelá-las usar-se-á uma abordagem originalmente proposta por Creager e Paris (1967) transladando-se a origem do eixo de coordenadas para dentro da trinca de uma distância X, como mostrado na Fig. 4.

Creager localizou esta origem em $X = \rho/2$ para resolver o problema linear elástico, visando usar as soluções de K_I disponíveis para resolver problemas de concentração de tensões em entalhes profundos. A tensão (linear elástica) σ_y neste caso é dada por:

$$\sigma_y = \frac{K_I}{\sqrt{2\pi r}}\left[\cos\frac{\theta}{2}\left(1+\sin\frac{3\theta}{2}\right)+\frac{\rho}{2r}\cos\frac{3\theta}{2}\right] \qquad (22)$$

onde θ e r são as coordenadas polares do ponto em questão. Na raiz do entalhe e no plano da trinca temos $r = \rho/2$ e $\theta = 0$ e, segundo Creager, $\sigma_y = 2K_I/(\pi\rho)^{1/2}$

Seguindo a mesma idéia, X pode ser estimado calculando-se $\Delta\varepsilon_{ppt}$ por uma das regras de concentração das deformações elastoplástica cíclicas (como a de Neuber ou a Linear, Fuchs e Stephens, 1980, ou a de Gemma, 1985), tendo a trinca o fator de concentração de tensões (linear elástico ou geométrico) K_t obtido ou de Creager, ou da clássica solução de Inglis $K_t = 1+2\,(a/\rho)^{1/2}$, onde a é o comprimento da trinca. Na ponta da trinca (que agora é modelado de forma mais realista, com raio ρ e não zero) a amplitude de deformações $\Delta\varepsilon_{ppt}/2$ é finita, e de (18) X vale:

$$X = R_{YR}\left(\frac{\Delta\varepsilon_{ppt}E}{2S'_Y}\right)^{-(1+n')} \qquad (23)$$

$\Delta\varepsilon_{ppt}$ pode ser calculado a partir das tensões nominais atuantes na peça, $\Delta\sigma_{nom}$, usando-se uma das regras de concentração de deformações. Por exemplo, com a regra Linear:

$$\frac{\Delta\varepsilon_{ppt}}{2} = K_t \frac{\Delta\sigma_{nom}}{2E} \tag{24}$$

Uma estimativa para o valor de $K_t\Delta\sigma_{nom}$ pode ser obtida usando-se a expressão de Creager para calcular as tensões que atuariam em $r = X$ e $\theta = 0$ se o material não escoasse, e lembrando que ρ=CTOD/2:

$$K_t\Delta\sigma_{nom} = \frac{\Delta K}{\sqrt{2\pi X}}\left(1 + \frac{\Delta K^2}{4ES'_Y X}\right) \tag{25}$$

A expressão que se obtém usando a regra de Neuber é um pouco mais complicada algebricamente, mas é similar conceitualmente. Logo, a equação de acúmulo de dano, já sem o problema da singularidade do último ciclo, pode ser escrita como:

$$\sum_{i=1}^{i_f} 2\left[\frac{S'_Y}{E\varepsilon'_f}\left(\frac{R_{YR}}{X + R_{YR} - i\frac{da}{dN}}\right)^{\frac{1}{1+n'}}\right]^{-\frac{1}{c}} = 1 \tag{26}$$

Note-se que se está de novo assumindo a fronteira elastoplástica reversa para inicio do acúmulo de dano por fadiga, o que pode ser facilmente modificado fazendo-se o segundo denominador em (26) X+B-i da/dN (em vez de $X + R_{YR}$-i da/dN), sendo B o ponto em que se deseje começar a contagem do dano. As várias regras de concentração de deformações servem só para alterar X como também o valor de $\Delta\varepsilon_{ppt}$.

Entretanto, as várias equações do tipo (26) que podem ser obtidas (Creager, Linear, Neuber, etç), novamente só alteram o valor do termo constante em (21), mantendo da/dN sempre função de ΔK^2. Para modificar o valor do expoente de Paris, é necessário introduzir uma variação no modelo proposto a qual, se por um lado de certa forma diminui-lhe a auto-consistência, por outro apresenta um sucesso prático bastante encorajador.

Seguindo a idéia originalmente proposta por Schwalbe (1977) inspirada pelas formulações empíricas que reproduzem a forma sigmoidal das curvas da/dN vs. ΔK experimentais, introduz-se em (21) a influência de ΔK_{th}, de K_c e da carga média na taxa de fadiga:

$$\frac{da}{dN} = A\,(\Delta K - \Delta K_{th})^2\left[\frac{K_c}{K_c - K_{max}}\right] \tag{27}$$

A constante A é calculada como em (21) para o modelo da trinca matemática (com $\rho = 0$). Já para modelos não-singulares discutidas acima, não é possível obter-se uma expressão com A explicitado, sendo mais conveniente resolver numericamente (26) para substituir o valor calculado de A em (27). Desta forma foram gerados diversos modelos, que serão chamados de Básico Modificado (pelo artifício de Schawlbe), Creager, linear e Neuber.

Avaliação dos Diversos Modelos

É bastante difícil conseguir na literatura as propriedades mecânicas cíclicas e de propagação de trincas de um mesmo material . A Tabela 1 apresenta uma lista destas propriedades para 4 aços diferentes, baseadas em dados obtidos de diversas fontes, da maneira mais confiável possível, como detalhadamente discutido por Kenedi (199)1.

Tabela 1

Aço	E (GPa)	S'y (MPa)	K' (MPa)	n'	ε_f'	c	ΔK_{th} (MPam$^{1/2}$)	K_{IC} (MPam$^{1/2}$)
A533B	200	345	1048	0,17	0,32	-0,52	9,2	153
4340	209	724	1760	0,15	0,83	-0,65	9,4	116
C-Mn	208	372	1134	0,14	0,15	-0,52	13,0	83
8620	200	679	1954	0,20	0,92	-0,69	9,9	73

K' é a constante da lei parabólica de encruamento ciclico, e ΔK_{th} é listado para R = 0.

As Figs. 5 a 8 mostram as taxas experimentais de propagação de trincas de fadiga dos 4 aços, bem como as curvas previstas por 5 modelos diferentes: o Básico Modificado (27), os baseados nas regras Linear, Neuber e Creager, e um modelo proposto por Schwalbe (16), para efeito de comparação.

Nota-se que em todos casos a forma dos dados experimentais é reproduzida de forma bastante satisfatória, e que a magnitude das previsões está dentro de uma ordem de grandeza dos valores dos testes. Este é um resultado encorajador, pois indica que o caminho seguido na modelagem proposta, apesar de sua grande simplicidade, é capaz de estimar adequadamente o comportamento físico das trincas de fadiga.

A partir somente dos resultados apresentados nas Figs. 5-8, não é ainda possível concluir qual dos modelos propostos é o mais preciso, já que as diversas estimativas não mantém a mesma posição relativa nos 4 materiais analisados. Entretanto, como os dados experimentais não procedem todos da mesma fonte, eles têm que ser encarados como representativos, e não como padrão de referência para calibração dos diversos modelos (o que, é claro, só pode ser obtido a partir de um programa experimental onde os resultados sejam absolutamente confiáveis).

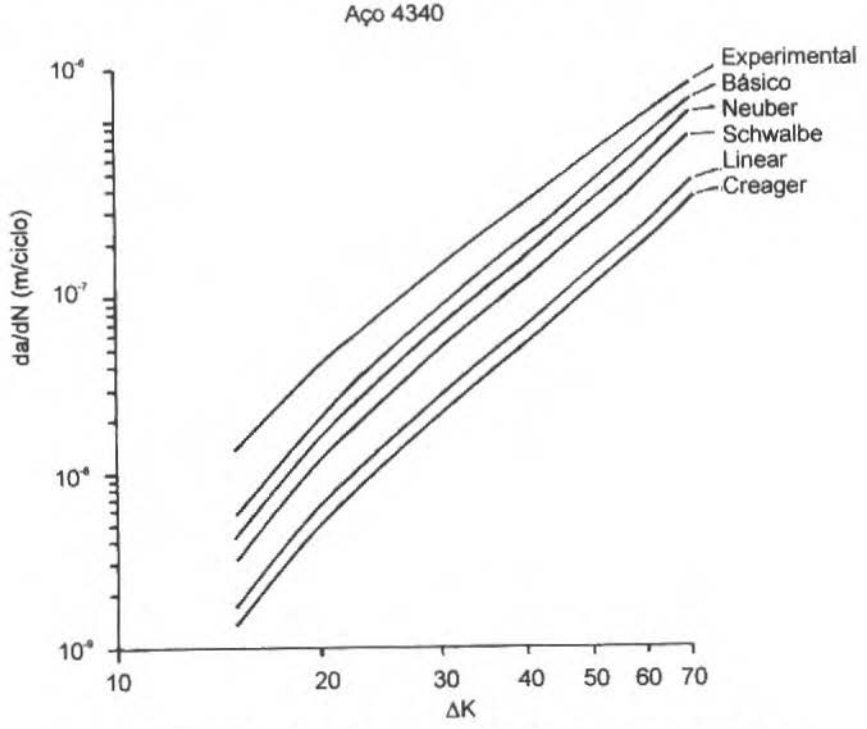

Fig. 5 Taxas Experimentais de Propagação de Trincas de Fadiga-Aço 4340

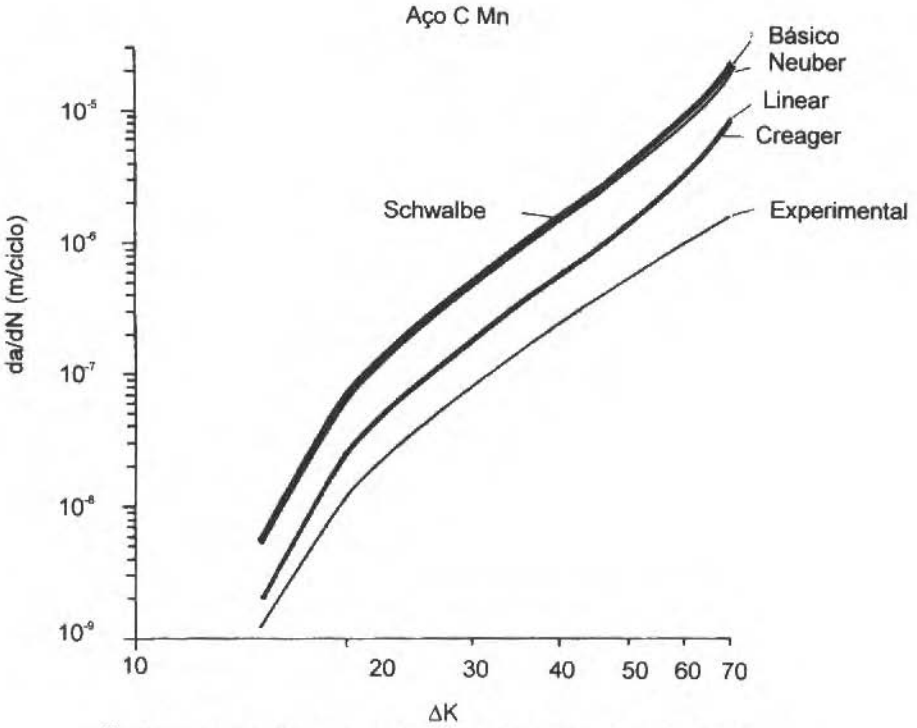

Fig. 6 Taxas Experimentais de Propagação de Trincas de Fadiga-Aço C Mn

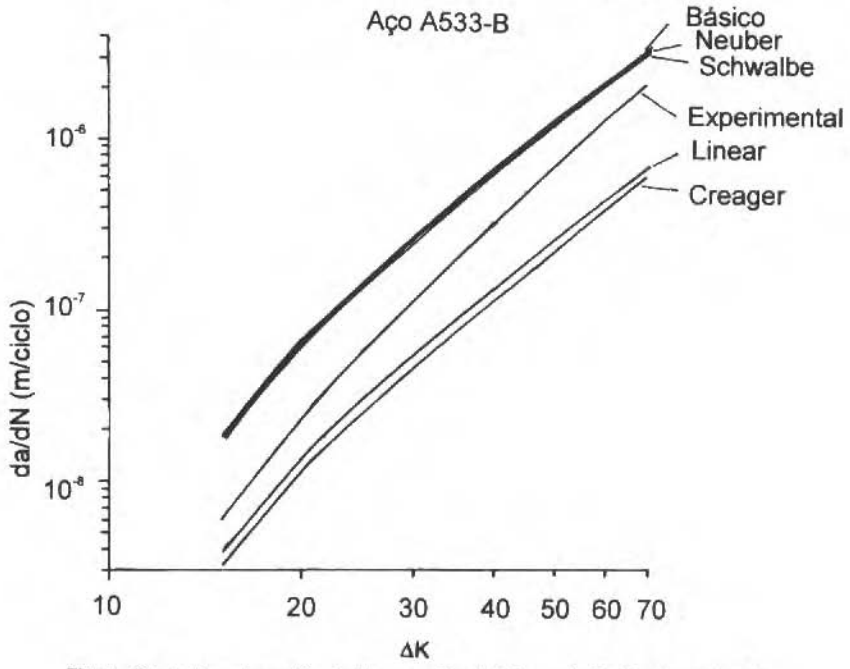

Fig. 7 Taxas Experimentais de Propagação de Trincas de Fadiga-Aço A533-B

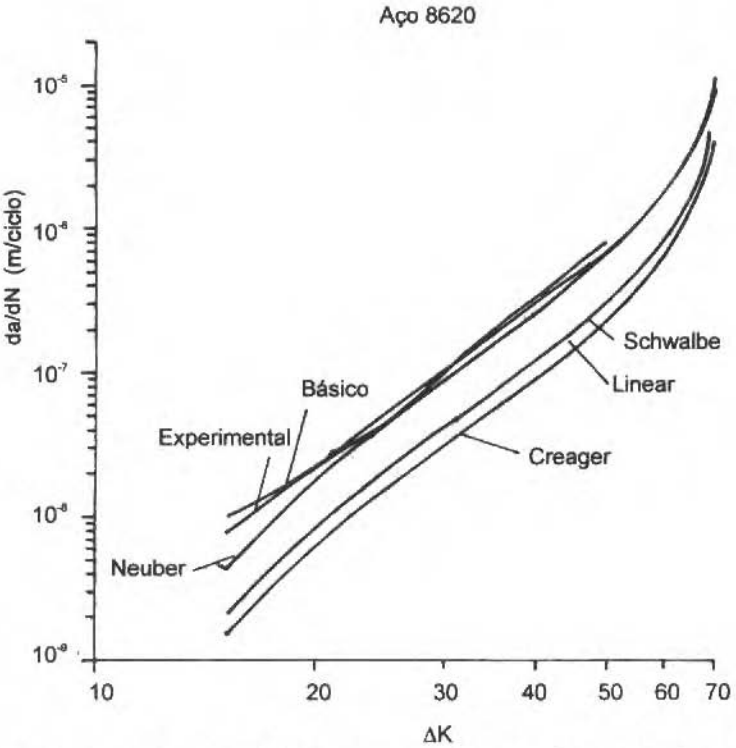

Fig. 8 Taxas Experimentais de Propagação de Trincas de Fadiga-Aço 8620

Um programa experimental que atende a estes requisitos está em andamento; e seus resultados serão publicados brevemente.

Conclusões

Uma modelagem simples, de grande apelo didático, baseada apenas em conceitos tradicionais de projeto mecânico à fadiga pelo método εN, e em correções para considerar os efeitos do limiar, carga média e tenacidade, foi capaz de descrever adequadamente a propagação das trincas de fadiga nos diversos materiais analisados.

Referências

Chand, S., e Garg, S. B. L., 1985, "Crack Propagation Under Constant Amplitude Loading", Eng. Fract. Mech., 21, pp. 1-30.

Creager, M., e Paris, P. C., 1967, "Elastic Field Equations for Blunt Cracks with Reference to Stress Corrosion Cracking", Int. J. Fract. Mech., 3, pp. 247-252.

Dowling, N. E., 1993, Mechanical Behavior of Materials, Prentice Hall

Ellyin, F., e Kujawsky, D., 1989, " Generalization of Notch Analysis and its Extension to Cyclic Loading', Eng. Fract. Meach., 32, pp. 819-826.

Gemma, A. E., 1985, "An Approximate Elastoplastic Anlysis of the Effect of Plane Strain at the Surface of a Notch", Eng. Fract. Mech., 21, pp. 495-501.

Glinka, G., 1985, "Energy Density Approach to Calculation of Inelastic Strain-Stress near Notches and Cracks", Eng. Fract. Mech., 22, pp. 485-508.

Hoeppner, D. W. e Krupp, W. E., 1974," Prediction of Component Life by Application of Fatigue Crack Growth Knowledge", Eng. Fract. Mech., 6, pp. 47-70.
Hutchinson, J. W., 1979, "Nonlinear Fracture Mechanics", Tec. U. Denmark.
Kenedi, P. P., 1991, "Estimativa da Taxa de Propagação de Trincas de Fadiga a Partir de Propriedades Mecânicas Cíclicas", Tese de Mestrado, Dept. Eng. Mecânica, PUC/RJ
Kenedi, P. P., e Castro J. T. P., 1992, "Avaliação de Taxas de Fadiga pelo Método εN, Anais do VII SIBRAT, pp. 269-278, ABCM
Kujawsky, D., e Ellyin, F., 1987, "A Fatigue Crack Growth Model With Load Ratio Effects", Eng. Fract. Mech., 28 pp. 367-378.
Latzko, D. G. H. et al., 1984, Post-Yield Fracture Mechanics, 2nd ed., Elsevier.
Majundar, S., e Morrow, J. D., 1967, "Correlation Between Fatigue Crack propagation and Low Cycle Fatigue Properties", T. & A.M. report 364 U. Illinois.
Rice, R. C., 1988, Fatigue Design Handbook, 2nd ed., SAE.
Schawlbe, K. H., 1974, Comparison of Several Fatigue Crack Propagation Laws with Experimental Results", Eng. Fract. Mech. 67, pp. 325-341
Schawlbe, K. H., 1977, "Some Aspects of Crack Propagation Under Monotonic and Cyclic Load", Eng. Fract. Mech., 9 pp. 547-556.
STP 687, Chang J. B. ed., 1979., "Part-Through Crack Fatigue Life Prediction", ASTM.
STP 748, Chang J. B., and Hudson, C. M. ed. 1981 "Methods and Models for Predicting Fatigue Crack Growth Under Random Loading", ASTM.
Suresh, S., 1991, Fatigue of Materials, Cambridge.

RBCM - J. of the Braz. Soc. Mechanical Sciences
Vol. XVII - nº3 - 1995 - pp. 304-313

ISSN 0100-7386
Printed in Brazil

Reducing the Plunge Cylindrical Grinding Time Using Acoustic Emission Monitoring

E. D. Baldo
Anselmo Eduardo Diniz
State University of Campinas
Campinas, SP, Brazil
CP 6122, CEP 13083-970

Abstract

The spark out stage is responsible usually for up to one third of the time spent in a plunge grinding cycle. Some authors have proposed the implementation of an accelerated spark out stage, in which the wheel position passes the final diameter of the part and returns quickly. This technique, up to now, has been difficult to implement since the feedback parameters have not been clearly defined. This paper attempts to investigate the accelerated sparkout method and examine the effect on part quality. Acoustic emission, generated by the grinding process, is shown to be a very good way to establish the parameters necessary to implement the accelerated spark out stage. It is also shown in this work that this kind of cycle does not damage the part.
Keywords: Grinding, Monitoring, Acoustic Emission

Introduction

Monitoring of machining process using acoustic emission (AE) has been extensively studied in the last 15 years and has shown good results not only in universities, but also in industry (Kakino, 1984). The method has many advantages when compared with other means of monitoring such as measuring the cutting forces with piezoelectric dynamometers or the power consumed by electrical motors. Some of these characteristics are:

- The sensor is simple, cheap and small;
- The acoustic emission sources are directly related with the cutting process, and
- Noises coming from the environment, like mechanical vibrations of the machine, do not influence the AE signal, since the interesting signals are generated at much higher frequencies than the background noises (50 KHz to 1 MHz).

AE can be defined (Blum, 1988; Kannatey-Asibu and Dornfeld, 1981) as acoustic waves generated by a material when subject to an external stimulus. In other words, when a material is deformed, waves of elastic tension propagate inside it due to the quick release of the deformation energy, causing an acoustic emission. These tension waves cause very small displacements on the surface of the material, which can be captured by a piezoelectric sensor that transforms the displacements into an electrical signal. The frequency band of this signal is usually from 50 KHz to 1 MHz.

Many additional phenomena, occurring in the cutting process, generate AE, such as the shear and plastic deformation in the primary cutting zone, the friction between chip and tool and between tool and workpiece, the breakage of the chip (Blum, 1988) and, in the case of grinding, the impacts of each grain on the workpiece surface. Because of this, AE has been used to accomplish many goals in the machining process like on-line monitoring of tool wear and detecting tool fracture in both, milling (Kakino, 1984; Blum and Inasaki, 1990) and turning process (Lan and Dornfeld, 1984; Kannatery-Asibu and Dornfeld, 1982). It has also been used in diamond turning in order to monitor the actual depth of cut (Liu, 1991).

Monitoring the Grinding Process Through Acoustic Emission

As already cited before, acoustic emission has been used to monitor some metal cutting processes, like turning and milling. In these kind of processes, the sources of acoustic emission generation are well known, since the process is relatively deterministic, because the tool has only one or few cutting edges. In the grinding process, however, the tool is composed by thousands (or millions) of abrasive

Manuscript received: March 1995. Technical Editor: Walter L. Weingaertner

grains that have irregular geometry and are randomly distributed through out the wheel. There are, however, some similarities between the AE generated in grinding and the AE generated in either turning or milling.

The main sources of AE in a grinding operation are:

- Sliding of the abrasive grain on the surface of the part, in the first contact grain-part;
- Ploughing of the surface part, without material removal, a short time after the first contact, and
- Chip removal.

Dornfeld and Cai (1984) studied the use of AE to reduce the non-productive delay that occurs between the moment that the wheel infeed speed, used during grinding, is turned on and the moment the wheel touches the part. This technique was after referred to as gap elimination. The results are shown on Fig. 1. When the distance between wheel and part is bigger than 25.4 μm, only the instrumentation noise is detected. When this distance gets the range between 7.6 and 25.4 μm, there is an interaction between part and cutting fluid and between cutting fluid and wheel, that generates a measurable AE signal. When the gap is smaller than 7.6 μm there is already some interaction between part and wheel leading to a strong AE signal. Dornfeld and Cai also monitored the spark out stage using AE in surface grinding. They proved that, initially, AErms decreases as the number of wheel reciprocations increases during the spark out stage, followed by a second stage when the signal stabilizes. When this happens, no more material is being removed and the spark out is finished. This result proves that it is possible, using acoustic emission, to determine exactly the number of strokes needed for a complete spark out.

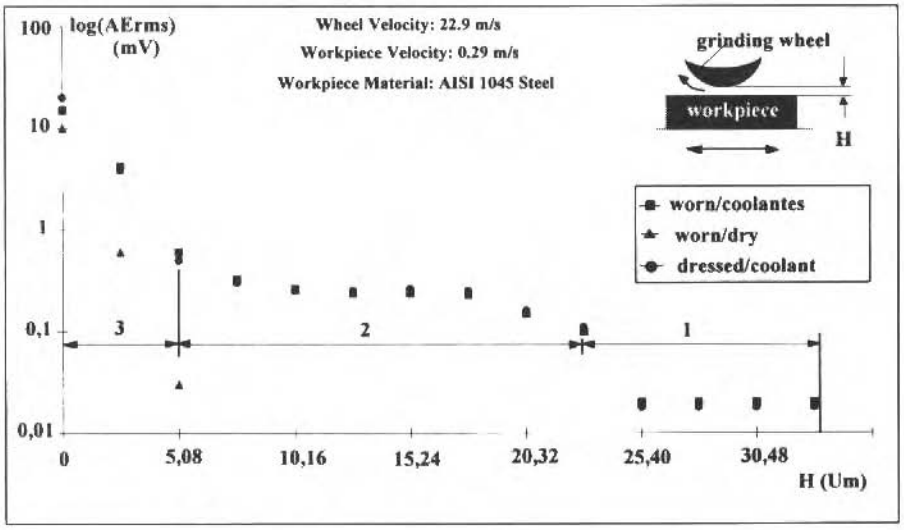

Fig. 1 Values of Acoustic Emission for Different Wheel-Part Distance

Nomenclature

a_d = dressing depth [μm]
AErms = root mean square of the acoustic emission signal [V or mV]
b_d = width of the dresser [mm]
H = gap between wheel and workpiece [μm]
n_w = workpiece rotation [rpm]
Rmax = maximum surface roughness [μ m]
r(t) = radial position of the wheel [mm]
s_d = dressing feed [mm/rev]
t_1 = rough grinding time [s]
t_2 = sparkout time [s]
t_f = whole grinding cycle time [s]
u_1 = radial infeed velocity [mm/s]
u_m = retraction velocity of the wheel in the accelerated sparkout cycle [mm/s]
Δr_i = radial wheel positions during the grinding cycle [mm]
ε = amount of material not removed by the sparkout [μm]
τ = delay to elastic deformation of the wheel-workpiece-machine system [s]

Inasaki and Okamura (1985) concluded that AE is a very good way to monitor both the dressing and grinding process. The wheel life, in many cases, can also be evaluated by AE since the signal increases as the wheel loses its sharpness. In dressing, they concluded that, when the shape of the wheel is irregular (worn wheel) and the dressing depth is not constant (and so more strokes of the dresser are necessary) the AE signal is also not constant. When the AE signal becomes constant, it is time to stop the dressing process, because a constant dressing depth was reached and the wheel has the correct geometry.

Eda et al. (1985) verified the correlation between the number of thermal cracks and the AE signal generated during the grinding process. They saw that, when spiky AE signal occurs just after the wheel passes over the work surface, a substantial amount of cracks are found on the ground surface. Eda et al. (1984) demonstrated that there is a relationship between the color of the ground surface that was burnt by the wheel and some components of the AE frequency spectrum. Moreover, the AE signal level increases when the part is burnt.

Plunge Grinding Cycle

Figure 2 shows the position of the wheel against cutting time during a whole cycle of plunge cylindrical grinding. It can be seen in this figure that, at the beginning of the cut, the actual infeed of the wheel is delayed due to the elastic deformation of the workpiece and wheel. After some time, the actual infeed rate becomes equal to the controled infeed rate (u1), followed by a period with infeed rate equal to zero, that has the purpose of removing all the material that is still in the workpiece due to the elastic deformation. This period is called spark out.

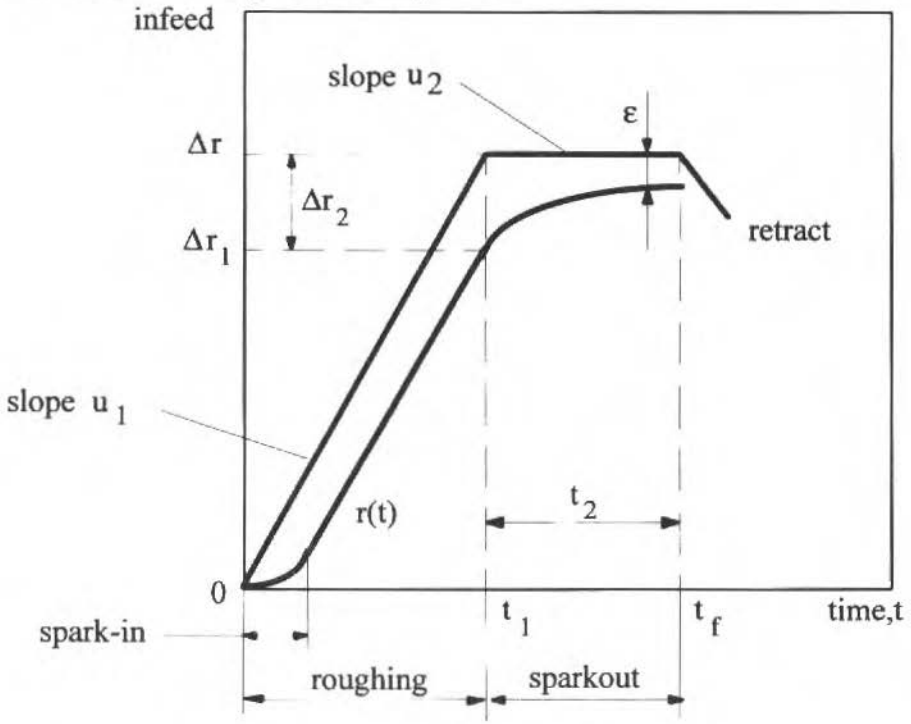

Fig. 2 Conventional Grinding Cycle, Malkin (1989)

The delay to elastic deformation (τ) depends on the stiffness of the wheel-work-machine system. Its value is usually in the range of 0.5 to 1.0 s in external plunge grinding (around 5% of the whole cycle) and from 1 to 10 s in internal grinding. The spark out time occupies around 30% of the total grinding cycle time.

One way to reduce the spark out time and the time for the whole grinding cycle is to use the cycle shown on Fig. 3, proposed by Malkin (1989). In this cycle the wheel overshoots the final dimension of the workpiece by Δr_3 with the infeed speed u_1. Then, the wheel is retracted to achieve the final dimension of the workpiece, using the speed u_m. After this, the wheel must stay for a short time ($1/n_w$ - where n_w is the part revolution) stopped in this dimension, in order to complete the spark out around all the perimeter of the part.

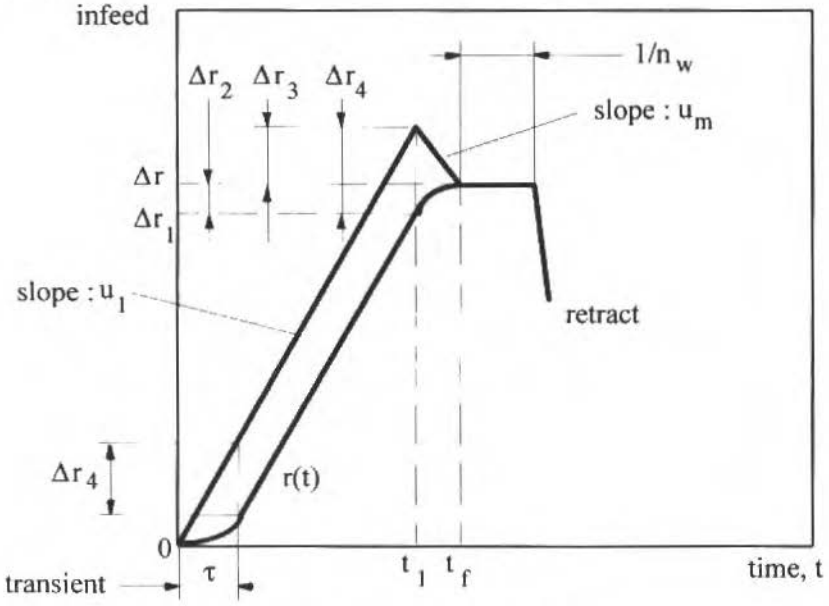

Fig. 3 Accelerated Plunge Grinding Cycle, Malkin (1989)

To implement this cycle it is necessary to get the correct value of Δr_3 and u_m to avoid the dimension to exceed its range of tolerance. The performance of this cycle depends on the estimation of Δr_2 . Once Δr_2 is obtained, um can be calculated using Eq. (1). The calculation of Δr_2 is difficult, although Malkin showed that $(\Delta r_2/u_1\tau)$ is between 0.2 and 0.8. Therefore, assuming a value of $(\Delta r_2/u_1\tau)$ inside the proposed interval, the determination of Δr_2 depends just on the determination of τ and using Eq. (1), u_m can be determined as follows :

$$u_m = -u_1 \cdot e^{\left(1.65 - 5.15\frac{\Delta r_2}{u_1\tau}\right)} \qquad (1)$$

In this work, the value of $(\Delta r_2/u_1\tau)$ used was 0.3 since this value is inside the interval proposed by Malkin and makes $u_m = u_1$ in Eq. (1). With Δr_2, the value of Δr_3 (the overshoot) can be calculated by the following equations [15]:

$$\Delta r_3 = \Delta r_4 - \Delta r_2 \qquad (2)$$

$$\Delta r_4 = u_1\tau - \frac{u_1\tau}{e} = u_1\tau\left(1 - \frac{1}{e}\right) \qquad (3)$$

As shown, just the value of τ is missing in order to implement the accelerated cycle. This work has the purpose of verifying the feasibility of using the acoustic emission generated by the process, to obtain τ (and so to get the values of u_m and Δr_3) and also to check if the use of the accelerated cycle does not harm the quality of the part.

Materials, Equipments and Experimental Procedures

The experiments were divided in two phases. In the first one the purpose was to verify whether the use of acoustic emission is a good way to obtain the time spent by the system wheel-part in elastic deformation (τ) and, in the second one, the purpose was to implement the accelerated plunge grinding cycle with the help of acoustic emission and to check whether the quality of the part (roundness and surface roughness) is not damaged by this kind of cycle.

Metodology of the Experiments to Check the Feasibility of using AE to Obtain τ

This phase of the experiments consisted of plunge cylindrical grinding operations of quenched 4340 steel with 52 Rc of hardness, using several values of infeed speed (u_i). During all the experiments the acoustic emission generated in the process was measured. The AE sensor was attached to the tailstock of the machine tool. The grinding machine used was a conventional one (non CNC). The cutting conditions used were:

- Radial Infeed Speed: 0.012, 0.018, 0.020, 0.024, 0.040 and 0.060 mm/s
- Revolution of the Part: 120 RPM
- Part diameter : 50 mm
- Workpiece Velocity: 0.31 m/s
- Revolution of the Wheel: 2000 RPM
- Wheel Velocity: 36 m/s
- Infeed per Part Revolution = 0.02 mm
- Theoretical Material Removal Rate: 6.28 $mm^3/mm.s$
- Wheel Specification: D-A-46-K-5-V-10W (ϕ350 x 19 mm)
- Tool for Dressing: Single-point Diamond
- Dressing conditions:
  - Dressing Depth: 30 μm
  - Width of the Dresser: 0.65 mm
  - Dressing Feed: 0.13 μm/revolution

The Experimental Setup is shown on Fig. 4. The time constant, used in the RMS voltmeter, was 2 ms and the gain of the amplifier was 40 dB.

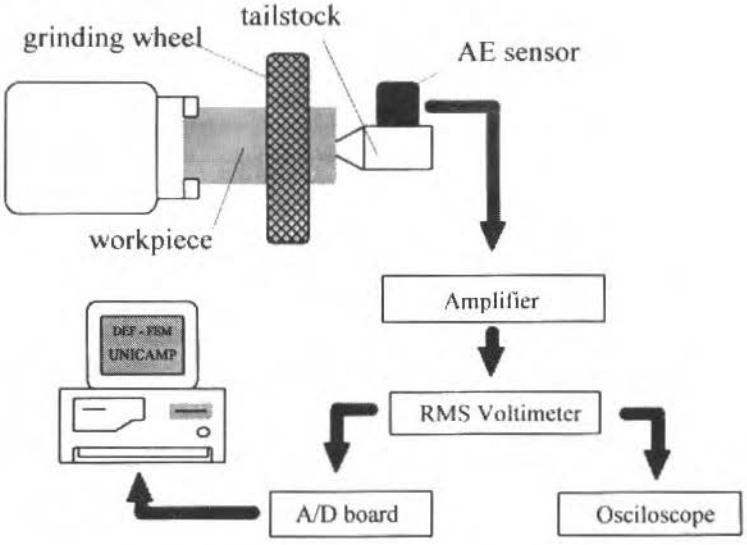

Fig. 4 Experimental Setup

Metodology of the Experiments Aiming to Verify the Quality of the Part in Accelerated Spark out Cycle

In this second phase, all the experiments consisted of plunge grinding cylindrical parts of 4340 steel with a hardness of 52 Rc, using a CNC machine, which is well suited to implement the accelerated spark out. At first, the parts were machined using the conventional spark out cycle. In this kind of experiments 5 different values of infeed rate were used. After each cycle, the wheel was dressed to avoid any influence of wheel wear in the final results. The acoustic emission data from these experiments were fed in a software running in a PC, that calculated all the parameters needed for the implementation of accelerated spark out. With all these parameters, the second kind of experiments of this phase were carried out. These tests used the same cutting conditions as the former experiment, but with the accelerated spark out cycle activated.

The position of the AE sensor and the experimental setup used was the same one used in the first phase of the experiments. After each cut the surface roughness, the diameter and the roundness of the part were measured.

The cutting conditions used were:

- Radial Infeed Velocity - 0.011 - 0.013 - 0.015 - 0.017 and 0.020 mm/s
- Workpiece Velocity - 0.42 m/s
- Wheel Velocity -:45 m/s
- Depth of material removed in radius - 0.15 mm
- Machine Tool - CNC grinding machine
- Wheel Specification - A A 80 K V
- Dressing Conditions:
  - Dressing Depth (a_d) : 30 μm
  - Width of the dresser (b_d) : 0.63 mm
  - Dressing Feed (s_d) : 0.26 mm/rev

Results and Discussions

Figure 5 shows an example of acoustic emission signal generated at the beginning of the cut (elastic deformation phase) in one of the experiments carried out. This figure shows clearly that acoustic emission is a very good way to establish exactly the end of the elastic deformation period in a plunge grinding cycle and so, establish τ, what is necessary to implement the accelerated spark out cycle. For the calculation of τ, a polynomial regression of the AErms x cutting time curve was done (also shown in the figure) and when this curve gets constant (its derivative reaches zero), the end of the elastic deformation phase has been reached and τ established.

Table 1 shows the values of τ for all the experiments.

Table 1 Values of τ

Infeed Speed [mm/s]	τ [ms]
0.012	4550
0.018	3820
0.024	4110

The values of τ are much bigger than usual because the stiffness of the machine used was not good. Because of this, it will not be tried to evaluate the influence of infeed speed in t values. This will be done in the second phase of experiments when a rigid and CNC machine is used.

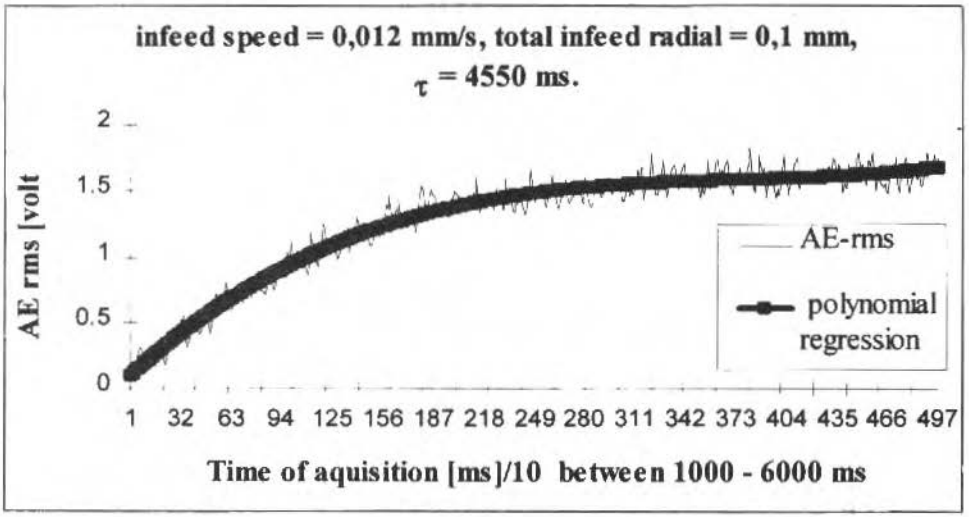

Fig. 5 Acoustic Emission in the Beginning of the Grinding Cycle

Besides the fact that acoustic emission can establish the end of the elastic deformation period in plunge grinding, other conclusions also can be made using the results obtained in this first phase of experiments:

- AE is very sensitive to small variations of the volume of material removed, what makes possible to establish the value of τ. This feature of AE may be used in other applications in the grinding process, like the exact determination of the end of spark out cycle, and
- Because AE detects very well the end of the elastic deformation cycle, it can also be used to measure the stiffness of the system machine tool - part - wheel. The bigger τ, the smaller the stiffness of the system.

With the non CNC machine, used in the first phase of the experiments, it was impossible to implement the accelerated spark out cycle. Therefore the second phase of the experiments was carried out in a CNC machine tool. Using AE monitoring it was possible to establish τ and then calculate all the parameters necessary to implement the accelerated spark out cycle, as shown previously in this work. The second phase of the experiments had the objective of implementing the accelerated spark out cycle using the values of τ (determined through the AE signals) and to compare the surface roughness and roundness of the parts obtained with those obtained using a conventional plunge grinding spark out cycle.

Figure 6 shows the behavior of the part roundness, as a function of radial infeed speed, for the two kind of cycles. This figure shows that:

- The roundness did not vary. The maximum variation among the points in the figure was less than 0.001 mm, what is equal to the error of the device used to measure it;
- The radial infeed speed does not influence roundness. The increase of roundness with radial infeed speed was also around 0.001 mm, and
- The roundness values are inside the usual range of grinding process (0.005 to 0.015 mm according to Agostinho, 1977).

Figure 7 shows the variation of surface roughness (Rmax) with radial infeed speed for both kinds of cycles. It can be seen in this figure that:

- Rmax increased smoothly with radial infeed speed in both kinds of spark out cycle. This behavior was expected because with the increase of the radial infeed speed, the stock removal rate increases, and

- The surface roughness is smaller for the accelerated cycle, what can be explained by the fact that, when the conventional cycle is used, a greater deformation remains at the point of wheel retraction as compared to the accelerated sparkout method. This deformation is caused by the friction between wheel and workpiece that generates a normal force big enough to keep the deformation in the same height of the roughness peaks. In the accelerated cycle, a large percentage of the roughness peaks is removed during the period the wheel is following the part till a position smaller than its diameter.

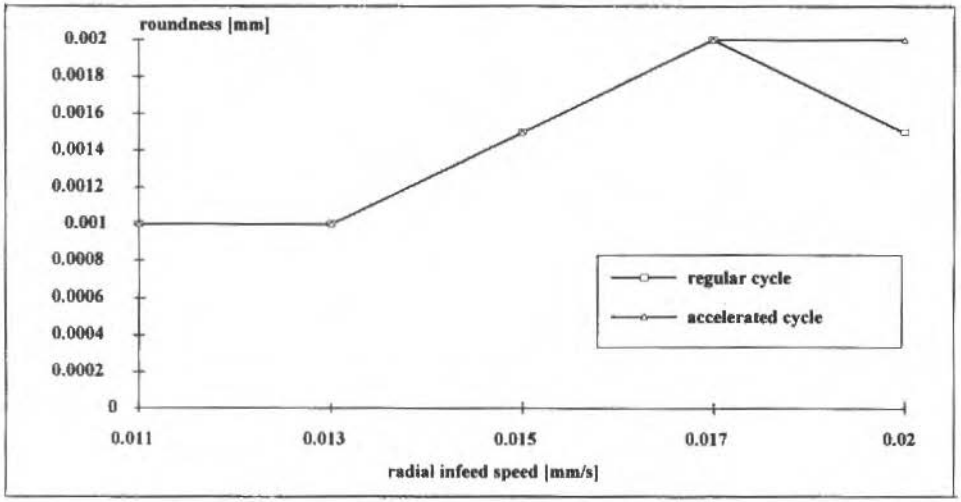

Fig. 6 Roundness of the Part against Infeed Speed

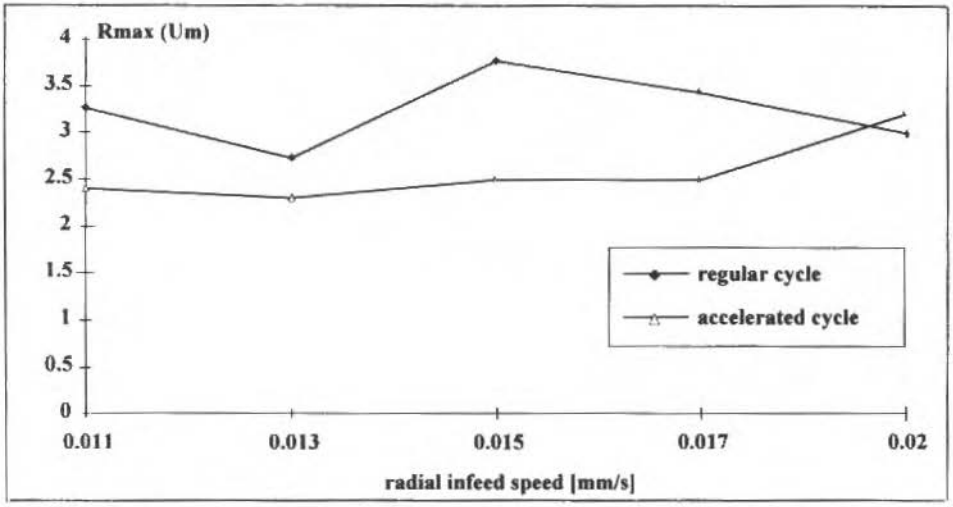

Fig. 7 Surface Roughness of the Part (Rmax) against Radial Infeed Speed

Figure 8 shows the time spent by the spark out stage using accelerated and conventional spark out against infeed speed. From this figure, it can be concluded that:

- The accelerated spark out is five to six times shorter than the conventional spark out;
- The spark out time does not depend on infeed speed. It depends mainly on the stiffness of the system and on the value of Δr_3, and

- The time saved using accelerated spark out was around 5 seconds. It is a very important economy of time, since the whole cycle lasts around 15 seconds.

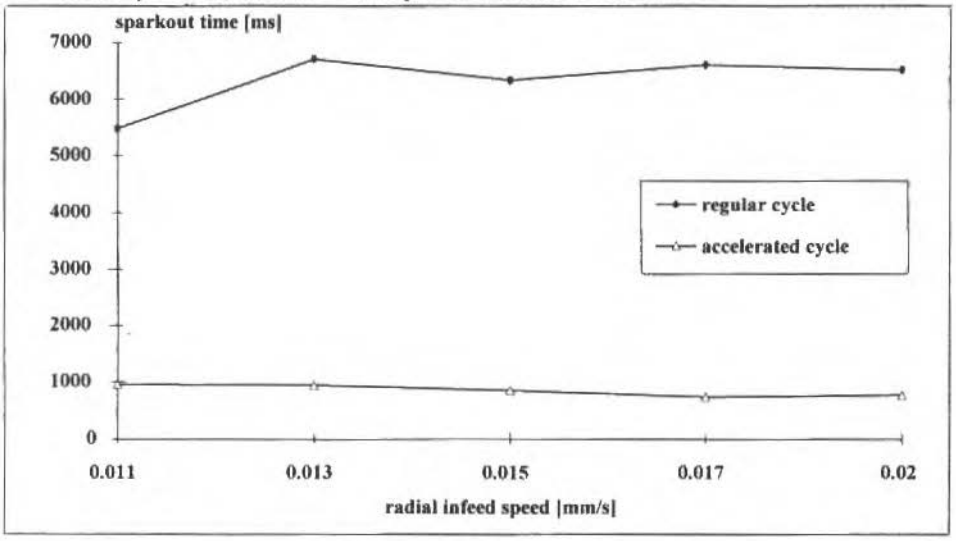

Fig. 8 Time Spent with Spark out against Infeed Speed

It is important to cite that the part diameters were always kept inside a h5 range of tolerance, even in the accelerated cycle.

Conclusions

Based on the discussions above, it can be concluded that :

- Acoustic Emission monitoring can be used to determine the amount of time (τ) spent in elastic deformations of the wheel and part in plunge grinding;
- The implementation of the accelerated plunge grinding cycle, using the equations proposed by Malkin (1989), can be done with the help of acoustic emission monitoring;
- The accelerated plunge grinding cycle does not damage the quality of the part;
- The accelerated plunge grinding cycle saves a large amount of time, when compared with the conventional cycle for a similar quality of part, and
- The next step of this work is to implement the accelerated spark out cycle in real time, i.e., to determine τ and calculate Δr_3 and u_m in the earlier stages of the cycle and automatically to inform the machine control, in order to allow the implementation in the same cycle.

References

Agostinho, O. L., Rodrigues, A. C. S., Lirani, J., and Rufino, R. T., 1977, "Tolerâncias, Ajustes, Desvios e Análises de Dimensões", Editora Edgard Blucher, São Paulo, Brazil.

Blum, T., and Inasaki, I., 1990, "A Study on Acoustic Emission from the Orthogonal Cutting Process", Transactions of ASME, Journal of Engineering for Industry, Vol. 112, pp. 203-211.

Beattie, A. G., 1983, "Acoustic Emission Principles and Instrumentation", Journal of Acoustic Emission, Vol. 2, pp. 95-128.

Blum, T., 1988, "Study of Acoustic Emission Monitoring in Metal Cutting", PhD. Thesis, Keyo University, Tokyo, Japan

Blum, T. and Dornfeld, D. A., 1990, "Grinding Process Feedback Using Acoustic Emission", 4th International Grinding Conference, Techincal Paper MR90-525, SME, Detroit, Michigan.

Dornfeld, D. A., and Cai, H. G., 1984, "An Investigation of Grinding and Wheel Loading Using Acoustic Emission", Transactions of ASME, Journal of Engineering for Industry, Vol. 106, pp. 28-33.

Eda H., et al., 1985, "In Process Detection of Grinding Cracks by the Use of Acoustic Emissions", Bulletin of the Japan Society of Precision Engineering, Vol. 19, No. 3, pp. 181-186.

Eda H., et al., 1984, "In Process Detection of Grinding Burn by Means of Utilizing Acoustic Emission", Bulletin of the Japan Society of Precision Engineering, Vol. 18, No. 4, pp. 299-304.

Inasaki, I., and Okamura, 1985, "Monitoring of Dressing and Grinding Process with Acoustic Emission Signals", Annals of the CIRP, Vol. 34, No. 1, pp. 277-280.

Kakino, Y., 1984, "Monitoring of Metal Cutting and Grinding Process by Acoustic Emission", Journal of Acoustic Emission, Vol. 3, No. 3, pp. 108-116.

Kannatey-Asibu Jr., E., and Dornfeld, D. A., 1981, "Quantitative Relationships for Acoustic Emission from Orthogonal Metal Cutting ", Transactions of ASME, Journal of Engineering for Industry, Vol. 103, No. 3, pp. 330-340.

Kannatey-Asibu Jr., E., and Dornfeld, D. A., 1982, "A Study of Tool Wear Using Statistical Analysis of Metal Cutting Acoustic Emission", Wear, Vol.76, No. 2, pp. 247-261.

Konig, W., and Meyen, H. P., 1990, "AE in Grinding and Dressing: Accuracy and Process Reliability", 4th International Grinding Conference, MR90-256, pp. 1-20.

Lan, M. S., and Dornfeld, D. A., 1982, "Experimental Studies of Tool Wear via Acoustic Emission Analysis", Proceedings of the 10th North American Manufacturing Research Conference, Hamilton, Canada, pp. 305-311.

Liu, J. J., 1991, "Monitoring the Precision Machining Process: Sensors, Signal Processing and Information Analysis", PhD. Thesis, University of California at Berkeley, Berkeley, USA.

Malkin, S., 1989, "Grinding Technology: Theory and Applications of Machining with Abrasives", Ellis Horwwod Limited Publishers, Chichester, England

RBCM - J. of the Braz. Soc. Mechanical Sciences
Vol. XVII - nº3 - 1995 - pp. 314-321

ISSN 0100-7386
Printed in Brazil

Influência de Ilhas de Calor na Capacidade Dispersiva Atmosférica

Heat Islands Influence on the Dispersion of Contaminants by the Atmosphere

R. S. Queiroz
R. A. Falbo
L. M. C. Varejão
Centro Tecnológico
Universidade Federal do Espírito Santo
CP - 01-9011 Vitória - ES - Brasil

Abstract

A two-dimensional model for atmospheric flows based on linear momentum, energy and mass conservation equations is used to simulate the effects of heat islands on the concentration field of contaminant species. The finite volume method is used to solve the equations and the results show that the concentration field is strongly dependent on local dispersive capacity.
Keywords: Atmospheric Flow, Heat Islands, Concentration Field of Contaminant Species, Local Dispersive Capacity

Resumo

Um modelo bidimensional de escoamento atmosférico baseado nas equações de conservação de momentum linear, energia e massa, é usada para simular os efeitos de ilhas de calor no campo de concentração de espécies contaminantes. O método de volumes finitos é usado para resolver as equações e os resultados mostraram que o campo de concentrações é fortemente dependente da capacidade dispersiva local.
Palavras-chave: Escoamento Atmosférico, Ilhas de Calor, Campo de Concentração de Contaminantes, Capacidade Dispersiva Local.

Introdução

A análise de características dispersivas da atmosfera tem objeto inúmeros trabalhos científicos que avaliaram analítica, numérica e experimentalmente este ambiente com o intuito principal de prever concentrações de contaminantes do ar.

Entre os muitos trabalhos publicados podemos citar alguns de reconhecida importância, tais como o trabalho de Lamb e Neiburger (1971) onde foram utilizadas formulações simplificadas para a difusividade turbulenta K; a modelagem Gausiana de formulações Lagrangeana, que permite rápidos cálculos de concentrações para diferentes classes de estabilidades atmosférica (Seinfeld, 1986); trabalhos experimentais simulando a contaminação atmosférica em camada convectiva efetuados por Willis e Deardorff (1978, 1981); trabalhos desenvolvidos por Trombetti, (1986) e Ku (1987) enfocando a solução das equações de transporte da quantidade de movimento linear, energia e massa na atmosfera utilizando métodos numéricos, associada à aplicação da teoria de similaridade de Monin-Obukhov e o trabalho de Sun (1986) que procurou estabelecer uma formulação baseada no efeito da covariância de temperatura e concentração. O estado de arte do conhecimento sobre turbulência na atmosfera e seus efeitos na estabilidade pode ser avaliado pelos trabalhos de Speziale (1991) e Wyngaard (1992).

Estudos sobre ilhas de calor surgiram ainda na década de 70 nos trabalhos de Oke (1973) e Lee (1979), que avaliaram características das ilhas de calor urbanas e suas correlações com a estabilidade atmosférica e variações da velocidade do ar.

A existência de características térmicas não homogêneas na fronteira inferior do escoamento atmosférico e sua influência na estabilidade atmosférica, principalmente localizadamente, é o objeto deste trabalho. Aplica-se um método numérico à solução das equações de transporte no escoamento atmosférico com fronteira inferior com temperatura não homogênea - "ilhas de calor"- e avaliam-se os dos efeitos da instabilidade localizada sobre as características dispersivas globais do ambiente.

Presented at the Fifth Brazilian Thermal Sciences Meeting, São Paulo, S.P. December 7-9, 1194. Techinical Editorship: ENCIT Editorial Committee

Modelagem

A região da ilha de calor é caracterizada por temperaturas na fronteira inferior maiores que a temperatura da fronteira inferior na região fora dela. Foram efetuados estudos usando duas diferentes funções para descrever as ilhas de calor: função degrau, caracterizada por uma temperatura superior à temperatura da vizinhança e função com distribuição normal de temperaturas na região das ilhas de calor.

Uma vez que o objetivo deste trabalho é o estudo da influência de ilhas de calor em planos ortogonais a elas, e não em suas laterais, as ilhas de calor foram consideradas como tendo dimensões laterais infinitas, estabelecendo uma simetria em relação ao plano vertical longitudinal e permitindo a condução do estudo da determinação dos campos de velocidade de forma bi-dimensional.

Apesar de existir uma direção preferencial de escoamento, optou-se por modelar a situação em estudo usando escoamento elíptico.

Este problema é um estudo de microescala meteorológica e, portanto, está confinado à Camada Limite Planetária, que normalmente se estende até 500 metros de altura, sendo a aceleração de Coriolis desconsiderada. A avaliação foi feita para escoamento permanente, governado pelas equações de conservação de massa (equação da continuidade), conservação de quantidade de movimento linear e conservação de energia.

Uma vez que o escoamento atmosférico é turbulento, torna-se necessária a adoção de um modelo de turbulência. Neste trabalho utilizou-se o modelo $\kappa-\varepsilon$. κ é a Energia Cinética Turbulenta, ε é a Taxa de Dissipação da Energia Cinética Turbulenta.

Para se avaliar o campo de concentrações de contaminantes, utilizou-se a equação de conservação da espécie contaminante, associada a um modelo para descrição da difusividade turbulenta (Ku, 1987).

Equacionamento

As equações utilizadas foram adimensionalizadas usando as seguintes quantidades:

$$X_i = \frac{x_i}{D} \qquad U_i = \frac{\bar{u}_i}{u_\infty} \qquad T^* = \frac{\bar{T} - T_\infty}{\Delta T}$$

$$\rho^* = \frac{\rho}{\rho_\infty} \qquad \mu_t^* = \frac{\mu_t}{\mu Re} \qquad P^* = \frac{P}{\left(\rho_\infty u_\infty^2\right)} \tag{1}$$

$$\kappa^* = \frac{\kappa}{u_\infty^2} \qquad \varepsilon^* = \frac{\varepsilon D}{u_\infty^3} \qquad C = \frac{\langle c \rangle}{C_0} \qquad K_j^* = \frac{K_j}{u_\infty D}$$

sendo P a pressão, μ a viscosidade dinâmica, K_j a difusividade turbulenta, μ_T a viscosidade turbulenta, ρ a massa específica, ρ_∞ a massa específica nas condições da corrente livre, u_∞ a velocidade da corrente livre, $\langle c \rangle$ a concentração média, D o comprimento de estudo da direção preferencial do escoamento, $\Delta T = T_{ilhamax} - T_\infty$ (onde $T_{ilhamax}$ é a maior temperatura na região da ilha de calor e T_∞ a temperatura de corrente livre), Re o número de Reynolds, dado por $Re = \rho_\infty u_\infty D/\mu$ e C_0 concentração no ponto de lançamento do contaminante. A barra superior indica valor médio.

A seguir são apresentadas as equações de conservação adimensionais e as condições de contorno associadas.

Conservação da Massa

$$\frac{\partial(\rho^* U_j)}{\partial X_j} = 0 \tag{2}$$

Conservação da Quantidade de Movimento linear

$$\frac{\partial(\rho^* U_j U_i)}{\partial X_j} = \frac{\partial}{\partial X_j}\left(\mu_t^* \frac{\partial U_i}{\partial X_j}\right) - \frac{\partial P^*}{\partial X_i} + \frac{\partial}{\partial X_j}\left(\mu_t^* \frac{\partial U_i}{\partial X_j}\right) + RiT^* \delta_{i2} \qquad (3)$$

onde Ri é o Número de Richardson, dado por Ri = Gr/Re^2, sendo Gr o Número de Grashof, dado por:

$$Gr = \frac{g\beta D^3 \Delta T \rho_\infty^2}{\mu^2}$$

onde β é o coeficiente de expansão volumétrica do gás.

Para esta equação, aplicam-se as seguintes condições de contorno:

$X_1 = 0 \qquad U_1 = \left(X_2 \frac{D}{Z_i}\right)^{1/7} \qquad U_2 = 0$

$X_1 = 1 \qquad \frac{\partial U_1}{\partial X_1} = 0 \qquad \frac{\partial U_2}{\partial X_1} = 0$

$X_2 = 0 \qquad U_1 = 0 \qquad U_2 = 0$

$X_2 = \frac{Z_i}{D} \qquad U_1 = 1 \qquad U_2 = 0$

onde Z_i é a altura da camada de mistura.

Conservação da Energia

$$\frac{\partial(\rho^* U_j T^*)}{\partial X_j} = \frac{\partial}{\partial X_j}\left(\frac{\mu_t^* \partial T^*}{\sigma T \partial X_j}\right) + EcU_j \frac{\partial P^*}{\partial X_j} \qquad (4)$$

onde Ec é número de Eckert, dado por

$$Ec = \frac{u_\infty^2}{(\Delta T c_p)}$$

e as equações de contorno aplicados foram:

$X_1 = 0 \qquad T^* = 0$

$X_1 = 1 \qquad \frac{\partial T^*}{\partial X_1} = 0$

$X_2 = \frac{Z_i}{D} \qquad T^* = 0$

$X_2 = 0 \qquad T^* = \begin{cases} e^{-\frac{(x-1/2)^2}{2(D_{ilha}/4D)^2}} & \text{na ilha de calor} \\ 0 & \text{fora da ilha de calor} \end{cases}$

e outra para os casos em que se utilizou a função degrau:

$$X_2 = 0 \qquad T^* = \begin{cases} 1 & \text{na ilha de calor} \\ 0 & \text{fora da ilha de calor} \end{cases}$$

Conservação da Energia Cinética Turbulenta

$$\frac{\partial(\rho^* U_j \kappa^*)}{\partial X_j} = \frac{\partial}{\partial X_j}\left(\frac{\mu_t^* \partial \kappa^*}{\sigma_\kappa \partial X_j}\right) + G^* - \rho^* \varepsilon^* \qquad (5)$$

sendo que os seguintes valores foram utilizados nos contornos:

$$X_1 = 0 \qquad \kappa^* = 0 \cdot 01\left(1/2 U_1^2\right)$$

$$X_1 = 1 \qquad \frac{\partial \kappa^*}{\partial X_1} = 0$$

$$X_2 = 0 \qquad \frac{\partial \kappa^*}{\partial X_2} = 0$$

$$X_2 = \frac{Z_i}{D} \qquad \frac{\partial \kappa^*}{\partial X_2} = 0$$

Conservação da Taxa de Dissipação da Energia Cinética Turbulenta

$$\frac{\partial(\rho^* U_i \varepsilon^*)}{\partial X_j} = \frac{\partial}{\partial X_j}\left(\frac{\mu_t^* \partial \varepsilon^*}{\sigma_\varepsilon \partial X_j}\right) + (C_1 G^* - C_2 \rho^* \varepsilon^*)\frac{\varepsilon^*}{\kappa^*} \qquad (6)$$

onde

$$\mu_t^* = C\mu \frac{\rho^* \kappa^{*2}}{\varepsilon^*} \qquad G = \mu_t^*\left(\frac{\partial U_i}{\partial X_j} + \frac{\partial U_j}{\partial X_i}\right)\frac{\partial U_i}{\partial X_j}$$

sendo que foram aplicadas as seguintes condições de contorno:

$$X_1 = 0 \qquad \varepsilon^* = \frac{C_\mu^{3/4} \kappa^{*3/2}}{0.4\,(\alpha Z_i / D)}$$

$$X_1 = 1 \qquad \frac{\partial \varepsilon^*}{\partial X_1} = 0$$

$$X_2 = 0 \qquad \varepsilon^* = \frac{C_\mu^{3/4} \kappa^{*3/2}}{0.4\,(y/D)}$$

$$X_2 = \frac{Z_i}{D} \qquad \frac{\partial \varepsilon^*}{\partial X_2} = 0$$

Conservação da Massa da Espécie Contaminante:

$$\frac{\partial (U_j C)}{\partial X_j} = \frac{\partial}{\partial X_j}\left(K_j^* \frac{\partial C}{\partial X_j} \right) \tag{7}$$

associada às seguintes condições de contorno:

$$X_1 = 0 \qquad C = 0$$

$$X_1 = 1 \qquad \frac{\partial C}{\partial X_1} = 0$$

$$X_2 = 0 \qquad \frac{\partial C}{\partial X_2} = 0$$

$$X_2 = \frac{Z_i}{D} \qquad \frac{\partial C}{\partial X_2} = 0$$

$$X_1 = \frac{X_{lan}}{D} \quad \text{e} \quad X_2 = \frac{H}{D}, \quad C = 1$$

Análise dos Resultados

Para resolver o conjunto de equações apresentadas anteriormente, utilizou-se o método de volumes finitos descrito por Patankar (1980), que propõe uma descretização das equações de modo a manter a conservação das variáveis em volumes de controle finitos. A solução das equações discretizadas foi obtida utilizando-se o TDMA linha por-linha com correção por blocos, segundo os princípios do algoritmo SIMPLE.

Para avaliar as respostas do modelo utilizado e as características dos campos de concentração sob influência de instabilidades localizadas, foram estudadas vários casos, com variações da velocidade de corrente livre (u_∞), altura de lançamento (H), do Número de Richardson máximo (Ri_{max}), referente à maior temperatura da ilha de calor ($T_{ilha\text{-}max}$) e da dimensão da ilha de calor (D_{ilha}).

São flagrantes as deformações no campo de concentrações devido à presença da ilha de calor, como poder ser observado pela análise das Figs. 1, 2, 3, 4 e 5. Na região da ilha é gerada uma instabilidade localizada que leva a fortes variações na difusividade turbulenta (K_v), promovendo aumento na capacidade dispersiva, o que pode ser verificado pela mudança de comportamento das linhas de isoconcentração na região próxima à ilha de calor.

É interessante observar que, uma vez fixados os parâmetros u_∞ e H, o comportamento da pluma foi idêntico nos casos sem ilha de calor (Fig. 1) e com ilha do calor (Fig. 2), até ser atinginda a região de instabilidade localizada, onde houve um flagrante alargamento da pluma.

Foi possível notar ainda que os efeitos da ilha de calor descrita por uma função normal são mais suaves que a descrita por uma função degrau, sugerindo que a adoção de formulações mais suaves para descrever as temperaturas na fronteira inferior, modelam situações físicas mais próximas da realidade.

Foi nítida a resposta do modelo à variação de velocidade, que levou a um maior alongamento das linhas de isoconcentração. Este é um reflexo do aumento de quantidade de movimento linear, que

afasta da fonte todas as linhas de isoconcentração, ou seja, há um incremento no transporte do contaminante na direção principal de escoamento e conseqüentemente uma menor dispersão das linhas em torno da horizontal determinada pela altura de lançamento. É possível observar este fato pela comparação das Figs. 1 e 3 até a posição $x_1/D = 0.40$, a partir da qual os efeitos da ilha de calor começam a ser importantes.

Pela variação da altura de lançamento, foi possível constatar que mesmo plumas provenientes de lançamentos a alturas elevadas são influenciadas pelas estrutura da turbulência gerada sobre a ilha de calor, que se reflete na difusividade turbulenta, K_v, afetando a capacidade dispersiva no domínio vertical sobre a ilha.

A influência da dimensão da ilha de calor foi avaliada e foi possível verificar como as ilhas de calor agem localizadamente, promovendo a maior dispersão. Analisando-se as Figs. 3 e 4, é possível verificar esta influência.

O aumento da capacidade dispersiva sobre a ilha de calor devido ao incremento da intensidade da ilha (diferença entre sua temperatura e a do restante da fronteira inferior) também foi verificado.

A Tabela 1 mostra as relações entre o Número de Richardson máximo (Ri_{max}), usado como parâmetro para avaliação da intensidade da ilha, velocidade de corrente livre (u_∞) e a diferença entre as temperaturas do centro da ilha e fora dela.

Tabela 1 Relações entre Ri_{max}, u_∞ e ΔT.

Ri_{max}	u_∞ (m/s)	$T_{ilha\text{-}max} - T_{solo}$(K)
100	4	4.90
100	2	1.22
400	2	4.90

Pela análise das Figs. 4 e 5 pode-se verificar como o aumento do número de Richardson influencia fortemente o aspecto do campo de concentrações.

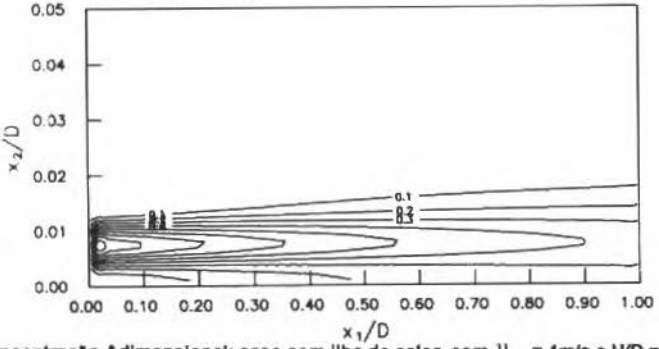

Fig. 1 Concentração Adimensional: caso sem ilha de calor, com u_∞ = 4m/s e H/D = 0.0075

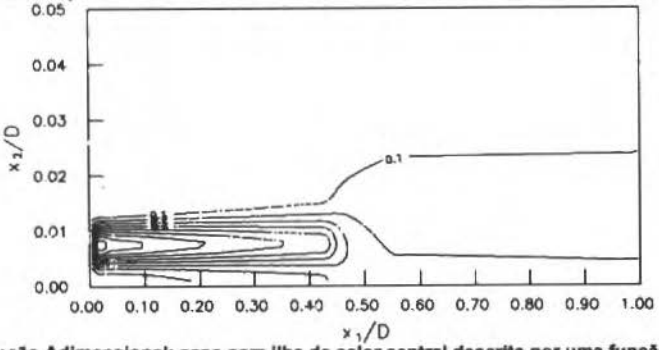

Fig.2 Concentração Adimensional: caso com ilha de calor central descrita por uma função degrau com D_{ilha}/D = 0.1, Ri_{max} = 100, u_∞ = 4 m/s e H/D = 0.0075

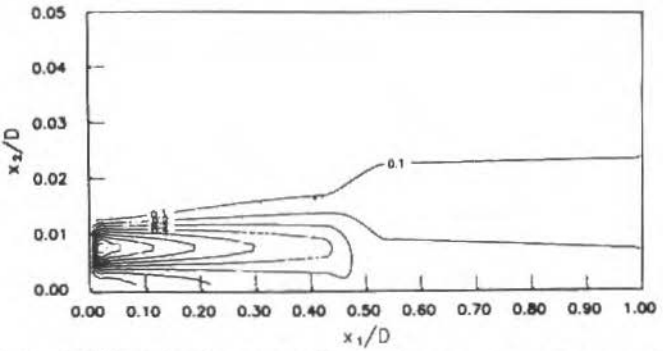

Fig. 3 Concentração Adimensional: caso com ilha de calor central descrita por uma função normal com $D_{ilha}/D = 0.1$, $Ri_{max} = 100$, $U_{\infty} = 2$ m/s e $H/D = 0.0075$

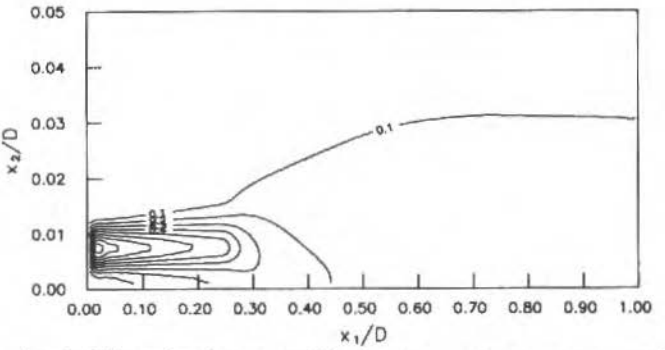

Fig. 4 Concentração Adimensional: caso com ilha de calor central descrita por uma função normal com $D_{ilha}/D = 0.5$, $Ri_{max} = 100$, $U_{\infty} = 2$ m/s e $H/D = 0.0075$

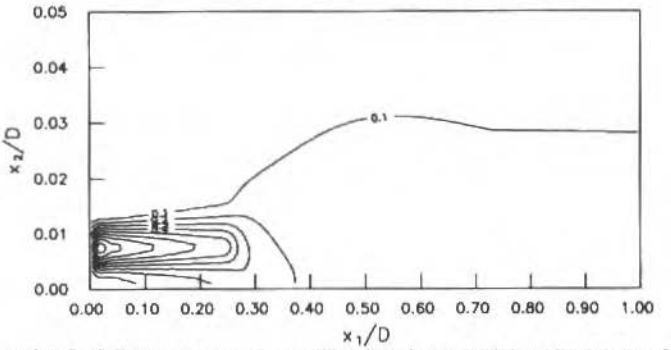

Fig. 5 Concentração Adimensional: caso com ilha de calor central descrita por uma função normal com $D_{ilha}/D = 0.5$, $Ri_{max} = 400$, $U_{\infty} = 2$ m/s e $H/D = 0.0075$

Conclusões

O modelo e o método numérico utilizados para solução do problema proposto mostraram-se adequados, fornecendo respostas fisicamente compatíveis para mudanças de parâmetros.

A ilha de calor introduzida na fronteira inferior do domínio estudado, gerando instabilidade localizada, influencia de maneira decisiva o aspecto dos campos de concentração para todos os casos estudados. O aumento da intensidade da ilha de calor reflete-se na capacidade dispersiva local via variação significativa da difusividade turbulenta.

O mecanismo de transporte de massa nas regiões fora da ilha de calor é denominado pelo campo solução da equação de transporte de quantidade de movimento linear e pela presença da difusividade turbulenta com formulação para atmosfera neutra na equação de transporte do contaminante.

Na região da ilha de calor é utilizada uma formulação para a difusividade turbulenta baseada em condições de instabilidade. Tem-se, assim, uma transição brusca relativa à capacidade dispersiva onde κ_v com formulação instável chega a ser 50 vezes maior que κ_v com formulação neutra. Muito embora a equação de energia reflita a presença da ilha de calor em qualquer ponto do domínio, a mudança brusca dos valores de κ_v na região da ilha domina os aspectos do transporte de massa do contaminante.

As características térmicas e de transporte de massa do problema estudado foram refinadas e portanto, aproximaram-se mais da realidade, ao se utilizar uma função descritora da temperatura inferior mais suave. Além disso, é notável a necessidade de se buscar uma formulação de κ_v que possa incorporar transições na capacidade dispersiva devido à aproximidade da ilha de calor, já que, claramente, o aspecto dominante é a formulação da difusividade turbulenta.

Referências

Falbo, R. A., 1993, "Simulação Numérica da Influência de Ilhas de Calor na Estabilidade e Capacidade Dispersiva da Camada Limite Convectiva Atmosférica", Dissertação de Mestrado, Departamento de Hidráulica e Saneamento da Universidade Federal do Espírito Santo.

Ku, W. S. et al., 1987, "Numerical Simulation of Air Pollution in Urban Areas: Model Development", Atmospheric Environment, Vol. 21, pp. 201-212.

Lamb. R. G. e Neiburger, M., 1971, "An Interim version of a Generalized Urban Air Pollution Model", Atmospheric Environment, Vol. 5.

Lee, D. O., 1979., "The Influence of Atmospheric Stability and the Urban Heat Island on Urban Rural Wind Speeds Differences", Atmospheric Environment, Vol. 13.

Oke, T. R., 1973, "City Size and Urban Heat Island", Atmospheric Environment, Vol. 7.

Pantakar, V. S., 1980, "Numerical Heat Transfer and Fluid Flow", Hemisphere Publishing Coorporation.

Seinfeld, J. H., 1986, "Atmospheric Chemistry and Physics of Air Pollution", Wiley Intercience Publication.

Speziale, C. G., 1991, "Analytical Methods for the Development of Reynolds-Stress Closures in Turbulence", Annu Rev. Fluid Mech, 23.

Sun, W. Y., 1986, "Air Pollution in a Convective Boundary Layer", Atmospheric Environment, Vol. 20, pp. 1817-1886.

Trombetti, F. et al., 1986, "Evaluation of Similarity Scales in the Stratified Surface Layer Using Wind Speed and Temperature Gradient", Atmospheric Environment, Vol. 20, pp. 2465-2471.

Willis, G. E., e Deardorff, J. M., 1978, "A Laboratory Study of Dispersion from an Elevated Source within a Modeled Convective Planetary Boundary Layer", Atmospheric Environment, Vol. 12, pp. 1305-1311.

Willis, G. E., e Deardorff, J. M., 1981, "A Laboratory Study of Dispersion from a Source in the Midle of the Convective Mixed Layer", Atmospheric Environment, Vol. 15, pp. 109-117.

Wyngaard, J. C., 1992, "Atmospheric Turbulence", Annu Rev. Fluid Mech, 24.

RBCM - J. of the Braz. Soc. Mechanical Sciences
Vol. XVII - nº3 - 1995 - pp. 322-330

ISSN 0100-7386
Printed in Brazil

Transferência de Massa para Jatos Espiralados Incidentes

Mass Transfer from Impinging Swirling Jets

L.G.C. Duarte
Luiz Fernando Alzuguir Azevedo
Pontifícia Universidade Católica do Rio de Janeiro
Departamento de Engenharia Mecânica
22453-900 - Rio de Janeiro, RJ - Brasil

Resumo

As características de transferência de massa de jatos turbulentos espiralados incidindo ortogonalmente sobre uma placa plana foram investigadas experimentalmente. Foram estudados os efeitos de número de Reynolds do jato, da distância jato/placa e da intensidade de escoamento espiralado dada pelo número de Swirl. Coeficientes locais e médios de transferência de massa foram obtidos utilizando-se uma mesa de coordenadadas computadorizada. Os resultados demostraram que, de uma maneira geral, a presença do escoamento reduz a troca de massa.
Palavras - Chave: Jatos Turbulentos Espiralados, Transferência de Massa, Jatos Incidentes sobre Placa Plana

Abstract

The present work is an experimental study of the mass transfer characteristics of a swirling jet impinging on a flat plate. The main objective of the investigation was to determine the influence of a circunferential velocity component (the swirl component) on the local and average mass transfer coefficients at the plate surface. The dimensionless parameters investigated were the jet Reynolds number, the jet-to-plate distance, and the strength of the swirl flow given by the swirl number. Mass transfer coefficients were obtained utilizing the naphthalene sublimation technique. The local coefficients were determined employing a computerized coordinate table which allowed a detailed study of the effects of the presence of the swirl component. Average coefficients were determined independently through precision weighing, and displayed excellent agreement with the integrated local coefficients. The results demonstrated that the presence of the swirl component decreases the mass transfer coefficients, when compared with than non swirl case.
Keywords: Mass Transfer, Swirling Jet, Jet Imping on a Flat Plate

Introdução

Jatos incidindo sobre superfícies produzem as mais elevadas taxas de transferência de calor ou massa que podem ser obtidas em escoamentos monofásicos e, por razão, são largamente empregados na indústria. O uso de jatos no aquecimento, resfriamento ou secagem é encontrado em várias aplicações, dentre as quais destacam-se secagem de papel e tecido, a têmpera de vidro, o aquecimento e resfriamento de metais, o resfriamento de palhetas de turbinas e de componentes eletrônicos.

Uma revisão da literatura relacionada com jatos incidentes revela um grande número de trabalhos investigando vários aspectos desta configuração. Os resultados destes trabalhos de pesquisa estão resumidos nos artigos de revisão publicados por Martin (1977) e Downs e James (1987). Os trabalhos citados incluem descrições dos diversos parâmetros que influenciam a troca de calor oû massa para jatos. Estes parâmetros incluem os efeitos geométricos tais como, espaçamento e diâmetro do jato, forma de seção reta do jato, número de Reynolds, intensidade de turbulência, efeitos de temperatura, ângulo de incidência do jato e curvatura da superfície. Também foram investigadas na literatura as características de transferência de calor e massa do conjunto de jatos incidentes, e a influência da forma com que o fluido utilizado é descartado para o ambiente.

Mais recentemente os trabalhos publicados na literatura indicam um crescente interesse no estudo de jatos incidentes de líquido. Stevens e Webb (1991) estudaram a troca de calor para jatos de líquido com ênfase na estrutura da superfície livre e dos efeitos causados pela inclinação do jato. Zumbrunnen e Aziz (1993) investigaram a troca de calor para jatos intermitentes de líquido, enquanto Liu, Gabour e Lienhard (1993) incluíram efeitos de tensão superficial. As aplicações de resfriamento de componentes eletrônicos com altas taxas de geração de calor têm motivado o estudo de jatos de líquido incidindo em pequenas superfícies aquecidas (Slayzak et al., 1994 e Womac et al., 1993).

Presented at the Fifth Brazilian Thermal Sciences Meeting, São Paulo, S.P. December 7-9, 1994. Technical Editorship: ENCIT Editorial Committee

Apesar do grande número de publicações relacionadas com jatos incidentes, os efeitos da presença de um componente circunferencial na velocidade do jato foram pouco explorados. Estes jatos espiralados encontram grande aplicação em combustores, onde o componente circunferencial de velocidade é introduzido com o objetivo de homogeneizar a mistura e estabilizar a chama. Em muitas aplicações, jatos provenientes de combustores são utilizados diretamente no aquecimento de chapas para tratamento térmico, sendo necessário o conhecimento dos coeficientes médios e locais de troca de calor para o projeto destes equipamentos.

Martin (1977) em seu extenso trabalho de revisão menciona, sem apresentar dados numéricos, que a presença do componente circunferencial na velocidade de um jato incidente não produz alterações significativas na troca de calor ou massa. Ward e Mahmood (1982), no entanto, apresentam conclusões opostas às de Martin, indicando que a presença do escoamento espiralado reduz significativamente a troca de calor ou massa. Este trabalho é bastante limitado, apresentando resultados de troca de calor local para apenas um valor do número de Reynolds do jato. É apresentada também uma correlação para o número de Nusselt médio em função da distância adimensional do jato à placa, do número de Prandtl, do número de Reynolds e da intensidade do escoamento espiralado. A acurácia desta correlação deve ser verificada, visto que foi construída com dados de apenas dois valores do número de Reynolds.

O objetivo do presente trabalho é apresentar dados detalhados sobre as características de transferência de massa da configuração formada por um jato de ar espiralado incidindo ortogonalmente sobre uma placa plana. Estes resultados além de esclarecerem as divergências entre os trabalhos de Martin e Ward e Mahmood, fornecem informações locais e médias sobre esta configuração não disponíveis até o presente.

Descrição do Experimento

As informações desejadas sobre os coeficientes de troca para o jato incidente espiralado foram obtidas neste trabalho utilizando-se a técnica de sublimação do naftaleno (Souza Mendes, 1991). Esta técnica além de permitir a medição de coeficientes médios de troca de massa, permite também a obtenção da distribuição detalhada dos coeficientes locais de troca de massa.

Para sua implementação, uma superfície plana de naftaleno é fabricada, sobre ela incidindo o jato de ar espiralado a ser estudado. Este jato provoca a sublimação do naftaleno, acarretando perda de massa que pode ser avaliada e relacionada com os coeficientes de troca da mesma. A pesagem da placa de naftaleno antes e depois da exposição ao ar fornece o coeficiente médio de troca da massa, enquanto a distribuição espacial do coeficiente local de troca de massa é obtida através de um detalhado levantamento topográfico realizado sobre a superfície de naftaleno antes e depois da exposição ao ar. Como será descrito a seguir, este levantamento foi realizado neste trabalho utilizando-se uma mesa de coordenadas computadorizada, especialmente construída para este fim.

Seção de Testes. Para a obtenção de resultados confiáveis com a técnica de sublimação de naftaleno é necessário que o experimento seja realizado com temperatura constante. Por esta razão, foi necessário construir uma seção de testes que permitisse a formação de um jato incidente proveniente de um ambiente com temperatura constante.

A Fig. 1 (a) auxilia a descrição da seção de testes construída. O ar succionado por um exaustor colocado fora do laboratório era forçado a passar por uma câmara geradora de escoamento espiralado, por uma câmara reguladora do escoamento espiralado, através do tubo que formava o jato, incidindo sobre a placa de naftaleno posicionada no interior de um tanque de grandes dimensões. Após incidir sobre a placa, o ar contendo vapor de naftaleno era conduzido para o exterior do laboratório através de uma tubulação que continha uma placa de orifício para medida de vazão, uma válvula de esfera para corte rápido do fluxo de ar e uma válvula globo para controle da vazão. O tanque possuía uma janela removível que permitia a manipulação da placa de naftaleno, quando desejado.

A seção geradora do escoamento espiralado era formada por um tubo fechado em sua extremidade superior e aberto em sua extremidade inferior. Na superfície lateral deste tubo foram usinadas quatro fileiras de 25 furos com 1,5 mm de diâmetro, dispostos verticalmente ao longo da geratriz do tubo, formando um total de 100 furos passantes. As fileiras eram espaçadas circunferencialmente de 90

graus. Os furos foram usinados cuidadosamente de forma a serem tangentes à circunferência interna do tubo. Desta forma, o ar succionado pelo exaustor penetrava na câmara geradora tangencialmente, produzindo o componente circunferencial de velocidade desejado.

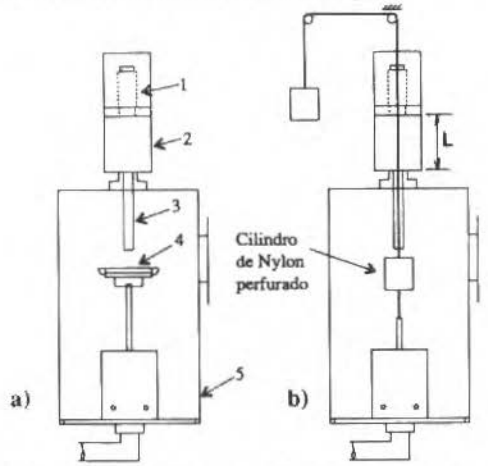

Fig. 1a Seção de Testes: 1-Câmara geradora, 2-Câmara reguladora, 3-Jato, 4-Placa, 5-Tanque. 1b) Seção Medidora de Swirl.

O escoamento espiralado produzido na câmara geradora penetrava na câmara reguladora, que era formada por um tubo de acrílico tendo em sua extremidade inferior uma tampa adaptada ao tubo do jato, e em sua extremidade superior em êmbolo adaptado à câmara geradora. O êmbolo, solidário à câmara geradora, podia ser movimentado verticalmente, de forma a variar as dimensões da câmara reguladora. A variação da posição vertical do êmbolo na câmara reguladora influía na taxa de decaimento do escoamento espiralado, permitindo o controle de intensidade do escoamento espiralado que penetrava no tubo e iria posteriormente incidir sobre a placa de naftaleno. Quando o êmbolo era posicionado no fundo da câmara reguladora, produzia-se a maior intensidade do escoamento espiralado, para uma determinada vazão de trabalho.

A placa de naftaleno era formada a partir da fundição do naftaleno líquido sobre um cassete circular de alumínio. Este cassete tinha a finalidade de dar rigidez à superfície de naftaleno e de impedir a exposição ao ar das superfícies inferior e lateral da placa do naftaleno. Desta forma, somente a superfície superior da placa era exposta ao jato de ar. Na operação de fundição o cassete era montado sobre uma superfície metálica polida, de maneira que, quando desmoldada, a superfície de naftaleno produzida apresentava excelente acabamento superficial. O cassete de alumínio contendo placa de naftaleno era colocado sobre um suporte ajustável no interior da seção de testes. Ajustando-se a posição do suporte podia-se variar a distância jato/placa, um dos parâmetros investigados no presente estudo.

Medição de Intensidade do Escoamento Espiralado. A intensidade do escoamento espiralado é normalmente caracterizada pelo número de Swirl, definido como a razão entre a quantidade de movimento angular do jato dividida pelo raio do tubo multiplicado pela quantidade de movimento linear. A quantidade de movimento linear do jato pode ser obtida facilmente das medidas de vazão, e assumindo-se um perfil típico de velocidade no tubo. A medida da quantidade de movimento angular do jato, requereu a construção de um sistema especial de medição, como será descrito a seguir.

A medida da quantidade de movimento angular do escoamento na saída do jato foi obtida através da utilização do princípio de conservação da quantidade de movimento angular e da medição do torque produzido pelo escoamento. A Fig. 1 (b), apresenta esquematicamente o experimento montado. Um cilindro de nylon de 70 mm de diâmetro perfurado longitudinalmente por 60 furos de 6 mm de diâmetro era colocado em frente à saída do jato, no interior do tanque. Um fio de aço de 0,2 mm de diâmetro solidário ao cilindro era fixado em uma extremidade na base que acomodava a placa de naftaleno (removida nestes experimentos). A outra extremidade do fio era fixada a uma massa de 6 kg, depois de passar pelo centro do tubo do jato, pelas câmaras reguladoras e geradoras de escoamento

espiralado e por um par de roldanas fixadas ao teto do laboratório. Um pequeno furo na tampa superior da câmara geradora de escoamento espiralado permitia a passagem do fio. O jato de ar penetrava nos furos transferindo sua quantidade de movimento angular para o cilindro, provocando um torque que era equilibrado pela torção do fio. A medição ótica da rotação do cilindro e um procedimento de calibração do conjunto cilindro/fio permitiam a determinação do torque, o qual era igualado à quantidade de movimento angular desejada. O número de Swirl podia assim ser determinado. Os detalhes da construção e calibração do torquímetro, podem ser encontrados no trabalho de Duarte (1994).

Medida dos Coeficientes de Troca de Massa. Os coeficientes médios de troca de massa eram obtidos a partir de pesagem do cassete contendo o naftaleno, antes e depois da exposição ao escoamento. Para isto utilizou-se uma balança analítica com resolução da ordem de 0,1 mg.

Os coeficientes locais de troca de massa eram obtidos realizando-se um levantamento topográfico da superfície de naftaleno antes e depois do escoamento. A superfície de naftaleno era posicionada sobre uma mesa de coordenadas computadorizada com resolução espacial da ordem de 0,01 mm. Estas mesa movimentava a superfície sob um apalpador digital fixo com resolução de 0,5 μm , realizando medidas em posições previamente estabelecidas, e armazenando as leituras no computador controlador do sistema. As medidas em um mesmo ponto, realizadas antes e depois do escoamento eram subtraídas, o que fornecia a profundidade de sublimação naquela determinada posição. Experimentos preliminares com medições realizadas ao longo de 8 diâmetros demostraram a perfeita simetria circular do escoamento. Por esta razão, os resultados locais foram obtidos realizando-se medições em pontos ao longo de dois diâmetros ortogonais. Duzentos e setenta pontos eram medidos ao longo de cada diâmetro o que tipicamente, requeria 7 minutos de operação do sistema de medição.

Redução dos Dados. A redução dos dados experimentais tinha como objetivo o cálculo dos números de Reynolds e Swirl do jato e dos números de Sherwood local e médio, adimensionais que, juntamente com a distância adimensional jato/placa, governam o problema em estudo.

O número de Reynolds era calculado a partir da vazão mássica, m, medida na placa de orifício, como

$$Re = 4m/\pi D\mu \qquad (1)$$

onde, D é o diâmetro do jato e μ a viscosidade absoluta do ar.

O número de Swirl, era definido como,

$$S = G_{\varphi}/RG_x \qquad (2)$$

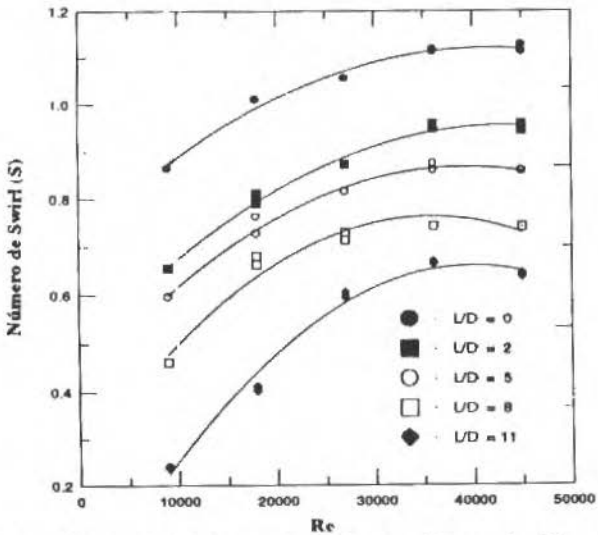

Fig. 2 Número de Swirl versus Reynolds, para jato com D = 22mm.

onde Gφ e Gx representaram as quantidades de movimento angular e axial do jato, e R é o raio do tubo. A quantidade de movimento angular era tomada como sendo igual ao torque medido no torquímetro, enquanto a quantidade de movimento axial era calculada assumindo-se um perfil uniforme no jato com velocidade média V. Assim,

$$G_x = \pi\rho V^2 R^2 \tag{3}$$

Curvas auxiliares apresentando o número de Swirl como função do número de Reynolds foram construídas a partir dos experimentos de calibração do torquímetro, para cada valor do diâmetro do tubo utilizado, e para cada posição L/D do êmbolo na câmara controladora do escoamento espiralado. Estas curvas eram utilizadas para estabelecer o número de Swirl em cada experimento de troca de massa a ser realizado. A Fig. 2 apresenta uma destas curvas, obtida para um tubo com diâmetro igual a 22 mm.

O coeficiente médio de troca de massa para a placa circular de naftaleno, K, era obtido pela pesagem e cronometragem do tempo de exposição da superfície ao jato de ar. Este coeficiente era calculado pela expressão,

$$K = \Delta M/\tau A \Delta\rho_n \tag{4}$$

onde, ΔM é a massa de naftaleno sublimada durante o experimento, obtida por pesagem antes e depois da exposição ao jato, τ é o tempo de exposição ao jato, A é a área de troca da placa e é $\Delta\rho_n$ a diferença de massa específica do vapor de naftaleno na superfície sólida e no ar. Como o ar é considerado isento de naftaleno, $\Delta\rho_n$ é simplesmente a massa específica do vapor na superfície sólida. Este valor pode ser obtido a partir da medição da temperatura da superfície de naftaleno em conjunto com a equação de Sogin citada em Souza Mendes (1991).

O coeficiente local de troca de massa, k, foi determinado pela expressão,

$$k = m/\Delta\rho_n \qquad \text{com} \qquad m = \rho_{ns}\Delta Y/\tau \tag{5}$$

onde m é a taxa de transferência de massa local por unidade de área, ρ_{ns} é a massa específica do naftaleno sólido, ΔY, a profundidade de sublimação do naftaleno medida com o apalpador e τ, o tempo de exposição ao jato de ar.

Os coeficientes adimensionais médio e local de troca de massa foram utilizados nas apresentações dos resultados na forma de números de Sherwood médio, SH, e Sherwood local, Sh_l, definidos como,

$$Sh = \rho_{ar}KDSc/\mu_{ar} \qquad e \qquad Sh_l = \rho_{ar}kDSc/\mu_{ar} \tag{6}$$

onde Sc representa o número de Schmidt para o vapor de naftaleno no ar e ρ_{ar} e μ_{ar} são, respectivamente, a massa específica e viscosidade absoluta do ar.

Resultados e Discussão

Nesta seção serão apresentados os resultados de transferência de massa obtidos nos experimentos realizados. Os experimentos foram realizados para números de Reynolds iguais a 9000, 27000, 36000 e 45000. Para cada valor do número de Reynolds, foram investigados três valores da distância adimensional jato/placa (H/D = 2, 4 e 8) e três valores da intensidade do escoamento espiralado caracterizado pelo número de Swirl (S = 0,28, 0,54 e 0,74). Experimentos foram também realizados

para o caso base formado pelo jato não espiralado (S = 0). Estes experimentos foram usados como base de comparação para os efeitos de escoamento espiralado. Ao todo 60 experimentos foram realizados mas, por limitação de espaço, apenas alguns resultados serão apresentados. Os resultados completos podem ser encontrados em Duarte (1994).

A distribuição radial do número de Sherwood local é apresentada nas Figs. 3,4 e 5, respectivamente, para H/D igual a 2,4 e 8 e para Re = 9000. Nestas figuras, a intensidade do escoamento espiralado investigada está caracterizada pelos números de Swirl, identificados na legenda. O caso base, correspondente a S = 0, está também representado para facilitar as comparações.

Uma observação geral das Figs 3,4 e 5 mostra que o efeito preponderante da presença do escoamento espiralado é no sentido de diminuir o número de Sherwood local em comparação como o caso base onde o escoamento não é espiralado.

Para pequenas e médias distâncias jato/placa (H/D = 2 e 4), o comportamento das distribuições de Sh_l é semelhante. Nota-se uma forte redução em Sh_l na região de estagnação, seguida de uma recuperação e um comportamento assintótico tendendo para os valores de Sherwood do caso base.

Estes resultados podem ser explicados pelas alterações impostas no perfil de velocidade do jato pela presença do componente de velocidade circunferencial. De fato, é descrito na literatura (Ward e Mahmood, 1982), que a presença de um componente circunferencial em um jato livre provoca um deslocamento do ponto de máxima velocidade da linha de simetria do jato no caso base para posições radiais da ordem do raio do tubo. Dependendo da intensidade do número de Swirl, pode-se até produzir reversão do escoamento na linha de simetria do jato. A redução de Sh_l na linha de centro, assim como os picos na distribuição em torno de r/D = 1, são o reflexo da nova configuração do perfil de velocidade. Experimentos de visualização realizados utilizando a técnica de óleo com negro de fumo, confirmaram a presença de reversão de escoamento na região de estagnação para altos valores de S.

À medida que o jato é afastado da placa, a distribuição de Sh_l é alterada em alguns aspectos. Como pode ser observado, os picos na região r/D = 1 presentes no caso de menor H/D, não são mais notados para baixos valores de S, apresentando-se bastante atenuados para valores maiores de S. A drástica redução em Sh_l na região de estagnação e a tendência à assintotização para os valores do caso base continuam, no entanto, presentes.

Para números de Reynolds intermediários (18000 e 27000) a tendência geral de diminuição de Sh_l com a presença do escoamento espiralado é mantido. No entanto notou-se que a diminuição de Sh_l na região de estagnação não é tão pronunciada como no caso de baixos Re, indicando que a quantidade de movimento linear do jato foi aumentada em comparação com o gradiente de pressão adverso gerado pelo escoamento espiralado, de forma a não provocar reduções tão drásticas na velocidade axial do fluido nesta região.

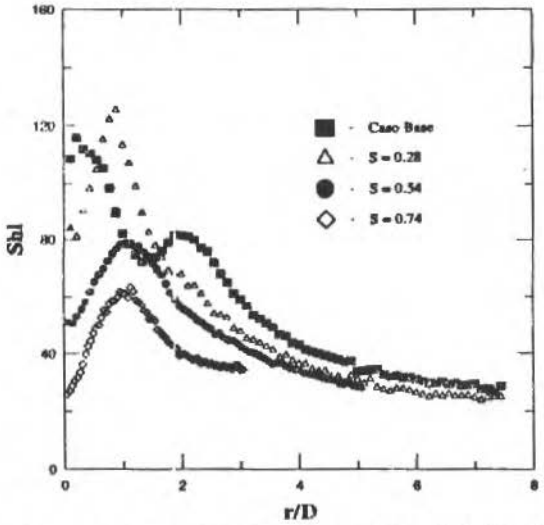

Fig. 3 Distribuição Radial de Sherwood,Re = 9000, H/D = 2

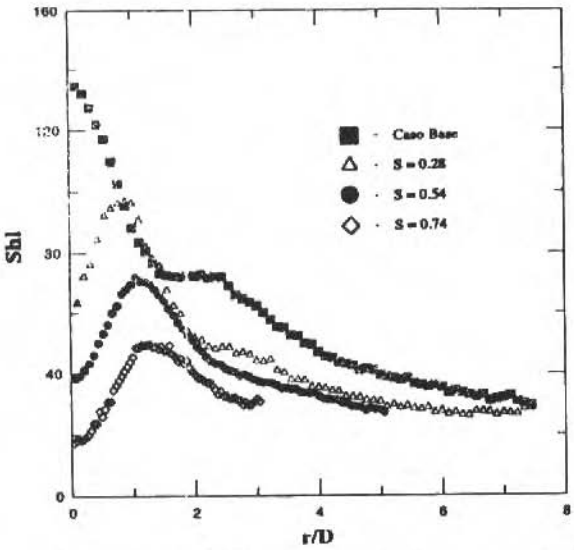

Fig. 4 Distribuição Radial de Sherwood,Re = 9000, H/D = 4

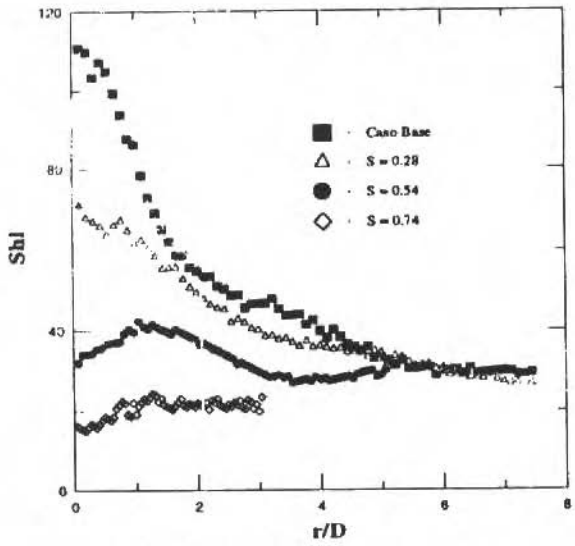

Fig. 5 Distribuição Radial de Sherwood,Re = 9000, H/D = 8

No caso dos maiores Re investigados, mostrados nas Figs. 6, 7, pode-se observar o mesmo comportamento qualitativo descrito para os outros valores de Reynolds. Uma comparação de casos com a mesma distância jato/placa e diferentes Re, mostra que quanto maior o número de Reynolds maior o número de Swirl necessário para alterar a forma da distribuição local de Sherwood.

Os números de Sherwood locais foram integrados ao longo da área da placa até uma distância r/D = 3, de modo a fornecer valores médios de Sherwood para esta região. Os resultados obtidos mostram que a razão este número de Sherwood médio e o Sherwood médio correspondente ao caso base, Sh/Sh_{cb}, são insensíveis à distância jato/placa e fracamente dependentes do número de Reynolds,

dependendo apenas da intensidade do escoamento espiralado dada pelo número de Swirl. Assim, para S = 0,28, 0,54, e 0,74, a razão Sh/Sh_{cb} vale, respectivamente, 0,8, 0,6 e 0,3, revelando a significativa queda na troca de massa média provocada pela presença do componente circunferencial na velocidade do jato incidente.

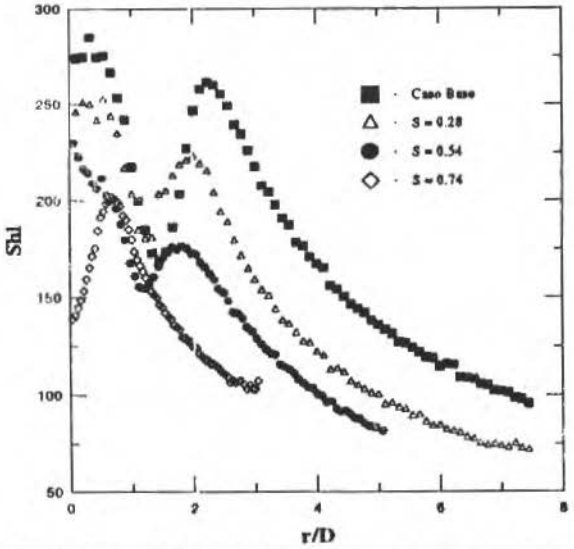

Fig. 6 Distribuição Radial de Sherwood,Re = 45000, H/D = 2

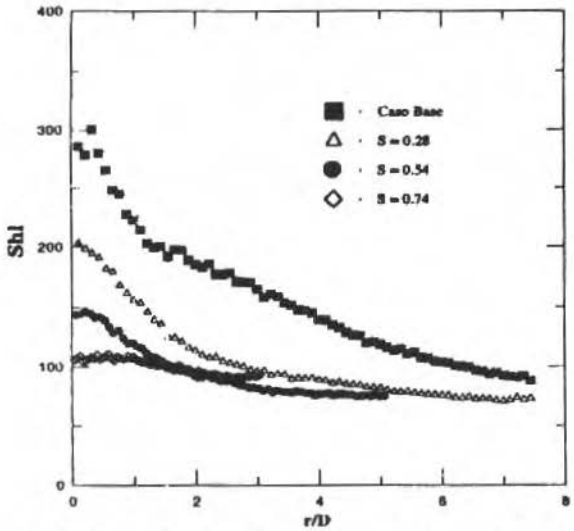

Fig. 7 Distribuição Radial de Sherwood,Re = 45000, H/D = 8

Conclusão

O presente trabalho investigou experimentalmente a transferência de massa para jatos turbulentos espiralados incidindo ortogonalmente sobre uma superfície plana. Foram estudados os efeitos sobre a transferência de massa do número de Reynolds do jato, da distância jato/placa e da intensidade do escoamento espiralado dada pelo número de Swirl. Os experimentos realizados permitiram a obtenção

de informações detalhadas sobre a distribuição espacial dos coeficientes de troca de massa na superfície da placa, assim como os coeficientes médios de troca de massa. A técnica de sublimação de naftaleno foi utilizada em conjunto com um sistema automatizado para realização das medidas locais.

Os resultados revelaram que, de uma maneira geral, a presença de um componente circunferencial no escoamento do jato produz uma diminuição nos coeficientes de troca de massa, quando comparados ao caso base de escoamento não espiralado. Em particular, verificou-se uma significativa diminuição dos coeficientes de troca de massa na região de estagnação do jato.

Os coeficientes médios de troca apresentaram também diminuição em relação ao caso base.

Referências

Duarte, L.G.C., 1994, "Transferência de Massa para Jatos Espiralados e Incidentes", Dissertação de Mestrado, Pontifícia Universidade Católica do Rio de Janeiro, RJ, Brasil.

Liu, X., Gabour, L.A. e Lienhard, J.H., 1993,"Stagnation-Point Heat Transfer During Impingement of Laminar Liquid Jets: Analysis Including Surface Tension", ASME J. Heat Transfer, pp. 99-105.

Martin, H., 1977, "Heat and Mass Transfer Between Impinging Gas Jets and Solid Surfaces", em Advances of Heat Transfer, pp. 1-60.

Souza Mendes, P.R., 1991, "The Naphthalene Sublimation Technique", Experimental Thermal and Fluid Science, pp. 510-523.

Stevens, J. and Webb, B., 1991., "Local Heat Transfer Coefficients under an Axisymmetric, Single-Phase Liquid Jet", ASME J. Heat Transfer, pp. 3-17.

Ward, J. e Mahmood, M., 1982, "Heat Transfer From a Turbulent Swirling Jet", Proc. 7th Int. Heat Mass Transfer Conference, pp. 401-408.

Womac, D.J., Ramadhyani, S., e Incropera, F.P., 1993, "Correlating Equations for Impingement Cooling of Small Heat Sources With Single Circular Liquid Jets", ASME J. Heat Transfer, pp. 88-95.

Zumbrunnen, D.A., e Aziz, M., 1993, "Convective Heat Transfer Enhancement Due to Intermittency in an Impinging Jet", ASME J. Heat Transfer, pp. 91-98.

RBCM - J. of the Braz. Soc. Mechanical Sciences
Vol. XVII - n°3 - 1995 - pp. 331-339

ISSN 0100-7386
Printed in Brazil

Mixed - Convection in Flows of Viscoelastic Liquids - A Parametric Study

M. F. Naccache
Paulo Roberto Souza Mendes
Department of Mechanical Engineering
Pontifícia Universidade Católica do Rio de Janeiro
22453-900 Rio de Janeiro, RJ Brazil.

Abstract

A parametric analysis of the viscoelastic laminar flow through rectangular ducts is presented, which gives a generic insight of the relative importance of physical parameters. The effects of the elastic and buoyancy forces on flow patterns and on heat transfer are analyzed, as well as the effects of the Reynolds, Prandtl and Weissenberg numbers. The results show the existence of a physical dimensionless parameter which gives the relative influence of the elastic and buoyancy effects on flow patterns and heat transfer
Keywords: Viscoelastic Liquid, Flow Through Rectangular Duct, Elastic Force, Buoyance Force, Flow Pattern, Heat-Transfer

Introduction

Flows of viscoelastic liquids inside rectangular ducts are known to present secondary flows that increase the heat transfer coefficient significantly.

In order to better understand the heat transfer mechanisms involved in this flow situation, a parametric study is helpful. For Newtonian fluids, because the only rheological property is the viscosity, which is a constant for a give fluid, this kind of analysis is typically straightfoward. For flows of viscoelastic fluids some difficulty arises because there are a number of rhelogical properties involved, which are often functions of the flow kinematics.

Because of the small velocities in flows of polymetric solutions, buoyancy forces may play an important role. These forces interacts with the viscoelastic forces and causes several changes in flow patterns and the heat transfer coefficient behavior.

Analysis

The problem under study is shown in Fig. 1. The flow is assumed to be laminar, hydrodynamically and thermally developed. The fluid is incompressible with temperature - independent properties.

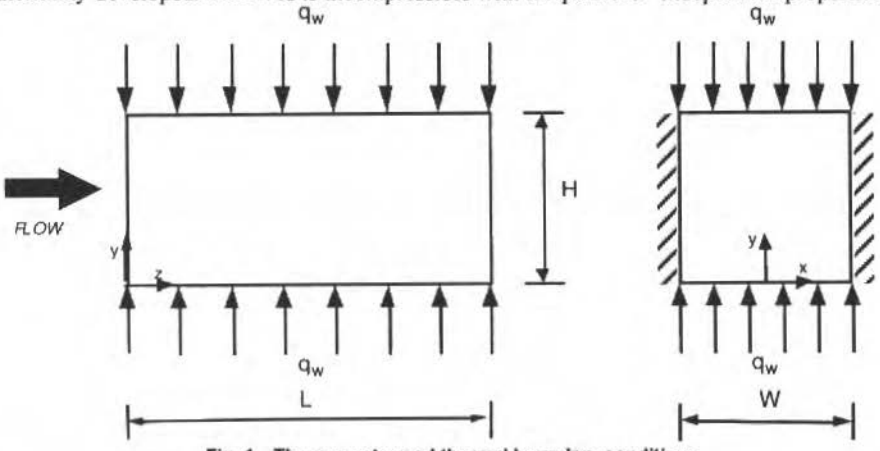

Fig. 1 The geometry and thermal boundary conditions

Presented at the Fifth Brazilian Thermal Sciences Meeting, São Paulo, S.P. December 7-9, 1994. Technical Editorship: ENCIT Editorial Committee

The problem solution is obtained by solving the conservation equations of mass, momentum and energy. In order to model the non-Newtonian behavior of the fluid the CEF constitutive relation (Criminale et al., 1958) is used.

$$\tau = \eta(\dot{\gamma})\dot{\gamma} - \frac{1}{2}\Psi_1(\dot{\gamma})\gamma_{[2]} + \Psi_2(\dot{\gamma})\dot{\gamma}^2 \tag{1}$$

τ is the extra-stress tensor (the part of the stress tensor that vanishes when there is no motion other than rigid-body translation and rotation) and $\dot{\gamma} = \text{grad } \mathbf{v} + (\text{grad } \mathbf{v})^T$ is the rate-of-strain tensor. The scalar rate of strain $\dot{\gamma}$ is defined as $\dot{\gamma} \equiv \sqrt{\frac{1}{2}\text{tr}\dot{\gamma}^2}$. The tensorial quantity $\dot{\gamma}_{[2]}$ is the convected derivative of the rate-of-strain, tensor, defined as

$$\gamma_{[2]} \equiv \frac{d\dot{\gamma}}{dt} - \left[(\text{gradv})^T\dot{\gamma} + \dot{\gamma}(\text{gradv})\right] \tag{2}$$

$\eta(\dot{\gamma})$, $\Psi_1(\dot{\gamma})$ and $\Psi_2(\dot{\gamma})$ are respectively the viscosity, first and second normal stress coefficientes. The operator d/dt is the material time derivative.

The extra stress can be decomposed into a Newtonian term τ^N and a non-Newtoniam (or polymeric) term τ^P, so that $\tau = \tau^N + \tau^P$:

$$\tau^N \equiv \eta(\dot{\gamma})\dot{\gamma} \; ; \; \tau^P \equiv -\frac{1}{2}\Psi_1(\dot{\gamma})\gamma_{[2]} + \Psi_2(\dot{\gamma})\dot{\gamma}^2 \tag{3}$$

The viscosity function employed is of the Carreau-Yasuda type:

$$\eta(\dot{\gamma}) = \eta_\infty + (\eta_0 - \eta_\infty)\,1 + (\lambda\dot{\gamma})^{a(n-1/a)} \tag{4}$$

In dimensionless form, the viscosity function can be written as:

$$\eta^*(\dot{\gamma}^*) \equiv \frac{\eta(\dot{\gamma})}{\eta(\dot{\gamma}_{char})} = \eta^*_\infty + (\eta^*_0 - \eta^*_\infty)\left[1 + \left(We\dot{\gamma}^*\right)^a\right]^{(n-1/a)} \tag{5}$$

where $\eta^*_\infty = \eta_\infty/\eta_{char}$, $\eta_0^* = \eta_0/\eta_{char}$. The Weissenberg number is defined as $We = \lambda\dot{\gamma}_{char}$ and $\dot{\gamma} = \dot{\gamma}/\dot{\gamma}_{char}$. The quantities $\lambda\dot{\gamma}_{char}$ and η_{char} are the characteristic shear rate ($\dot{\gamma} \equiv v_{char}/D_h$) and the characteristic viscosity function ($\eta_{char} \equiv \eta(\dot{\gamma}_{char})$). The characteristic velocity is defined as $v_{char} = -(\partial p/\partial z)\, D_h^2/\eta_{char}$, while D_h is the hydraulic diameter, given by 2H (1 + H/W). As usual, $\partial p/\partial z$ is the pressure gradient in the flow direction. Some dimensionless quantities of importance are defined below:

$$U \equiv \frac{u}{v_{char}} \; ; \; V \equiv \frac{u}{v_{char}} \; ; \; W \equiv \frac{\omega}{v_{char}} \; ; \; \theta \equiv \frac{T - T_b}{q_w D_H/\kappa} \tag{6}$$

$$X \equiv \frac{x}{D_H} \; ; \; Y \equiv \frac{y}{D_H} \; ; \; Z \equiv \frac{z}{D_H} \; ; \; \dot{\gamma}^* \equiv \frac{\dot{\gamma}}{\dot{\gamma}_{char}} \tag{7}$$

$$P \equiv \frac{p + \rho g y}{\rho v_{char^2}} \qquad \tau^* \equiv \frac{\tau}{\rho v^2_{char}} \tag{8}$$

Using the definitions above, the dimensionless governing equations take the following form:

- Mass Conservation:

$$\frac{\partial U}{\partial X}+\frac{\partial V}{\partial Y}=0 \tag{9}$$

- Momentum:

$$U\frac{\partial U}{\partial X}+V\frac{\partial U}{\partial Y}=-\frac{\partial P}{\partial X}+\frac{1}{Re}\left(\frac{\partial}{\partial X}\left(2\eta^*\frac{\partial U}{\partial X}\right)+\frac{\partial}{\partial Y}\left(\eta^*\frac{\partial U}{\partial Y}+\eta^*\frac{\partial V}{\partial X}\right)\right) -\left(\frac{\partial \tau_X^* P_X}{\partial X}+\frac{\partial \tau_Y^* P_X}{\partial X}\right) \tag{10}$$

$$U\frac{\partial U}{\partial X}+V\frac{\partial U}{\partial Y}=-\frac{\partial P}{\partial Y}+\frac{1}{Re}\left(\frac{\partial}{\partial Y}\left(2\eta^*\frac{\partial U}{\partial Y}\right)+\frac{\partial}{\partial X}\left(\eta^*\frac{\partial V}{\partial X}+\eta^*\frac{\partial U}{\partial Y}\right)\right) -\left(\frac{\partial \tau_X^* P_Y}{\partial X}+\frac{\partial \tau_Y^* P_Y}{\partial Y}\right)+\frac{Ra}{Re^2 Pr}\theta \tag{11}$$

$$U\frac{\partial W}{\partial X}+V\frac{\partial W}{\partial Y}=-\frac{\partial P}{\partial Z}+\frac{1}{Re}\left(\frac{\partial^2 \eta^* W}{\partial X^2}+\frac{\partial^2 \eta^* W}{\partial Y^2}\right)+\left(\frac{\partial \tau_X^* P_Z}{\partial X}+\frac{\partial \tau_Y^* P_Z}{\partial Y}\right) \tag{12}$$

- Energy Conservation

$$U\frac{\partial \theta}{\partial X}+V\frac{\partial \theta}{\partial Y}=\frac{1}{RePr}\left(\frac{\partial^2 \theta}{\partial X^2}+\frac{\partial^2 \theta}{\partial Y^2}-\frac{2\alpha}{(\alpha+1)}\frac{W}{\overline{W}}\right) \tag{13}$$

where τ^{*P}_{ij} is ij^{th} component of $\boldsymbol{\tau}^{*\mathbf{P}}$. In the equations above, the following dimensionless parameters can be identified:

$$\alpha\equiv\frac{W}{H};Ra\equiv\frac{\rho^2 cg\beta D_H^4 qw}{\eta_{char}\kappa^2};Pr\equiv\frac{c\eta_{char}}{\kappa};Re\equiv\frac{\rho v_{char} D_H}{\eta_{char}} \tag{14}$$

$$De_1\equiv\frac{\Psi_1\dot{\gamma}_{char}}{\eta_{char}};De_2\equiv-\frac{\Psi_2\dot{\gamma}_{char}}{\eta_{char}} \tag{15}$$

$$\Psi_1{}^*\equiv\frac{De_1}{Re};\Psi_2{}^*\equiv\frac{De_2}{Re} \tag{16}$$

The dimensionless groups that appear in the governing equations are defined in Eqs. (14), (15) and (16). Equation (14) gives the aspect ratio, α, the Rayleigh number, Ra, the Prandtl number, Pr, and the Reynolds number, Re. Two dimensionless viscoelastic parameters, namely, the first Deborah

number, De_1, and the second Deborah number, De_2, are defined in Eq. (15). Equation (16) gives the dimensionless normal stress coeficients. These dimensionless groups appear in the dimensionless "polymetric" stress τ^{*P}.

Due to symmetry, the computational domain is reduced to the right half of the cross section. Then, the sought-for solution of Eqs. (9)-(13) must satisfy the boundary conditions below.

- $X = 0; U = 0; \frac{\partial V}{\partial X} = \frac{\partial W}{\partial X} = 0; \frac{\partial \theta}{\partial X} = 0$
- $X = \frac{\alpha + 1}{4}; U = V = W = 0; \frac{\partial \theta}{\partial X} = 0$
- $Y = 0; U = V = W = 0; -\frac{\partial \theta}{\partial Y} = 1$
- $Y = \frac{\alpha + 1}{2\alpha}; U = V = W = 0; \frac{\partial \theta}{\partial Y} = 1$

Nusselt numbers

Heat transfer at the lower and upper walls is given by the following Nusselt numbers:

$$Nu_i = \frac{q_W D_H}{\kappa\left(\overline{T_{w,i}} - T_b\right)} = \frac{1}{\overline{\theta_{w,i}}}; Nu_s \equiv \frac{qwD_H}{\kappa\left(\overline{T_{w,s}} - T_b\right)} = \frac{1}{\overline{\theta_{w,s}}} \qquad (17)$$

In the expressions above $\overline{T_{w,i}}$ and $\overline{T_{w,s}}$ are the mean temperatures of the lower and upper walls. The quantities $\overline{\theta_{w,i}}$ and $\overline{\theta_{w,s}}$ are the corresponding dimensionless mean temperatures (Naccache and Souza Mendes, 1993).

The appropriate mean Nusselt number, Nu_m is defined as $Nu_m \equiv Nu_i Nu_s / (Nu_s + Nu_i)$.

Governing parameters

The parameters that govern the present problem are the ones that appear in Eqs. (9)-(13), in the constitutive equation (Eq. (1)), and in the boundary conditions. They are: Re, Ra, Pr, Ψ_1^*, Ψ_2^*, $\alpha = W/H$, $We \equiv \lambda\dot{\gamma}_{char}$, $\eta_0^* \equiv \eta_0/\eta_{char}$, $\eta_\infty^* \equiv \eta_\infty/\eta_{char}$, n and a.

Because of the great number of parameters, the parametric study is restricted to some of the appearing parameters. They are: the Reynolds number, the Rayleigh number, the second normal stress coefficient and the aspect ratio. In addition, some of the results to be presented indicate the sensitivity of Nusselt numbers to the Prandtl number, the Weissenberg number and the first normal stress coefficient. The dimensionless viscosities η_0^*, η_∞^* and the parameters n and a are held fixed, mainly because they do not affect the secondary flows, which are the main focus of the present work.

The first and second normal stress coefficients are assumed constant to simplify the analysis so that their ratio Ψ_2/Ψ_1 is kept at -0.15 ($\Psi_2^*/\Psi_1^* = 0.15$), as often observed in polymeric liquids. Preliminary tests showed that allowing the normal stress coefficients to vary with the shear rate does not affect the results significantly (Naccache, 1993).

Results and Discussion

The differential governing equations were solved by means of the control-volume approach described by Patankar (1980). The coupling of momentum, continuity, energy, and constitutive equations was handled with the aid of the Simple algorithm. The discretized algebraic system was solved through the line-by-line Thomas algorithm.

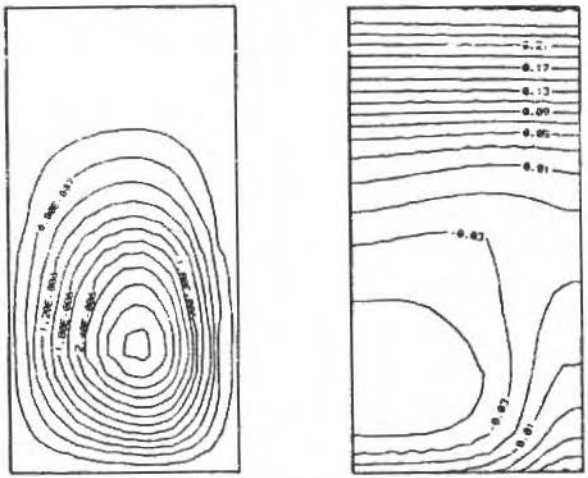

Fig. 2 $\Psi_2^* = 0$ (a) Streamlines (b) Isotherms

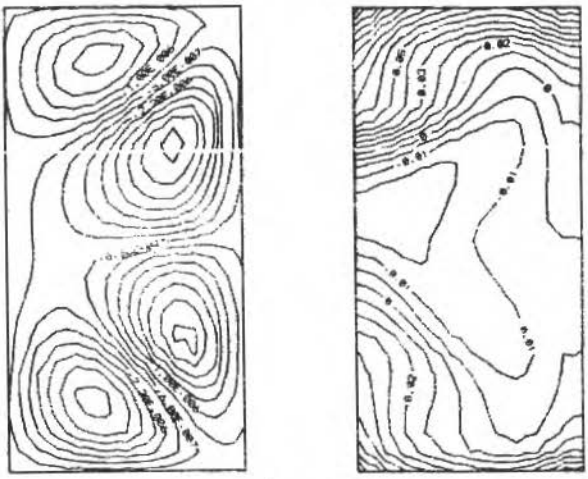

Fig. 3 $\Psi_2^* = 10^{-3}$ (a) Streamlines (b) Isotherms

The mesh sizes employed were 16 x 22 for $\alpha = 1$; 20 x 20 for $\alpha = 2$; and 22 x 16 for $\alpha = 4$. These sizes were chosen with basis on results of a number of tests. A more detailed discussion on the numerical solution can be found in Naccache (1993).

Some difficulties in convergence were caused by the highly non-linear character of the equations of motion. In order to overcome these problems and obtain a converged solution, a zero-th order continuation procedure in Ψ_2 was employed, starting from the solution for the Newtonian case. A similar continuation procedure in Ra was also needed, starting with the results for forced convection only Ra= 0.

A few representative results are now presented and analyzed. For a more complete discussion, please see Naccache (1993).

All the results were obtained for $\eta_{char} = 0.011$, $\eta_\infty^* = 0.36$, $\eta_0^* = 26.36$, We = 1500, n = 0.494, and a = 0.942.

Figures 2-3 show the flow patterns and the isotherms for Ra = 10^6, Pr= 70, We = 1500, Re = 2.5 x 10^4 and $\alpha = 1$. These results are very similar to that obtained in (Naccache and Souza Mendes, 1992).

It can be noted that when there is no viscoelasticity (Fig. 2) the flow is almost stagnant near the upper wall and the isotherms are horizontal lines. This behavior produces the largest differences between Nu_i and Nu_s. As the viscoelastic force increases, the fluid near the upper wall firstly starts flowing, then increase its intensity, until a simmetric configuration is achieved (Fig. 3). In this latter situation buoyancy forces are negligible when compared to viscoelastic ones. In this flow regime, temperature gradients near the heated walls are relatively high, and large heat transfer coefficients are in effect.

Figures 4a and 4b show the upper-wall and mean Nusselt numbers, as a function of Ψ_2^* for a square cross section, Pr = 70 and We = 1500. It is important to note that mean Nusselt number behavior is quite similar to the upper Nusselt number. It can be noted that for small viscoelastic forces the difference between lower-wall and mean (or upper-wall) heat transfer coefficients is very large, and the Reynolds number does not influence the heat transfer. On the other hand, when viscoelastic forces are large, natural convection does not influence the heat transfer behavior, and due to symmetry Nu_i is identical to Nu_s. Also, it can be noted that for the largest values of Ψ_2^*, the Nusselt number starts to decrease. This is due to the Ψ_1^* effect, as also observed and discussed in Naccache and Souza Mendes (1992).

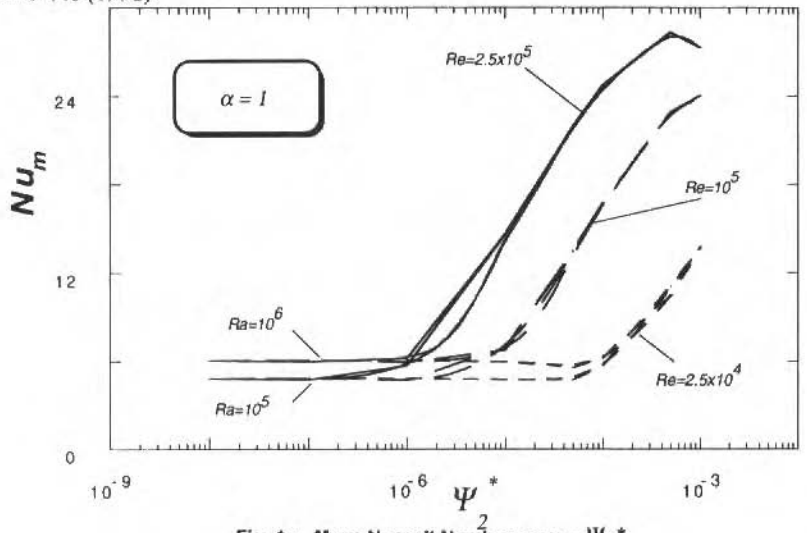

Fig. 4a Mean Nusselt Number versus Ψ_2^*

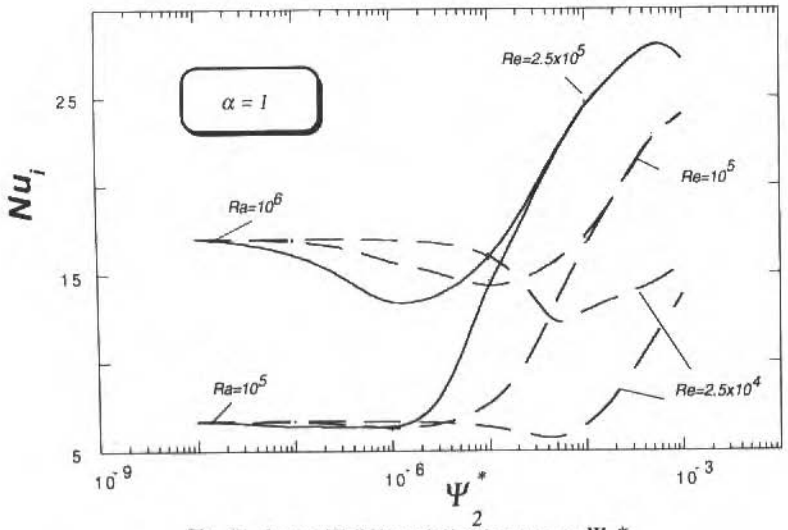

Fig. 4b Lower-Wall Nusselt Number versus Ψ_2^*

Figures 5a and 5b show the Nusselt number as a function of Ψ_2^* for Ra = 10^6, Pr = 70 and We = 1500. It can be seen that the curves obtained for three different aspect ratios are closer to each other the ones found in Naccache and Souza Mendes (1992). This is due to the fact that in the present analysis the Prandtl number is held fixed, which is not true in Naccache and Souza Mendes (1992). It can also be noted that there are critical values of the aspect ratio-which depend on Ψ_2^* and Ra-that correspond to maxima of the heat transfer coefficient. This occurrence can be explained by the changes in flow pattern as the aspect ratio is changed, as discussed in Naccache (1993). The effect of Prandtl number is illustrated in Fig. 6, for α = 1 and no natural convection. It can be observed that the Nusselt number increases with the Prandtl number. This trend gets more accentuated as the Reynolds number is increased.

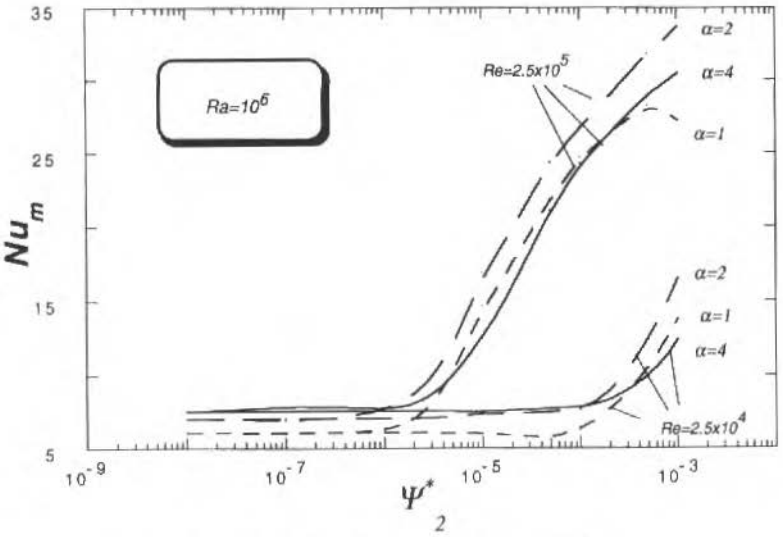

Fig. 5a Mean Nusselt Number versus Ψ_2^*

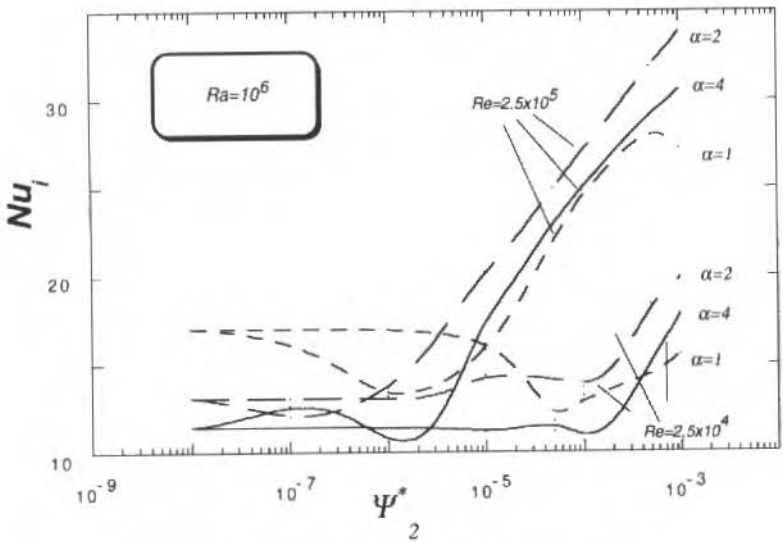

Fig. 5b Lower-Wall Nusselt Number versus Ψ_2^*

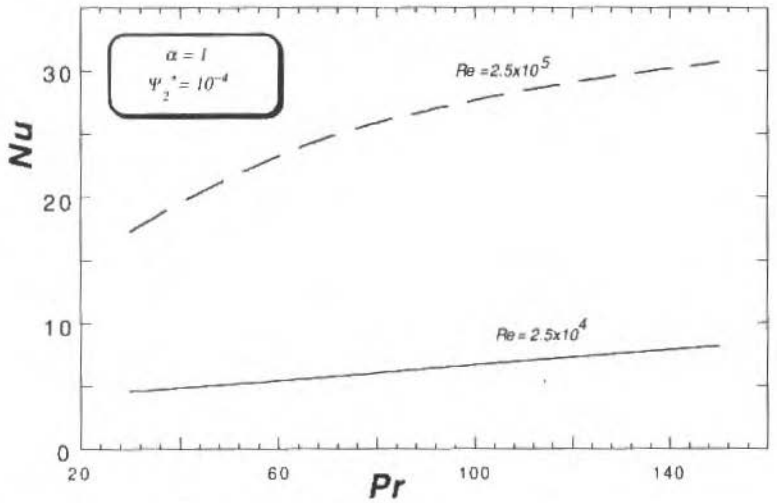

Fig. 6 Mean Nusselt Number versus Pr.

In Fig.7, it is illustrated that the Weissenberg number does not influence the Nusselt number in a significant manner. Figure 8 shows that Ψ_1^* becomes an important parameter as it gets large only, and that it influences Nu in the opposite direction as Ψ_2^* does.

Figure 9 shows the Nusselt numbers as a function of the dimensionless parameter defined as $\Lambda \equiv Re^2 Pr \Psi_2^*$. It helps characterizing three different flow regimes: for small values of Λ, natural convection governs the secondary flow; for intermediate values of Λ viscoelastic and buoyancy forces are both important; and for large values of Λ, the secondary flow is driven by viscoelastic forces alone.

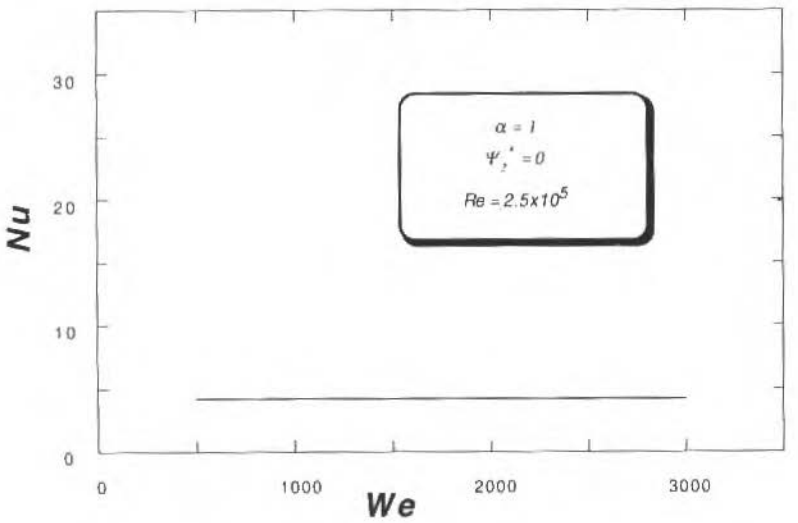

Fig. 7 Mean Nusselt Number versus We

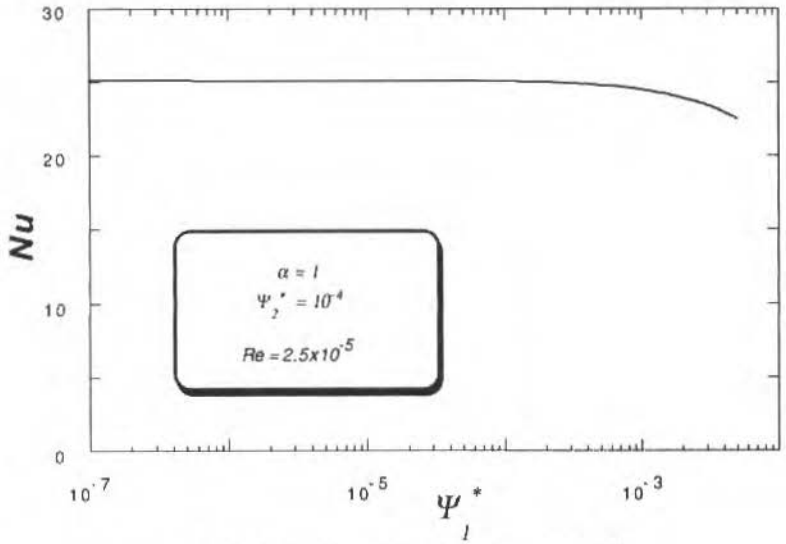

Fig. 8 Lower-Wall Nusselt Number versus Ψ_1^*

Final Remarks

The present paper analyzes the combined effects of buoyancy and viscoelastic forces on the velocity and temperature fields of laminar flow of viscoelastic liquids through rectangular ducts. It was found that heat transfer is strongly influenced by both natural convection and elastic effects. The relative importance of buoyancy and elastic effects as far as heat transfer is concerned is assessed via a parametric study. A dimensionless parameter which compares both effects is employed to present heat transfer results.

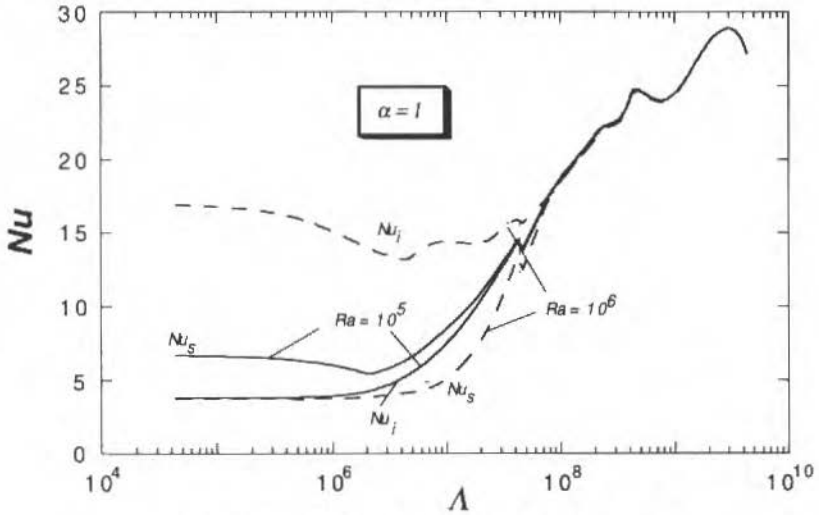

Fig. 9 Upper and Lower-Wall Nusselt Number versus Λ

References

Bird, R. B., Armstrong R. C., and Hassager O., 1987, "Dynamics of Polymeric Liquids", 2nd ed., John Wiley & Sons.

Hartnett, J.P., 1992, "Viscoelastic Fluids: A New Challenge in Heat Transfer," J. of Heat Transfer, Vol. 114, pp. 269-303.

Hartnett, J. P., and Kostic M., 1985, "Heat Transfer to a Viscoelastic Fluid in Laminar Flow through a Rectangular Channel," Int. J. Heat and Mass Transfer, Vol. 28, pp. 1147-1155.

Langlois, W. E., and Rivlin R. S., 1963, "Slow Steady-State Flow of Viscoelastic Fluid through Non-Circular Tubes," Rend. Math., Vol. 22, pp. 169-185.

Mayné, G., 1992, "Secondary Flows of Non-Newtonian Fluids in Rectilinear Pipes," Theor & Appl. Rheology, Proc. XIth Int. Congr. on Rhelogy, Belgium, August.

Mena, B., Best B., Bautista P., and Sanchez T., 1978, "Heat Transfer in Non-Newtonian Flow through Pipes", Rheol. Acta, Vol. 17, pp. 454-457.

Naccache, M. F., 1993, "Mixed-Convection Heat Transfer to Viscoelastic Liquids Flowing Laminarly Inside Rectangular Ducts" (in Portuguese), PH.D. thesis, Pontifícia Universidade Católica, Rio de Janeiro.

Naccache, M. F., 1992, "Combined Viscoelasticity and Free Convection in the Laminar Flow through Rectangular Ducts", Proc. XII COBEM, pp. 1053-1056.

Oliver, D. R., 1969, "Non-Newtonian Heat Transfer: an Interesting Effect Observed in Non-Circular Tubes", Trans. Instn. Chem. Engr., Vol. 47, pp. 18-20.

Winter, H. H., 1977, "Viscous Dissipation in Shear Flows of Molten Polymers" Advances in Heat Transfer, Vol. 13, pp. 205-267.

RBCM - J. of the Braz. Soc. Mechanical Sciences
Vol. XVII- nº3 - 1995

ISSN 0100-7386
Printed in Brazil

Abstracts

Vargas, J. V. C., Saboya, F. E. M., and Bianchi, M. V. A., "Initial Values Searching Method For Solving Non-Similar Boundary Layer Problems by the Local Non-Similarity Model", RBCM - J. of the Braz. Soc. Mechanical Sciences, Vol. 17, No. 3, pp. 252-268.

The present work introduces a method for searching initial values, to solve non-similar Boundary Layer problems through the local non-similarity model. In order to provide a view to illustrate the method, the problem of mixed convection on a wedge and the surface mass transfer problem of uniform injection (blowing) in a flat plate under forced convection are solved herein. The results for the latter and for the special case when the wedge becomes a vertical plate are compared with prior information from the published literature and novel results are presented for the 90° and 180° wedge, where the problem is non-similar and $U = Ax^m$. It is also shown the method provides results of high accuracy, for the whole range of variation of the non-similarity parameter, and with only one transformation of variables, based on scale analysis for forced convection, both to uniform surface temperature and to uniform heat flux.
Keywords: Boundary Layer Problem, Local Non-Similarity, Initial Value Search, Mixed Convection on a Wedge, Uniform Injection

d' Almeida, J. R. M., and Monteiro, S. N., "Strain Rate Effects on the Fracture Toughness Mechanisms of an Epoxy Resin and its Alumina Powder Composite" RBCM - J. of the Braz. Soc. Mechanical Sciences, Vol. 17, No. 3, pp. 269-277.

The micromechanisms of fracture of an alumina powder epoxy matrix composite was identified and compared with the fracture mechanisms of the neat epoxy matrix. The effect of strain rate upon the fracture behavior of the composite and that of the neat epoxy matrix was evaluated. A strong increase in the neat resin fracture toughness at high strain rates was associated with crack tip blunting.
Keywords: Composite, Crack Blunting, Strain Rate Effect.

Horikawa, O., Sato, K., and Shimokohbe, A., "Achieving Ultra-Precision by Mechatronics: Active Air Journal Bearing", RBCM - J. of the Braz. Soc. Mechanical Sciences, Vol. 17, No. 3, pp. 278-291.

Aiming bearings of: ultra-precision, infinite stiffness, high vibration damping capability and new functions (axis positioning and dynamic stiffness control), the authors present in this paper an "active air journal bearing" AAJB, a novel type of bearing, capable of precisely controlling the radial position of its axis. The AAJB that is the result of the application of concepts of the mechatronics, utilizes non-contact sensors to detect the radial position of the axis, non-contact actuators (movable air pads driven by piezo-electric actuators) to support and drive the axis, and a controller to regulate the whole system. In the paper, the basic configuration of the AAJB as well as its dynamic model and the controller design is shown. The stiffness and the positioning characteristics of the AAJB are examined and a method of compensating motion errors caused by profile error of the axis and bearing parts is presented. By experiments, it is shown that the AAJB has: an almost infinite static stiffness and an increased damping capability, a band-width of more than 1 KHz and an absolute rotary motion accuracy of better than 21 nm with the axis rotating at 750 rpm.
Keywords: Air Bearing, Mechatronics, Active Air Journal Bearing.

de Castro, J. T. P., and Kenedi, P. P., "Fatigue Crack Growth Rate Prediction Departing from Coffin-Manson Concepts", RBCM - J. of the Braz. Soc. Mechanical Sciences, Vol. 17, No. 3, pp. 292-303 (In Portuguese).

The Conffin-Manson and the Paris methods, which are normally used in a supplementary but impervious way in the dimensioning against the crack initiation and propagation phases of the fatigue process, are correlated through a series of simple and didactic appealing models. All the proposed models use the classical engineering routines based on cyclic mechanical properties and on the Miner's linear damage accumulation rule. The simpler one uses a singular plastic strain field to estimate the crack growth propagation rate, whereas the more complex recognize the finite dimension of the fatigue crack tip radius, and use various strain concentration rules to quantify the maximum strain amplitude. The models are easy to apply and to phenomenologically justify, and they present a very encouraging correlation with experimental results reported in the literature.
Keywords: Fatigue, Crack Growth Rate, Low-Cicle Fatigue

Baldo, E. D. and Diniz, A. E., "Reducing the Plunge Cylindrical Grinding Time Using Acoustic Emission Monitoring", RBCM - J. of the Braz. Soc. Mechanical Sciences, Vol. 17, No. 3, pp. 304-313.

The spark out stage is responsible usually for up to one third of the time spent in a plunge grinding cycle. Some authors have proposed the implementation of an accelerated spark out stage, in which the wheel position passes the final diameter of the part and returns quickly. This technique, up to now, has been difficult to implement since the feedback parameters have not been clearly defined. This paper attempts to investigate the accelerated sparkout method and examine the effect on part quality. Acoustic emission, generated by the grinding process, is shown to be a very good way to establish the parameters necessary to implement the accelerated spark out stage. It is also shown in this work that this kind of cycle does not damage the part.
Keywords: Grinding, Monitoring, Acoustic Emission

Queiroz, R. S., Falbo, R. A. and Varejão, L. M. C., "Heat Islands Influence on the Dispersion of Contaminants by the Atmosphere", RBCM - J. of the Braz. Soc. Mechanical Sciences, Vol. 17, No. 3, pp. 314-321(In Portuguese).

A two-dimensional model for atmospheric flows based on linear momentun, energy and mass conservation equations is used to simulate the effects of heat islands on the concentration field of contaminant species. The finite volume method is used to solve the equations and the results show that the concentration field is strongly dependent on local dispersive capacity.
Keywords: Atmospheric Flow, Heat Islands, Concentration Field of Contaminant Species, Local Dispersive Capacity

Duarte, L.G.C., and Azevedo, L. F. A., "Mass Transfer from Impinging Swirling Jets", RBCM - J. of the Braz. Soc. Mechanical Sciences, Vol. 17, No. 3, pp. 322-330 (In Portuguese).

The present work is an experimental study of the mass transfer characteristics of a swirling jet impinging on a flat plate. The main objective of the investigation was to determine the influence of a circunferential velocity component (the swirl component) on the local and average mass transfer coefficients at the plate surface. The dimensionless parameters investigated were the jet Reynolds number, the jet-to-plate distance, and the strength of the swirl flow given by the swirl number. Mass transfer coefficients were obtained utilizing the naphthalene sublimation technique. The local coefficients were determined employing a computerized coordinate table which allowed a detailed study of the effects of the presence of the swirl component. Average coefficients were determined independently through precision weighing, and displayed excellent agreement with the integrated local coefficients. The results demonstrated that the presence of the swirl component decreases the mass transfer coefficients, when compared with than non swirl case.
Keywords: Mass Transfer, Swirling Jet, Jet Imping on a Flat Plate

Naccache, M. F. and Souza Mendes, P. R., "Mixed - Convection in Flows of Viscoelastic Liquids - A Parametric Study", RBCM - J. of the Braz. Soc. Mechanical Sciences, Vol. 17, No. 3, pp. 331-340.

A parametric analysis of the viscoelastic laminar flow through rectangular ducts is presented, which gives a generic insight of the relative importance of physical parameters. The effects of the elastic and buoyancy forces on flow patterns and on heat transfer are analyzed, as well as the effects of the Reynolds, Prandtl and Weissenberg numbers. The results show the existence of a physical dimensionless parameter which gives the relative influence of the elastic and buoyancy effects on flow patterns and heat transfer
Keywords: Viscoelastic Liquid, Flow Through Rectangular Duct, Elastic Force, Buoyance Force, Flow Pattern, Heat-Transfer

Journal of the
razilian Society of
chanical Sciences

Information for Authors

SCOPE AND POLICY

- The purpose of the Journal of the Brazilian Society of Mechanical Sciences is to publish papers of permanent interest dealing with research, development and design related to science and technology in Mechanical Engineering, encompassing interfaces with Civil, Electrical, Chemical, Naval, Nuclear, Agricultural, Materials, Petroleum, Aerospace, Food, System Engineering, etc., as well as with Physics and Applied Mathematics.
- The Journal publishes Full-Length Papers, Review Papers and Letters to the Editor. Authors must agree not publish elsewhere a paper submitted to and accepted by the Journal. Exception can be made for papers previously published in proceedings of conferences. In this case it should be cited as a footnote on the title page. Copies of the conference referees reviews should be also included. Review articles should constitute a critical appraisal of published information.
- The decision of acceptance for publication lies with the Editors and is based on the recommendations of at least two ad hoc reviewers, and of the Editorial Board, if necessary.

SUBMISSION

- Manuscripts and all the correspondence should be sent to the Editor or, alternatively, to the appropriate Associate Editor.
- Four (4) copies of the manuscript are required. The author should submit the original figures, which will be returned if the paper is not accepted after the review process.
- Manuscripts should be submitted in English or Portuguese. Spanish will also be considered.
- A manuscript submitted for publication should be accompanied by a cover letter containing the full name(s) of author(s), mailing adresses, the author for contact, including phone and fax number, and, if the authors so wish, the names of up to five persons who could act as referees.

FORMAT

- Manuscripts should begin with the title, including the english title, the abstract and up to five key words. If the paper's language is not English, an extended summary of about 500 words should be included. The manuscript should not contain the author(s) name(s).
- In research papers, sufficient information should be provided in the text or by refering to papers in generally available Journals to permit the work to be repeated.
- Manuscripts should be typed double-spaced, on one side of the page, using A-4 sized paper, with 2 cm margins. The pages should be numbered and not to excess 24 pages, including tables and figures. The lead author of a RBCM paper which exceeds the standard length of pages will be assessed a excess page charge.
- All symbols should be defined in the text. A separate nomenclature section should list, in alphabetical order, the symbols used in the text and their definitions. The greek symbols follow the English symbols, and are followed by the subscripts and superscripts. Each dimensional symbol must have SI (Metric) units mentioned at the end. In addition, English units may be included parenthetically. Dimensionless groups and coefficients must be so indicated as dimensionless after their definition.
- Uncertainties should be specified for experimental and numerical results.

ILLUSTRATIONS AND TABLES

- Figures and Tables should be referred in consecutive arabic numerals. They should have a caption and be placed as close as possible to the text first reference.
- Line drawings should be prepared on tracing paper or vellum, using India ink; line work must be even and black. Laser print output is acceptable. The drawings with technical data/results should have a boundary on all four sides with scale indicators (tick marks) on all four sides. The legend for the data symbols should be put in the figure as well as labels for each curve wherever possible.
- Illustrations should not be larger than 12 x 17 cm. Lettering should be large enough to be clearly legible (1.5-2.0 mm).
- Photographs must be glossy prints.

REFERENCES

- References should be cited in the text by giving the last name of the author(s) and the year of publication of the reference: either "Recent work (Smith and Jones, 1985) ... or "Recently Smith and Jones (1985) With four or more names, use the form "Smith et al.(1985)" in the text. When two or more references would have the same text identification, distinguish them by appending "a", "b", etc., to the year of publication.
- Acceptable references include: journal articles,dissertations, published conference proceedings, numbered paper preprints from conferences, books, submitted articles if the journal is identified, and private communications.
- References should be listed in alphabetical order, according to the last name of the first author, at the end of paper. Some sample references follow:

Bordalo, S.N., Ferziger, J.H. and Kline, S.J., 1989, "The Development of Zonal Models for Turbulence", Proceedings, 10th ABCM - Mechanical Engineering Conference, Vol. I, Rio de Janeiro, Brazil, pp. 41-44.

Clark, J.A., 1986, Private Communication, University of Michigan, Ann Arbor, MI.

Coimbra, A.L., 1978, "Lessons of Continuum Mechanics", Editora Edgard Blucher Ltda, São Paulo, Brazil.

Kandlikar, S.G. and Shah, R.K., 1989, "Asymptotic Effectiveness - NTU Formulas for Multiphase Plate Heat Exchangers", ASME Journal of Heat Transfer, Vol. 111, pp. 314-321.

McCormak, R.W., 1988, "On the Development of Efficient Algorithms for Three Dimensional Fluid Flow", Journal of The Brazilian Society of Mechanical Sciences, Vol. 10, pp. 323-346.

Silva, L.H.M., 1988, "New Integral Formulation for Problems in Mechanics", (in portuguese), Ph.D. Thesis, Federal University of Santa Catarina, Florianópolis, SC, Brazil.

Sparrow, E.M., 1980a, "Forced-Convection Heat Transfer in a Duct Having Spanwise-Periodic Rectangular Protuberances", Numerical Heat Transfer, Vol. 3, pp. 149-167.

Sparrow, E.M., 1980b, "Fluid-to-Fluid Conjugate Heat Transfer for a Vertical Pipe-Internal Forced Convection and External Natural Convection", ASME Journal of Heat Transfer, Vol. 102, pp. 402-407.

ISSN 0100 - 7386

JOURNAL OF THE BRAZILIAN SOCIETY OF MECHANICAL SCIENCES
REVISTA BRASILEIRA DE CIÊNCIAS MECÂNICAS

VOL. XVII - Nº 3 - 1995